CORRUSION BEHAVIOR OF Al-Al_2O_3 COMPOSITES IN AERATED 3.5% CHLORIDE SOLUTION

by

Paul Omar Acevedo Hurtado

A thesis submitted in partial fulfillment of the requirements for the degree of

MASTER OF SCIENCE
in
MECHANICAL ENGINEERING

UNIVERSITY OF PUERTO RICO
MAYAGÜEZ CAMPUS
2010

Approved by:

_____	_____
Nestor Peréz, PhD Member, Graduate Committee	Date
_____	_____
Pablo Caceres, PhD Member, Graduate Committee	Date
_____	_____
Paul Sundaram, PhD President, Graduate Committee	Date
_____	_____
Aaron Cavosie, PhD Representative of Graduate Studies	Date
_____	_____
Gustavo Gutierrez, PhD Chairperson of the Department	Date

ABSTRACT

Aluminum based metal matrix composites are finding many applications in engineering. Of these Al-Al_2O_3 composites appear to have promise in a number of defense applications because of their mechanical properties. However, their corrosion behavior remains suspect, especially in marine environments. While efforts are being made to improve the corrosion resistance of Al-Al_2O_3 composites, the mechanism of corrosion is not well known. In this study, the corrosion behavior of powder metallurgy processed Al-Cu alloy reinforced with 10, 15, 20 and 25 vol. % Al_2O_3 particles (XT 1129, XT 2009, XT 2048, XT 2031) was evaluated in aerated 3.5% NaCl solution using microstructural and electrochemical measurements. AA1100-O and AA2024T4 monolithic alloys were also studied for comparison purposes. The composites and unreinforced alloys were subjected to potentiodynamic polarization and Electrochemical Impedance Spectroscopy (EIS) testing. Addition of 25 vol. % Al_2O_3 to the base alloys was found to increase its corrosion resistance considerably. Microstructural studies revealed the presence of intermetallic Al_2Cu particles in these composites that appeared to play an important role in the observations. Pitting potential for these composites was near corrosion potential values, and repassivation potential was below the corresponding corrosion potential, indicating that these materials begin to corrode spontaneously as soon as they come in contact with the 3.5 % NaCl solution. EIS measurements indicate the occurrence of adsorption/diffusion phenomena at the interface of the composites which ultimately initiate localized or pitting corrosion. Polarization resistance values were extracted from the EIS data for all the materials tested.

Electrically equivalent circuits are proposed to describe and substantiate the corrosive processes occurring in these Al-Al_2O_3 composite materials.

RESUMEN

Los compuestos de matriz metálica de aluminio encuentran muchas aplicaciones en ingeniería. De estos compuestos Al-Al_2O_3 parecen tener un sinnúmero de aplicaciones como materiales de defensa debido a sus propiedades mecánicas. Sin embargo, su comportamiento a la corrosión es incierto, especialmente en ambientes marinos. Mientras se realizan esfuerzos para mejorar su resistencia a la corrosión de Al-Al_2O_3, los mecanismos de corrosión aun están en discusión. En este estudio, el comportamiento a la corrosión de las aleaciones Al-Cu procesadas por pulvimetalurgia reforzadas con 10, 15, 20, 25 % de partículas de alúmina en volumen (XT 1129, XT 2009, XT 2048, XT 2031 en ese orden) fueron evaluadas en una solución aireada al 3.5% de NaCl usando mediciones micro-estructurales y electroquímicas. Aleaciones monolíticas AA1100-O y AA2024-T3 fueron usadas para comparación. Los compuestos y las aleaciones no reforzados fueron sujetos a ensayos polarización potencio-dinámica y Espectroscopia de Impedancia Electroquímica (EIS, por sus siglas en ingles). Se encontró que adiciones de 25% en volumen de Al_2O_3 a la aleación base incrementa la resistencia a la corrosión considerablemente. Estudios de micro-estructura revelan partículas de compuesto intermetalico Al_2Cu jugando un papel importante en estas observaciones. El potencial de picado para estos compuestos fue cercano al potencial de corrosión, y el potencial de repasivación estuvo por debajo del potencial de corrosión, indicando que estos materiales comienzan a corroer espontáneamente tan pronto entran en contacto con la solución de 3.5% de NaCl. Mediciones de EIS indican fenómenos

de adsorción/difusión en la interface de los compuestos las cuales inician la corrosión localizada o picado. Los valores de la resistencia de polarización fueron extraídos de los datos de EIS. El circuito equivalente fue propuesto para describir y sustraer los procesos de corrosión de los materiales compuestos Al-Al_2O_3.

To God for being always with me.

To my Mother for her confidence and understanding.

To my Father for teaching me how to get by in life.

To my sister Griset for being the refuge of my heart.

ACKNOWLEDGEMENTS

During the development of my graduate studies in the University of Puerto Rico several persons and institutions collaborated directly and indirectly with my research. Without their support it would be impossible for me to finish my work. That is why I wish to dedicate this section to recognize their support.

Most of all, I cannot fully express my gratitude to my advisor, Dr. Paul Sundaram for his immeasurable support, superb guidance and excellent advice. He has always given me inspiration and encouragement to finish my studies at Puerto Rico. Under his wing, I have learned about writing papers and expressing them in public presentations.

Table of Contents

List of Tables

Tables **Page**

List of Figures

Figures **Page**

1 INTRODUCTION

Metals are extremely versatile engineering materials. A metallic material can exhibit a wide range of readily controllable properties through appropriate selection of alloy composition and thermo-mechanical processing methods. The development of Metal Matrix Composites (MMCs) has reflected the need to achieve property combinations beyond those attainable in monolithic metal alone [1]. MMCs can no longer be excluded from daily life. MMCs offer significant performance advantages over monolithic ceramic or metals, which include attractive combinations of strength, stiffness, wear and creep [2]. Composites were initially developed for military and space applications, after which they have percolated to the civilian world although the individual consumer is unaware of the variety of material systems and their applications; in many cases they are even unknown. Examples are carbides for machining of materials in product engineering, noble metal composites systems for contact in electronics and electro-technology, copper-graphite sliding contacts for generator and electric motors and multi-compound system for brake linings in high speed brakes [3]. This material group becomes of interest for construction and functional materials, if the property profile of conventional materials either does not reach the increased standard of specific demands, or it is not the best solution to the engineering problem at hand. The advantages of metal matrix composites are of great utility if a meaningful cost-performance relationship is possible during production of components. Of special economic and ecological interest is the need for integration of processing residues, scrap and waste product from these materials into the material cycle.

MMCs consist of at least two chemically and physically distinct phases, suitably distributed to provide properties not obtainable with either of the individual phases. All metal matrix composites have a metal or a metallic alloy as the matrix. The reinforcement can be metallic or ceramic. In general, there are three kinds of metal matrix composites: i) particle reinforced MMCs, ii) short fiber or whisker reinforced MMCs and iii) continuous fiber or sheet reinforced MMCs. The parameter that allows us to distinguish between these different forms of reinforcements is called the aspect ratio. Thus, continuous fibers have an aspect ratio approaching infinity while perfectly equiaxed particles have an aspect ratio of about one.

Selection of the matrix metal and reinforcement constituent is usually based on how well the combination interacts to achieve the desired properties. Interaction of the MMC with the environment is normally a secondary consideration. The corrosion resistance of the MMC is usually inferior to that of its monolithic matrix alloy, due to one or more of the following reasons [4]:

1. Galvanic coupling of reinforcement constituent and matrix.
2. Formation of interphase between the reinforcement constituent and matrix.
3. Microstructural contaminant and processing residuals in MMC.
4. Microstructural changes caused by the presence of the reinforcement constituents.

In a modern business environment, successful enterprises cannot tolerate major corrosion failures, especially those involving personal injuries, fatalities, unscheduled shutdowns and environmental contamination. Decisions regarding the integrity of a structure or its components depend on an accurate assessment of the conditions affecting its corrosion and rate of deterioration. Required levels of maintenance can vary greatly depending on the

severity of the operating environments. For this reason, considerable effort is generally expended in corrosion control at the design stage and in the operational phase. Even the best of designs cannot be expected to anticipate all the conditions that may arise during the life of a system.

Aluminum-based composites have been under development for many years during which time a vast number of different types of reinforcement have been attempted with varying degrees of success. The particular attributes of aluminum composites are a combination of high specific stiffness, good fatigue properties, and relatively low-cost conventional processing. There are a number of variables to be considered, including the type and level of reinforcement, the choice of matrix alloy, and the composite processing route, to meet the requirements of a specific application. Corrosion resistance, strength levels, toughness, etc. are all strongly influenced by the matrix alloy.

The corrosion behavior of Al-based MMCs has been shown to depend not only on metal-reinforcement combination, but also on manufacturing process parameters. The influence of manufacturing process and weight fraction of reinforcing particles on the corrosion behavior in 3.5 wt% NaCl solution improves or reduces the corrosion resistance of the composites [5].

Despite the risk of corrosive attack, most of the research on MMCs has been concentrated on the mechanical properties and the effect of processing route on these properties [1,2]. The purpose of the current study is to answer some fundamental questions regarding the corrosion mechanisms in Al-Al_2O_3 metal matrix composites in a marine environment, because the interaction between chloride with the time of wetness (time of exposure to the corrosive

environment) was found to be the most significant factor influencing the corrosion of Al alloys.

1.1. Motivation

The development of MMCs has widened the field of engineering applications by the modification of the mechanical properties of monolithic matrix, i.e., stiffness, strength, thermal conductivity, etc. by the incorporation of a suitable reinforcement However, the degradation of MMCs in different environments has to be explored further, The present thesis is focused on the experimental testing of Al-Al_2O_3 composites with the goal of obtaining results leading to understanding and explanation of the phenomenon of degradation by corrosion of these MMCs in a chloride environment.

1.2. Objectives

The overall goal is to study the effect of particulate Al_2O_3 addition in various proportions to four aluminum based alloys (XT1129/Al_2O_3/10Vol, XT2009/Al_2O_3/15Vol, XT-2048/Al_2O_3/20Vol and XT-2031/Al_2O_3/25Vol) on their corrosion behavior in aerated 3.5% NaCl solution.

An attempt will be made to explain the role of additions of different percentages of Al_2O_3 reinforced particles to the base alloy on its corrosion behavior by carrying out microstructural studies and electrochemical polarization and electrochemical impedance spectroscopy measurements in 3.5% NaCl solution at room temperature (30 ˚C).

1.3. Summary of Following Chapters

A brief outline of the content of this thesis is as follows. Chapter 2 deals with the basic theories of MMCs, fundamentals of MMC processing, experiments and data analysis related to the behavior of MMCs in a chloride solution. Chapter 3 presents the experimental procedures to analyze the behavior of four different Al-Al_2O_3 MMCs in 3.5% NaCl solution, as well as a brief description of the different techniques used to characterize these results. Chapter 4 is focused on the analysis and interpretation of the obtained results including a technical discussion of these observations. Chapter 5 presents the conclusions of this study.

2 LITERATURE REVIEW

Metal matrix composites are metals that are reinforced with fibers or particles. The fibers and particles can be metal (e.g., tungsten) nonmetal, (e.g., carbon or boron) or ceramic (e.g., silicon carbide (SiC) or alumina (Al_2O_3)). The purpose for reinforcing metals with fibers or particles is to create composites that have properties which are more useful than that of the individual constituents. For example, fibers and particles are used in MMCs to increase stiffness, strength and thermal conductivity, and to reduce weight, thermal expansion, friction, and wear [4,6].

MMCs materials can be produced by many different techniques. The focus of the selection of suitable engineering process is the desired kind, quantity and distribution of the reinforcement component (particles and fibers), the matrix alloy and application. By altering the manufacturing method, the processing and finish, as well as the form of the reinforcement component it is possible to obtain different characteristic profiles, even though the same composition and amount of component are involved [4].

The corrosion resistance of aluminum and aluminum alloys has been extensively studied. Aluminum alloys form a protective oxide film when exposed to air. Aluminum is an extremely reactive metal, but the oxide film causes aluminum to have good corrosion resistance in neutral solutions, where oxide is stable. However, aluminum is susceptible to localized corrosion such as pitting and crevice corrosion. A number of authors have reported that aluminum MMCs pit in chloride solutions, similar to aluminum alloys. A review of corrosion in aluminum and Al-based MMCs is provided below.

2.1. Corrosion of aluminum and aluminum alloys

Aluminum in aerated solutions forms a natural protective oxide about 5nm thick [7,8] consisting of largely amorphous aluminum oxide. As a result, Al alloys show good corrosion resistance in aerated solutions of pH 4 to 9 [8,9]. At high and low pH values, the oxide is soluble and uniform corrosion of aluminum occurs. The naturally formed oxide is an insulator [4]. This suppresses the oxidation-reduction reactions necessary for corrosion to occur due to the high resistance to transfer of electrons across the film. The rate of aluminum corrosion is higher in aluminum alloys with higher copper content [10] or intermetallic precipitates [11]. Copper is a major alloying element for high strength aluminum alloys used in various fields, and is known to have a detrimental effect on localized corrosion [9]. The increase in corrosion rate has been attributed to the lower resistivity of oxide film caused by the incorporation of copper or iron of lower resistivity in the oxide [4,12]. This results in local anodic and cathodic sites in the metal that affect the type and rate of corrosion [13].

The major problem of corrosion with aluminum alloys is localized breakdown of the passive film in the presence of aggressive ions. Halide, particularly the chloride ion, is corrosive to aluminum. The corrosiveness of the chloride ion is a major concern because the ion is ubiquitous; this ion is known to cause pitting on aluminum [11]. In addition, the metal must be polarized above a critical potential known as the pitting potential.

Preferred sites for initiations are flaws in the passive film. Electron microscopy studies suggest that surface films contain enough flaws to provide sites to initiate pitting [11,14,15].

Flaw density increases with increasing alloy content, particularly for copper, so that aluminum alloys containing significant copper levels are more susceptible to pitting [15,16].

2.2. Metal Matrix Composites (MMC)

The best mechanical properties in a composite are provided by continuous fibers. However, these materials have the disadvantage of being the most expensive to produce. In addition, they have to be fabricated in their final shape. If these materials are mechanically worked to form them into the desired shape, the fiber distributions will be disturbed and the brittle fibers are likely to break causing a significant degradation in mechanical properties [17,18]. For this reason, discontinuously reinforced composites are preferable. Discontinuous reinforcements affect mechanical properties negatively to a slight extent, but the resulting composite is significantly cheaper to produce and can be worked into the final shape. The most common methods of production of discontinuous composites are powder metallurgy and casting [19].

Typical reinforcements have the advantage of a relatively low density and include SiC, B_4C, Si_3N_4, AlN, Al_2O_3, etc. Particle reinforced composites are conventionally prepared either via powder metallurgy or liquid metallurgy [20]. In powder metallurgy, metal particles are mixed with reinforcement particles. The particles are then vacuum hot pressed to form a billet. The billet is then hot worked to a usable shape. The metal and oxide particles used to manufacture the composite will have an oxide film on them. Working is critical for powder metallurgy

composites to breakdown the oxides film and promote bonding between the metal matrix and reinforcement [1,21].

Cast composites are produced by mixing reinforcement particles with liquid aluminum, after which the composite can then be cast to a near final shape. Cast composites have a limit of about 20 volume percent reinforcement caused by viscosity limitations. Although cast composites will have the dendritic microstructure typical of a casting process [19], the distribution of the reinforcement particles as such may not be uniform due to settling which is caused by the difference in density between the matrix metal and the reinforcement particles [20].

Interfaces in MMCs often include second phase particles, precipitate free zones, and solute enrichment or depletion. These can be caused by interfacial reactions, heterogeneous nucleation, interfacial diffusion, or combinations of these. These inhomogeneities are expected to have a significant effect on the corrosion behavior of the composite [22-24]. In addition, during the solidification of cast composites, the reinforcement phase tends to segregate between the dendrites of the cast microstructure [25,26].

2.3. Corrosion of aluminum metal matrix composites

Similar to aluminum alloys, the predominant mode of corrosion for MMCs in seawater is not general corrosion, but localized corrosion [27]. The density of pits on a MMC has been reported to be greater than on the matrix alloy for the same immersion conditions. Pits on the MMCs are reported to be uniform, shallow and widespread [22], and the increased number of

pits is attributed to the crevice formed at each matrix-reinforcement interface [28- 30]. It is believed that the corrosion on the MMC is greater due to coupling between the reinforcement acting as a cathode site and the aluminum matrix [31]. Anodic and cathodic polarization was measured for SiC, using mixed potential theory; the corrosion current density was estimated for the matrix coupled to an equal area of SiC and was 2.5 times larger than the matrix alone [4].

It has been proposed that pits initiate at the interface between the matrix and the reinforcement. However, studies by a number of authors indicate that this interface is not the preferential site for pit nucleation [26,32].

As in aluminum alloys, it has also been suggested that pits initiate at flaws in the oxide film formed on the aluminum matrix of the composites [33]. It appears that pits initiate at second phase precipitates in the matrix [13,27]. These second phase precipitates were smaller and greater in number on the MMC than in the unreinforced matrix [34]. It is suggested that pitting sites result from elemental segregation and precipitation of impurities during forming [35].

2.4. Electrochemical techniques

The main variables that are measured in an electrochemical test are the voltage and the current. The goal is to translate this information into a corrosion rate or some other information that describes the corrosion process as described in different standards such as ASTM G5 [36], ASTM G3 [37], ASTM G61 [38]. In this study, Potentiodynamic

Polarization measurement and Electrochemical Impedance Spectroscopy were used to characterize the corrosion behavior of the MMCs. The theoretical background of these techniques is presented here.

2.5. Potentiodynamic Polarization Curve

Measurement of current density is the most common output of electrochemical corrosion testing [39]. This quantity is usually related either to the corrosion rate or some feature of the corrosion process, such as surface redox reactions that change the corrosion characteristics [40]. Polarization measurements are a common technique in electrochemistry and corrosion science. A corrosion reaction consists of two half-cell reactions. The anodic reaction is an oxidation reaction and the cathodic reaction is a reduction reaction. The cathodic reaction in a neutral aqueous solution is the reduction of oxygen [41]. The anodic and cathodic reactions for Al in neutral, aqueous solutions are [42]:

$$Al \rightarrow Al^{3+} + 3e^{-} \qquad E^{o} = -1.66V$$

Equation 1

$$O_2 + 2H_2O + 4e^{-} \rightarrow 4OH^{-} \qquad E^{o} = 0.401$$

Equation 2

Both the anodic and cathodic reactions have a reversible potential, E^{o}, at which the rate of the forward reaction is equal to the back reaction for that half-cell reaction. When aluminum is exposed to a solution with O_2, the anode will be polarized toward the cathode and the cathode will be polarized toward the anode [43].

The corrosion potential, E_{corr}, will be at the intersection of anodic polarization curve with the cathodic polarization curve. At the corrosion potential, the current from the anodic reaction will exactly equal the current from the cathodic reaction [44]. To polarize the cell away from E_{corr}, an external current (or potential) source must be inserted. The excess current (or voltage) supplied is recorded. By polarizing to a more positive potential (anodically) from E_{corr}, the anodic reaction will dominate and the current supplied will be the anodic current at the given potential. Similarly, polarizing to a more negative potential (cathodically) allows the study of the cathodic reaction. For potentiodynamic polarization curves, the potential is varied at a given rate and the current supplied by the potentiostat is recorded. Typical anodic and cathodic polarization curves are shown in Figure 2.2-1 [40]. Normally, the potential is plotted versus the logarithm of the current density, i. The intersection of anodic and cathodic polarization curves will be at E_{corr}. The cathodic polarization curve will typically show a limiting current due to mass transport limitations as given in Figure 2.2-2. The anodic polarization curve for Al typically shows a region where the current density is nearly independent of the potential. This is the passive region and it is due to the formation of a passive oxide film on Al as seen in Figure 2.2-3. The breakdown of the oxide and consequent initiation of pitting will take place at a characteristic potential referred to as the Pitting Potential, E_{pit}. At E_{pit}, the current density will show a sudden increase [4]. For Al alloys in aerated solutions, E_{pit} is near E_{corr} [45].

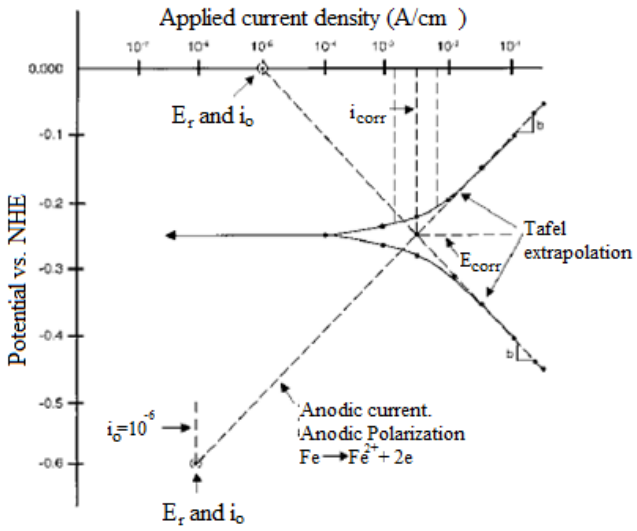

Figure 2.2-1. Polarization curve [40].

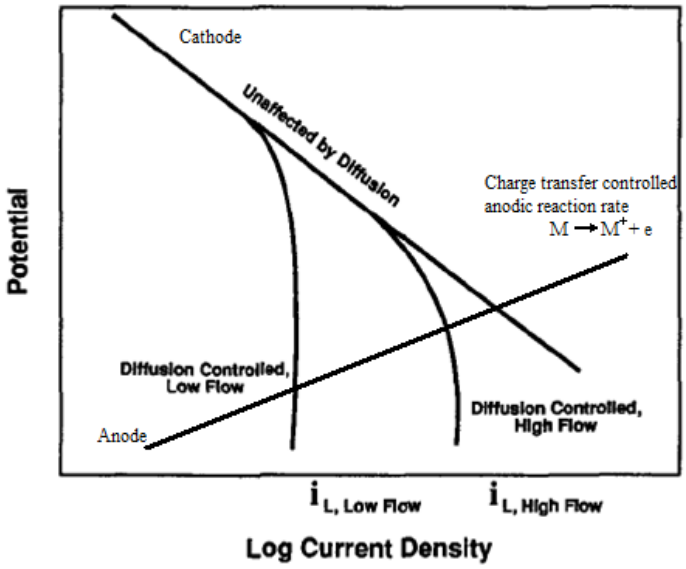

Figure 2.2-2. Evans diagram illustrating the influence of solution velocity on corrosion rate for a cathodic reaction under "mixed" charge transfer-mass transport control. The anodic reaction shown is charge transfer controlled [4].

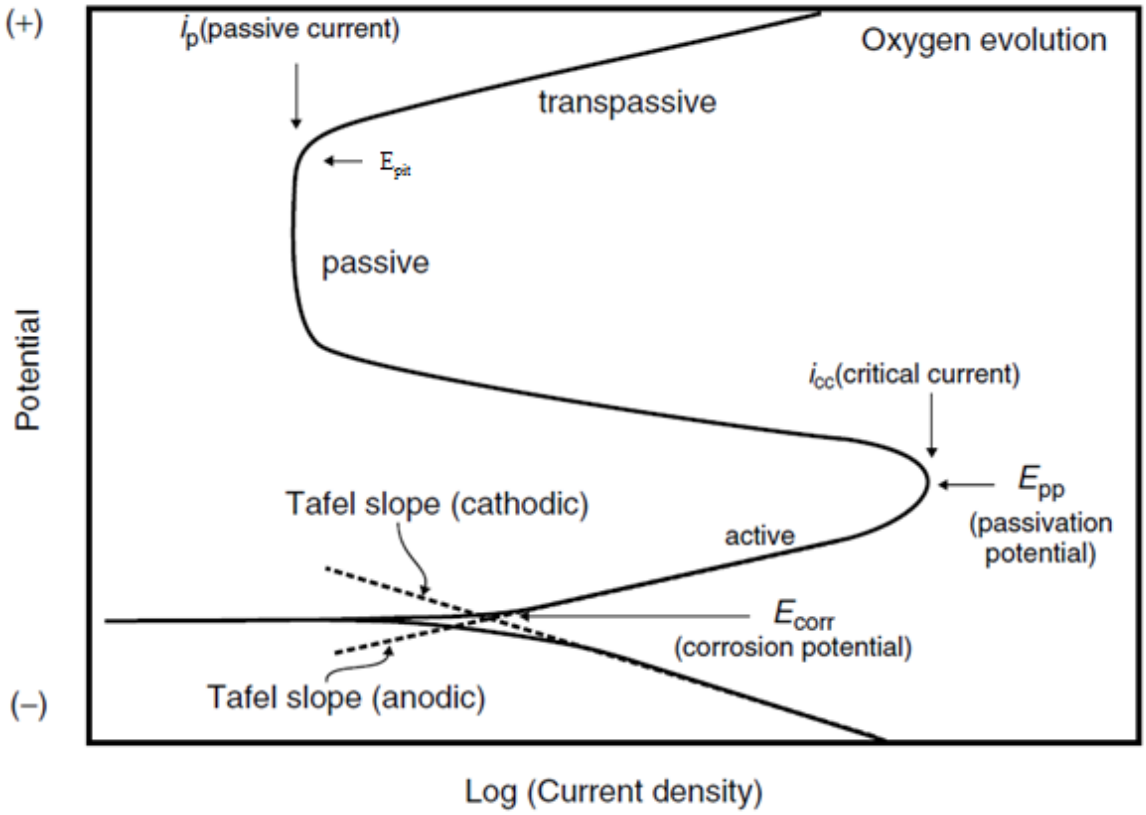

Figure 2.2-3. Generalized polarization diagram showing the various potential regions of a passive metal and Tafel extrapolation lines [4].

In this work, potentiodynamic polarization was carried out anodically and cathodically in aerated 3.5% NaCl solution to determine the pitting potentials and the passive current densities for the Al alloys and Al-Al_2O_3 MMCs.

2.6. Electrochemical Impedance Spectroscopy (EIS)

EIS has rapidly developed into an important technique for corrosion science and technology [44]. The increasing use of EIS in corrosion science and electrochemistry has led to the

publication of a number of excellent reviews of methods and techniques for measuring and analyzing EIS data [46]. EIS is a non-destructive technique that is suitable for in-situ monitoring of many corrosion processes [47]. EIS uses a small amplitude signal applied to an electrochemical cell to measure the impedance over a wide frequency range usually in the 1 MHz to the 1 mHz range [48]. It allows the study of many high impedance systems which were inaccessible with traditional DC electrochemical techniques [49]. In addition, DC techniques use polarization which can sometimes be large enough to change the properties of the system under study [46,50]. EIS uses a small signal, which is also necessary to ensure that the system response is linear [47].

The system impedance is measured around a fixed potential. To minimize damage to the electrode, this potential is commonly the open circuit potential. The impedance of the system is measured by applying a small amplitude perturbation to the system and measuring the response. Commonly, a sinusoidal voltage signal is applied and output is a current. The impedance may then be calculated as the input voltage divided by the output current taking into account that both the input and output parameters are vectors with a magnitude and phase [51]. The frequency is varied during the measurement and the impedance is recorded as a function of frequency. With modern Frequency Response Analyzers (FRA), the data is converted to the frequency domain via a Laplace Transform. The FRA calculates the impedance and records the impedance as a function of frequency. The impedance is a complex quantity with both a modulus and phase angle in the complex plane. Alternately, the impedance can be represented as a real and imaginary impedance component [52].

Impedance data may be displayed in a number of different forms. The two most common forms are the Bode plot (Figure 2.2-4) and the Nyquist plot (Figure 2.2-5). In the Bode representation, the phase angle, ϕ, and the logarithm of the impedance modulus, |Z|, are plotted versus the logarithm of the frequency, ω [48]. The Nyquist plot, on the other hand, displays Z_{im} vs Z_{Re} for different values of ω [49].

The analysis of impedance data requires appropriate models based on the physical and chemical properties of the system under study. Modeling of the system with equivalent circuits allows the data to be numerically analyzed. In Equivalent Circuit Modeling (ECM), the system is modeled by a network of resistors, capacitors and inductors which are correlated to the physical and electrochemical properties of system [40].

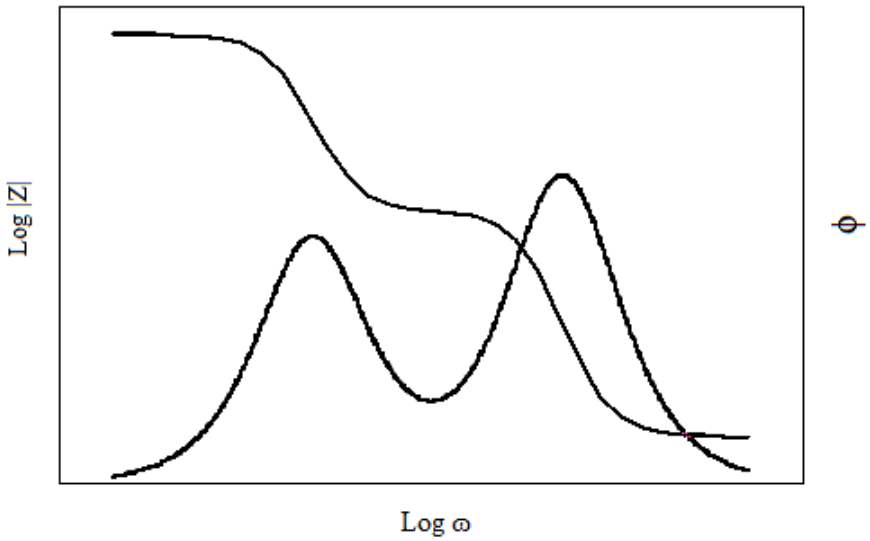

Figure 2.2-4. Graphical impedance presentation Bode plots [51].

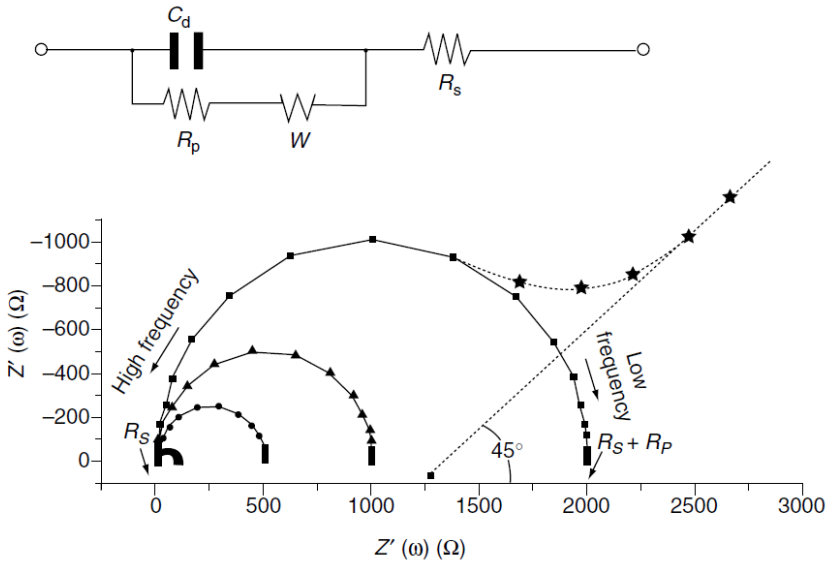

Figure 2.2-5. Faradaic impedance spectra presented in the form of Nyquist plots along with the electronic equivalent circuit of the electrified interface [40].

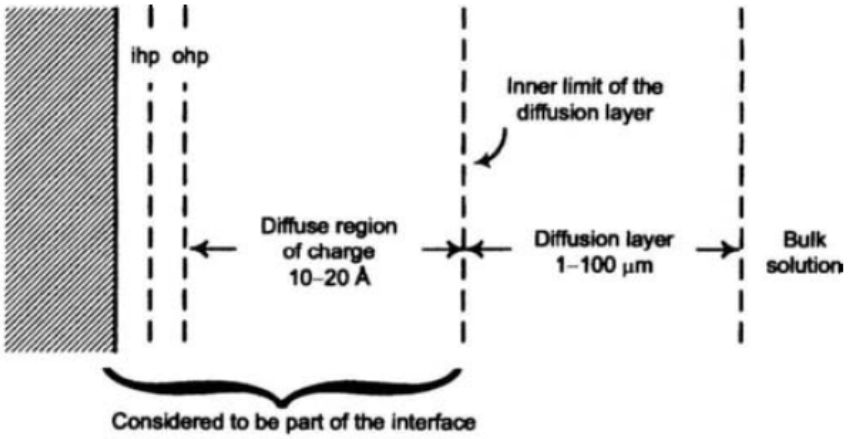

Figure 2.2-6. The structure of the electrical double layer; where ihp refers to inner Helmholtz plane and ohp refers to outer Helmholtz plane [50].

A simple example of an ECM is the model for a charge transfer controlled reaction in Figure 2.2-5 [50]. R_s accounts for the ohmic resistances in the system. C_{dl} and R_p model the electrochemical interface. C_{dl} represents the double layer capacitance at the metal-electrolyte

interface. The double layer is an array of dipoles and charged particles at the corroding interface, Figure 2.2-6 [52]. R_p is referred to as the polarization resistance. The corrosion rate is inversely proportional to the polarization resistance [49]. The impedance of this simple ECM is given as [51]:

$$\boldsymbol{Z = R_s + \frac{R_p}{1 + j\omega C_{dl} R_p}}$$

Equation 3

Insertion of Z' and Z" in place of Z and rearrangement leads to:

$$\boldsymbol{(Z' - R_s - {}^{R_p}/_{2})^2 + (Z'')^2 = ({}^{R_p}/_{2})^2}$$

Equation 4

This is the equation for a circle in the Z"-Z' plane (Nyquist format) with R_p as the diameter. Alternately, the impedance may be plotted in the Bode format. In the Bode format, the capacitor will act as a short circuit at high frequencies and R_s will be seen. At intermediate frequencies, the impedance is dominated by C_{dl} and the impedance will vary as the inverse of the frequency. At low frequencies, the capacitor will act as an open circuit and impedance will be the sum of R_s and R_p [53].

Frequently, in regions where a capacitance is dominating, the impedance will show non-ideal behavior. The impedance of an ideal capacitor would vary as the inverse of the frequency. In the Bode format, an ideal capacitor would have a slope of -1 in the modulus plot and a phase angle of 90^o, Figure 2.2-7.

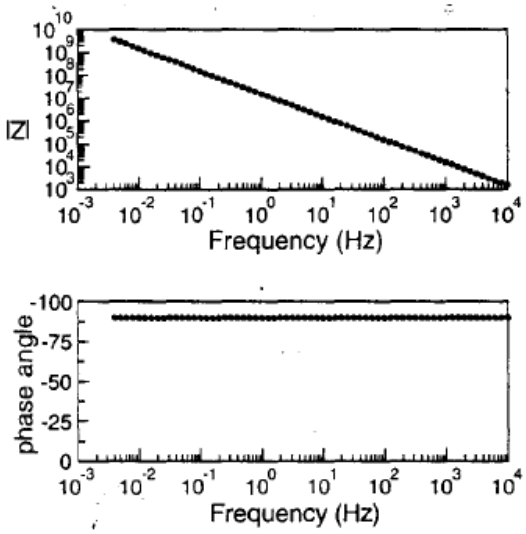

Figure 2.2-7. Ideal impedance behavior of a capacitor [47].

The capacitance may be expressed as:

$$\boldsymbol{C = \varepsilon \varepsilon_o A/d}$$

Equation 5

Where ε is the dielectric constant of the material, ε_o is the permittivity of free space, A is the area normal to current flow and d is the thickness of the dielectric material [54]. In the most general case, ε is considered to be function of frequency and a complex number with both real and imaginary components [54]. Therefore, a real capacitor may not exhibit a constant capacitance over a wide frequency band. This has been observed in many corrosion studies. Frequently, the Nyquist plot will show a depressed semicircle and the Bode plot will show a phase angle less than 90^o with the absolute value of the slope in the modulus plot less than 1. Many reasons have been proposed for this behavior including surface roughness, frequency dispersion of time constant due to local in-homogeneities in the dielectric material, porosity,

mass transport effects and relaxation effects [47,55]. In order to account for these effects, non-ideal capacitors are proposed whose impedance can be expressed as [56]:

$$\boldsymbol{Z_c = (j\omega C)^{\alpha}}$$

Equation 6

The value of α for an ideal capacitor is -1. This model is only valid for absolute values of α greater than 0.80 [47].

ECMs have been developed for a number of frequently studied systems. ECMs allow the system to be characterized in terms of circuit elements with a physical significance. With the use of appropriate software, numerical fits of the ECMs to the experimental data may be performed. The analysis presented in this thesis was performed using ECHEM ANALYST commercial software developed by GAMRY. This software uses a non-linear least squares fit methodology to vary the fit parameters to minimize the error between the fitted result and the experimental data [57].

3 EXPERIMENTAL

This chapter describes the materials used in this work, the details of sample preparation, the parameters used in the electrochemical testing and the analytical microscopy techniques utilized in this research.

3.1. Materials

The aluminum matrix composites evaluated in this investigation were XT1129 alloy reinforced with 10 vol.% of Al_2O_3 particles, XT2009 alloy reinforced with 15 vol.% of Al_2O_3 particles, XT2048 alloy reinforced with 20 vol.% Al_2O_3 particles and XT2031 alloy reinforced with 25 vol.% Al_2O_3 particles. The powder metallurgy route used for processing the MMCs involves blending of the aluminum alloy powder and the Al_2O_3, hot consolidation and followed by extrusion to provide a billet having circular cross-section. Details of the processing technique are considered to be proprietary by the manufacturer. These composites were supplied in the form of 16 mm diameter rods and were about 300 mm long. AA1100-O alloy and AA2024-T3 alloy without reinforcement served as the monolithic materials for comparison. These alloys are used because they have a chemical composition similar to the matrix of MMCs. Sample disks of 16 mm diameter and 2 mm thick were prepared from the as-received composite materials and monolithic materials.

The chemical composition of the composites is not known accurately. From review of literature nominal compositions for alloy AA2009, AA2031, AA2048, AA1100 and AA2024 were encountered and these are tabulated in Table 3-1. The nominal composition of AA1129

aluminum alloy could not be determined. However, all these alloys are derivations from AA 2024.

Table 3-1. Chemical composition of monolithic and matrix alloys (elements wt.%) [58,59].

Material	Si	Fe	Cu	Mn	Mg	Cr	Zn	Specified other elements	Ti	Al minimum
AA1100	0.95 (Si+Fe)		0.05-.20	0.05	-	-	0.10	(a)	-	99.00
AA2024	0.5	0.5	3.8-4.9	0.3-0.9	1.2-1.8	0.1	0.25	(k)	0.15	Rem
AA2048	0.15	0.20	2.8-3.8	0.2-0.6	1.2-1.8	-	0.25	-	0.10	Rem
AA2031	0.5	0.6-1.2	1.8-2.8	0.5	0.6-1.2	-	0.6-1.4	-	0.20	Rem
AA2009*	0.25	0.07	3.2-4.4	-	1.0-1.6	-	0.1	0.15	-	Rem

a) 0.008 Be max for welding electrode and filler wire only.

k) A (Zr+Ti) limit of 0.20% maximum may be used for extrude and forged product.

3.2. Corrosion testing

3.2.1 Cyclic polarization

For corrosion testing, the cyclic polarization technique was used. The measurements were carried out in a 3.5% NaCl aqueous solution at room temperature in a Pyrex glass cell exposed to atmospheric air with graphite counter electrodes. The potential was controlled with a GAMRY PC300 potentiostat and measured through a Luggin capillary with reference to a saturated calomel electrode (SCE). Deaeration of the solution did not take place. The Al-Al_2O_3 composite material samples served as the working electrode. For all tests, three samples of each Al-Al_2O_3 composite material were tested in order to ensure good reproducibility of the results. These were cut from the as-received rods using a slow speed diamond saw to obtain disks with 2 mm thickness. The specimens were ground successively using 240 to 600 grit SiC papers using standard metallographic techniques and finally ultrasonically cleaned using ethanol to degrease them. Afterward, each sample disk was mounted in the Teflon gasket end of the rod and immersed into the solution. The exposed area of the samples was about 1 cm^2. It was left in the solution for about 2000 seconds until a steady open circuit potential was reached. After equilibrium, potentiodynamic polarization was started at a rate of 1 mV/s. The cycle began at the cathodic over potential of -250 mV and the scan was reversed when the specimens reached the anodic corrosion current density of 2.5 mA/cm^2. The samples were potentiodynamically polarized until a potential of -150 mV was reached again.

3.2.2 Electrochemical Impedance Spectroscopy

Another set of specimens was used in order to study the corrosion processes occurring in these Al-Al_2O_3 composite materials using EIS measurements. An initial frequency of 100 KHz and a final frequency 1 mHz were used on an imposed AC sinusoidal voltage signal with a wave amplitude of 10 mV; 7 points per decade with a delay before integration of 10 s were recorded by the GAMRY potentiostat.

Different parameters of polarization curves and impedance diagrams such as E_{corr}, E_{OCP}, E_p, E_{rp}, I_{corr}, R_s, R_p, CPE were derived from software DC105 and EIS300 of GAMRY INSTRUMENTS®, respectively using curve fitting methods.

3.3. Analytical Microscopy

A sample of each of the four metal matrix composites was subjected to standard metallographic grinding from 240 to 600 grit, then polished with alumina suspension of 5 and 3 μm, in that order and finally cleaned in an ultrasonic cleaner using isopropyl alcohol to degrease the sample. The sample was then sputter-coated with a thin gold film for observation in the SEM. The SEM observations were performed with secondary electrons and back-scattered electrons to assess the distribution of alumina particles, inter-metallic compounds and/or elements of second phase. Energy Dispersive X-ray Analysis (EDS) analysis was performed to determine the elements present in the composite.

The samples after cyclic polarization, EIS and OCP testing were washed in distilled water in an ultrasonic cleaner to remove the remnant 3.5% NaCl solution from the sample, rinsed with isopropyl alcohol and then observed initially by optical microscopy. These were later coated with gold and observed in the SEM in secondary electrons and back-scattered electron modes, as well as subjected to EDS analysis.

Chemical composition of specific microstructural features, as well as the line scanning and X-ray map acquisition were determined by CDU leap Detector EDAX, attached to the JEOL JSM 5800 LV scanning electron microscope (SEM). Energy Dispersive X-ray Spectroscopy (EDS) was used in a point mode to identify copper content inside and around the pit.

The study of pitting morphology was carried out using an NIKON ECLIPSE 80i optical microscope.

4 EXPERIMENTAL RESULTS AND DISCUSSION

EIS was used to study the response of as-received samples after immersion in 3.5% NaCl solution. The EIS results were supplemented by observation of surfaces after immersion with optical microscopy and visual observation of the surfaces during immersion. Potentiodynamic polarization measurement was recorded to determine the pitting potential and the cathodic reaction kinetics of the as-received materials. In addition, SEM with EDS was used for selected samples.

The objectives of the present study were to investigate the corrosion behaviour and the influence of alumina particles on corrosion behaviour of the MMC. Corrosion initiation sites were identified by monitoring changes in the surface morphology of MMC and monolithic aluminum specimens. Mapping of corrosion current density at corrosion sites was observed to study the propagation of localized corrosion. Polarization experiments were conducted to evaluate the corrosion performance. In this chapter, the experimental results will be presented concurrently with a technical discussion of the observations.

The electrochemical parameters measured for Al_2O_3 reinforced Al-Metal Matrix Composites, using Open Circuit Potential (OCP), Cyclic Polarization (CP) and EIS are each considered separately.

4.1. SEM observation

The microstructures of the metal matrix composite, before immersion, obtained with secondary and back-scattered electrons respectively in the SEM, are shown in Figure 4-1.

All analyses were carried at 20 keV accelerating voltage; this value is common in EDS analysis and represents the minimum value to produce x-rays. The x-ray spatial resolution for beam energy of 20 kV is 3-4 μm in an aluminum based matrix. Since the analyses employed low dead-time (less than 25%), the peak shape for low energy range (<1 keV) was mainly Gaussian. Sum peaks and silicon escape peaks were considering during qualitative analyses.

The calibration of SEM-EDS system was verified using a standard sample which is a copper grid embedded in a piece of pure aluminum. Conventional EDS analysis can reach analytical precision of 1-2 % of reported concentration values. All spectra were obtained using electron beam energy of 20 keV and a take-off angle of 35 degrees between the EDS detector and the surface of specimen was selected. To minimize errors, ZAF corrections were automatically computer-performed by the EDAX software.

Nevertheless, the EDS analysis performed on the samples in the present study cannot be considered “conventional”. First, all the samples were not homogeneous over the electron range, and this fact induces an error during quantification. Second, corrosion testing of the samples increased their roughness and consequently, they should not be considered as sub micrometric flat-polished samples. Furthermore, great errors can be introduced due to x-ray absorption and this significantly affects the quantification of light elements.

The secondary electron images show that the composites XT1129, XT2009 and XT2048 are reinforced with spherically shaped Al_2O_3 particles with a particle size ranging from 2 to 6 µm. The XT2031 composite, on the other hand, is reinforced with irregular shaped Al_2O_3 particles, whose size which varies from 2 to 6 µm, is estimated from the SEM micrographs.

EDAX analysis carried out in different areas of the sample are shown in Table 4-1 to Table 4-4 indicating elements such as oxygen, magnesium, copper and silicon as major alloying elements. The zones analyzed (marked with letters A through E) were white particles, gray particles, at the periphery of the particles, holes from which particles appear to have fallen out and matrix which are of interest in this discussion.

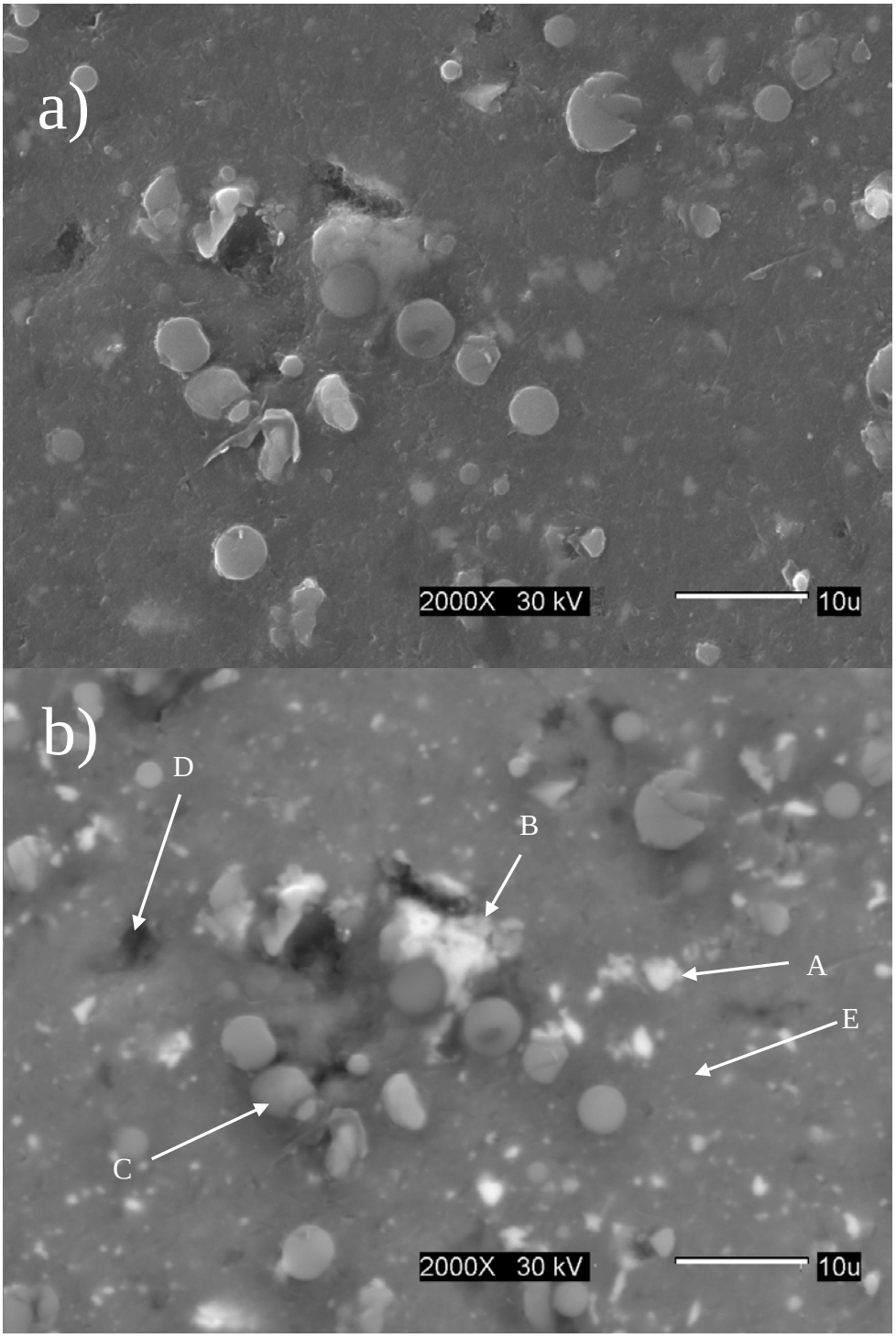

Figure 4-1. Micrographs of metal matrix composites obtained with the SEM with secondary electrons: a) XT1129, c) XT2009, e) XT2031, g) XT2048; and back-scattered electrons: b) XT1129, d) XT2009, f) XT2031, h) XT2048.

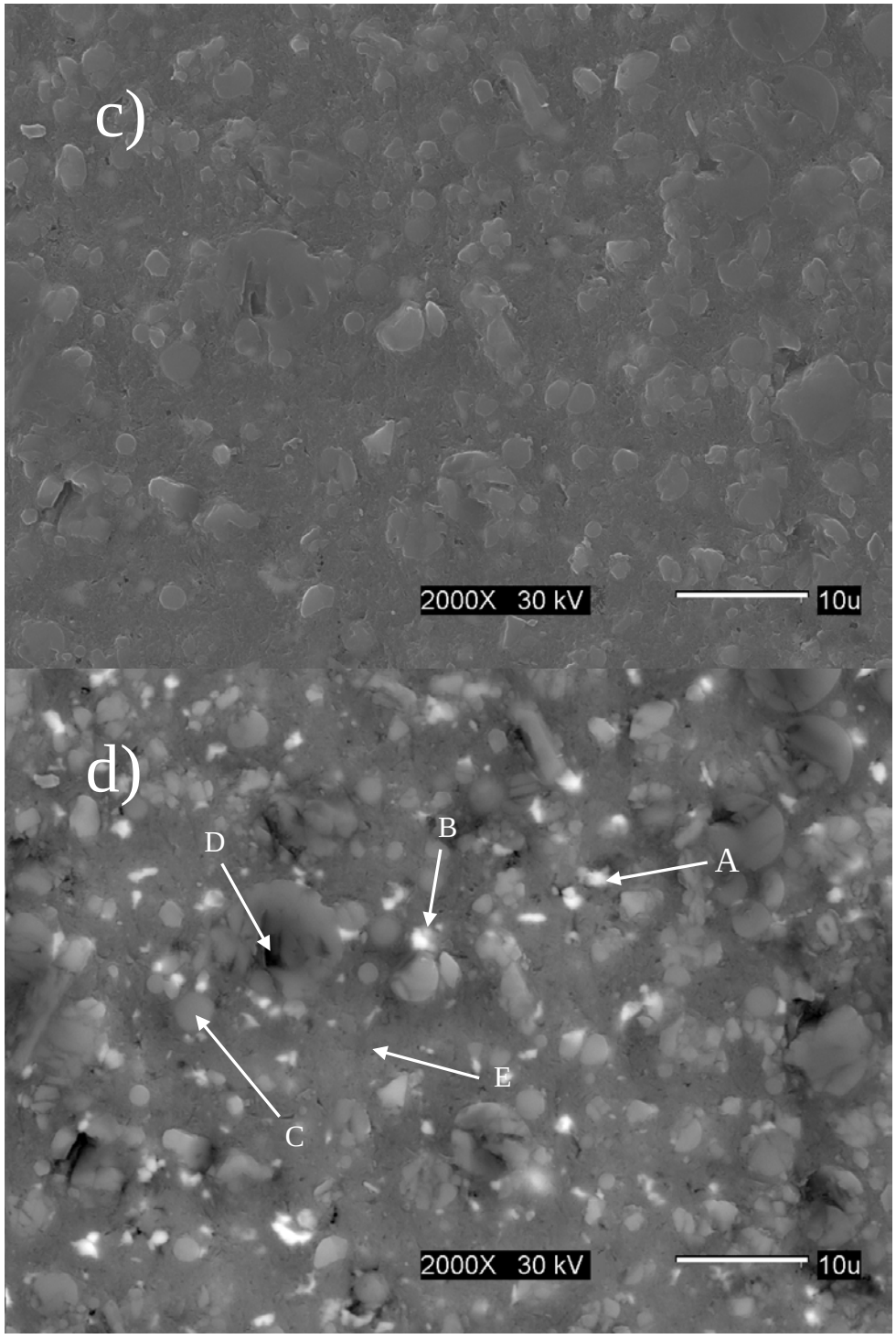

Figure 4-2. (Continued). Micrographs of metal matrix composites obtained with the SEM with secondary electrons: a) XT1129, c) XT2009, e) XT2031, g) XT2048; and back-scattered electrons: b) XT1129, d) XT2009, f) XT2031, h) XT2048.

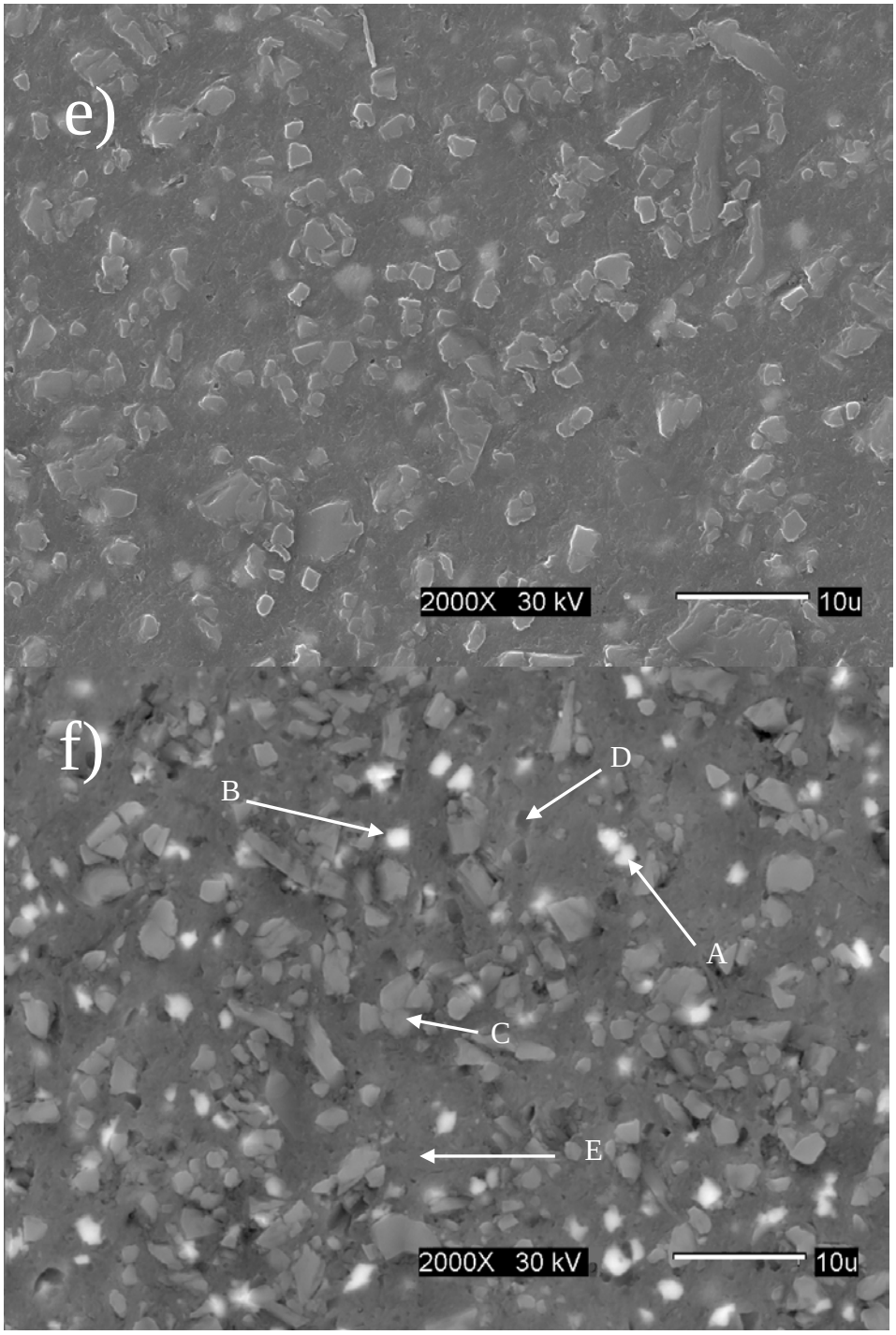

Figure 4-3. (Continued). Micrographs of metal matrix composites obtained with the SEM with secondary electrons: a) XT1129, c) XT2009, e) XT2031, g) XT2048; and back-scattered electrons: b) XT1129, d) XT2009, f) XT2031, h) XT2048.

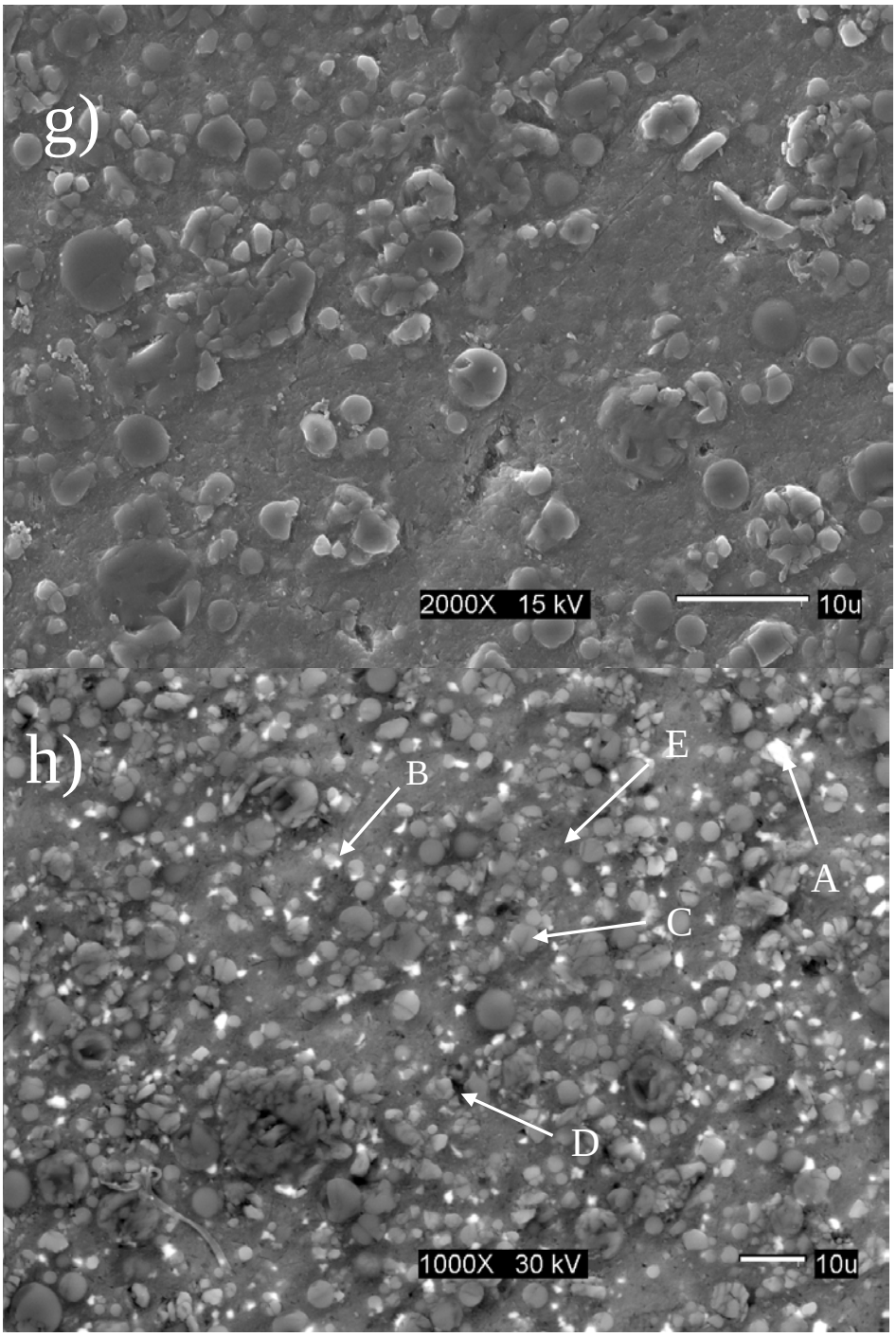

Figure 4-4. (Continued). Micrographs of metal matrix composites obtained with the SEM with secondary electrons: a) XT1129, c) XT2009, e) XT2031, g) XT2048; and back-scattered electrons: b) XT1129, d) XT2009, f) XT2031, h) XT2048.

Table 4-1. Results of EDAX analysis of metal matrix composite XT1129, areas A, B, C, D and E are shown in Figure 4-1-b.

Area	O (%At.)	Mg (%At.)	Al (%At.)	Cu (%At.)	Si (%At.)
Irregular white particle (A)	5.01	1.70	90.13	3.16	N.D.
Round white particle (B)	39.62	0.92	58.43	1.03	N.D.
Gray particle (C)	1.92	4.98	88.70	3.73	0.68
Black hole (D)	9.11	2.11	84.47	2.79	1.52
Matrix (E)	0.33	0.71	97.36	1.60	N.D.

Table 4-2. Results of EDAX analysis of metal matrix composite XT2009, areas A, B, C, D and E are shown in Figure 4-2-d.

Area	O (%At.)	Mg (%At.)	Al (%At.)	Cu (%At.)	Si (%At.)
Irregular white particle (A)	7.01	1.32	79.83	11.83	N.D.
Round white particle (B)	7.93	2.55	85.98	3.37	0.17
Gray particle (C)	18.24	1.55	76.53	3.48	0.18
Black hole (D)	7.93	2.55	85.98	3.37	0.17
Matrix (E)	8.58	1.22	87.87	2.32	N.D.

Table 4-3. Results of EDAX analysis of metal matrix composite XT2031, areas A, B, C, D and E are shown in Figure 4-3-f.

Area	O (%At.)	Mg (%At.)	Al (%At.)	Cu (%At.)	Si (%At.)
Irregular white particle (A)	1.37	1.13	89.30	4.06	4.14
Round white particle (B)	1.61	2.04	87.50	2.98	5.87
Gray particle (C)	2.40	1.33	40.71	1.07	54.49
Black hole (D)	1.45	1.38	74.10	1.47	21.59
Matrix (E)	1.81	1.39	90.20	2.12	4.48

Table 4-4. Results of EDAX analysis of metal matrix composite XT2048, areas A, B, C, D and E are shown in Figure 4-4-h.

Area	O (%At.)	Mg (%At.)	Al (%At.)	Cu (%At.)	Si (%At.)
Irregular white particle (A)	3.23	1.51	89.95	5.10	0.21
Round white particle (B)	34.15	1.43	63.00	1.15	0.26
Gray particle (C)	31.72	1.65	65.89	0.63	0.11
Black hole (D)	30.55	6.21	61.03	1.23	0.98
Matrix (E)	2.73	1.38	93.36	2.10	0.43

The white particles, A, have a high copper content, indicating that these particles are intermetallic aluminum-copper. The presence of the other elements from the EDS spectrum

is due to interference from the near-adjacent areas because of the relationship between particle size and minimum area of electron analysis. The analysis area is based on the electron beam width of 2 μm while the size of these particles is less than 2 μm [60].

A number of microstructural features are observed which are discussed below since they may be relevant to the observed corrosion behavior of the metal matrix composites in this study. The analysis of spherical particles, C, in the Al-Al_2O_3 composites XT1129, XT2009 and XT2048 confirms that these are indeed aluminum oxide reinforcement; the presence of silicon around the particle suggests that this was coated with silicon prior to fabrication of the composite. Precipitation of magnesium aluminate spinel ($MgAl_2O_4$) during the processing is also highly feasible because the affinity of magnesium for oxygen can reduce oxides present, [61]. $MgAl_2O_3$ formation produces a plastic incompatibility between the matrix and the particle [62] and the Mg-rich interface provides a nucleation site for localized corrosion by forming a local galvanic cell with the adjoining Al matrix [23]. The formation of intermetallic Mg_2Si in these composites results in improved resistance to corrosion, because the reaction products inhibit the corrosion process [63], and avoid Al_2O_3 precipitation which is the main cause of intergranular corrosion, exfoliation and SCC [64].

The analysis of the particles C of the XT2031 Al-Al_2O_3 composite shows a combination of aluminum and silicon. These compounds have very good dimensional stability [65]. The presence of SiO_2 and Al_2O_3 and Mg in the aluminum matrix during the manufacturing process promotes reactions such as [66]:

$$\frac{3}{4}SiO_2 + 2Al \rightarrow Al_2O_3 + \frac{3}{4}Si_{(in|Al)}$$

Equation 7

$$SiO_{2(s)} + 2Mg_{(l)} \rightarrow 2MgO_{(s)} + Si_{(in|Al)}$$

Equation 8

$$Mg_{(l)} + 2Al_{(l)} + 2SiO_{2(s)} \rightarrow MgAl_2O_{4(s)} + 2Si_{(in|Al)}$$

Equation 9

The presence of Mg develops an outer layer, assumed to be Al-rich $Mg(OH)_2$ as a result of exposure to the aqueous solution results in enhanced corrosion resistance [35].

The area B is the interface of the white particle with the matrix and the presence of Si was not detected in the XT1129 and XT2009 composites. Si was also not detected in area E, thus confirming that the reinforcement particles were probably coated with silicon before composite processing. For XT2031 and XT2048 composites, however, the presence of silicon was detected, both in the matrix as well in area B, indicating that silicon is an alloying element in these cases. Area D in the Al-Al_2O_3 composites XT1129, XT2009 and XT2048 are cavities or porosity, while for the XT2031 composite these correspond to particles detached from the matrix during metallographic preparation.

4.2. Potentiodynamic Polarization measurements

Polarization measurements were made for AA1100 and XT1129 in 3.5% NaCl solution, with the anodic and cathodic measurements performed in aerated solutions. Open Circuit Potential (E_{OCP}) measurements were conducted in the same medium too. The variation of potential

(E_{OCP}) under open circuit condition (OCP) as a function of time in 3.5% NaCl aerated solution for all the six materials are shown in Figure 4-5 and Figure 4-6 respectively, with the results for the OCP vs. time for the AA1100 and XT1129 composite in the former and AA2024, XT2009, XT2031 and XT2048 in the latter.

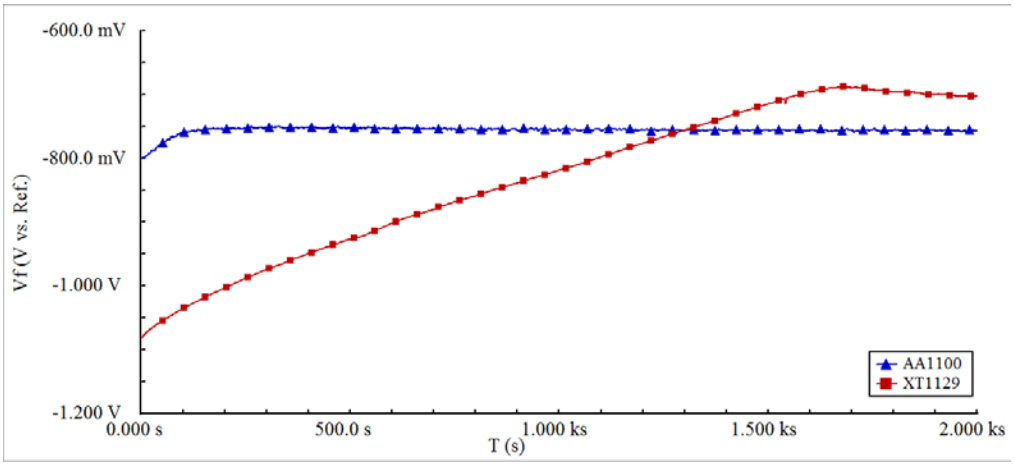

Figure 4-5. Open circuit potential (SCE) vs. time for aluminum metal matrix composite reinforced with 10 vol.% Al_2O_3 and AA1100.

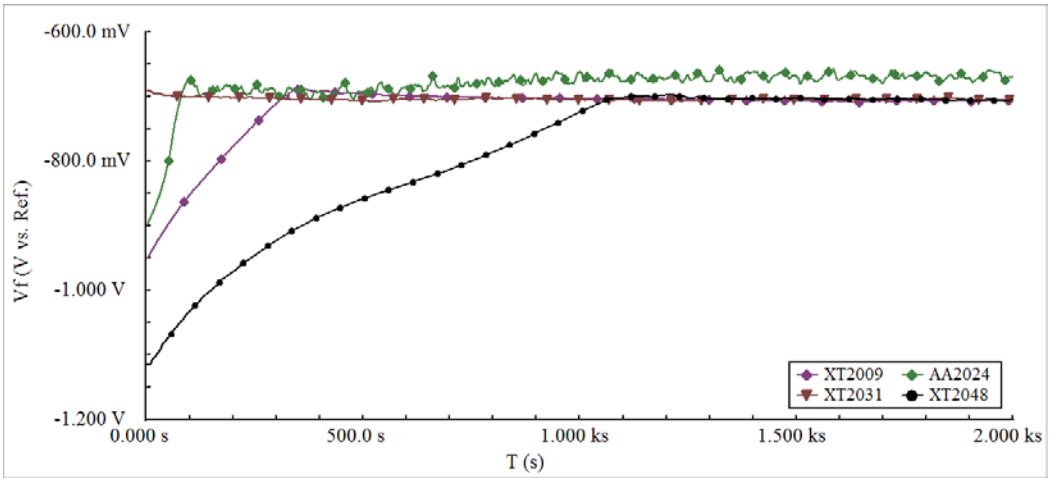

Figure 4-6. Open circuit potential (SCE) vs. time for aluminum metal matrix composite reinforced with 10 to 25 vol.% Al_2O_3 and AA2024.

The observed trend indicates that the four aluminum metal matrix composites have approximately the same OCP, which are listed in Table 4-5, while AA1100 shows the lowest value of E_{OCP} in the negative potential direction as compared to the composites. AA2024 alloy, on the other hand, shows maximum shift of the E_{OCP} in the positive direction as compared to the composite materials and AA1100. The manner in which the potential of the samples changes slowly from a more electronegative potential to a higher value after 2000 seconds, with the exception of the AA2031 composite is noticeable in this figure.

Dissolution potentials with respect to saturated calomel electrode (SCE) in natural seawater in motion at 25 ^{o}C for aluminum 1050A is -750mV; and AA2024 T3, T4 and AA1100 in NaCl solution according to ASTM G69 is -600mV and -740mV respectively [67]. These potentials are similar to the list in Table 4-5 which corresponds to the materials used in this study.

Table 4-5. Average values of the Open Circuit Potentials of AA1100, XT1129, AA2024, XT2009, XT2031, XT2048 in aerated 3.5% NaCl after 2000 s of immersion.

Material	**AA1100**	**XT1129**	**AA2024**	**XT2009**	**XT2048**	**XT2031**
E_{OCP}	-748.0	-711.1	-655.2	-711.3	-707.7	-706.7

The open circuit corrosion potentials (E_{OCP}) that have been obtained for the aluminum metal matrix composites reinforced with alumina particles in different percentages do not present significant variations among themselves, although there is some difference with the unreinforced aluminum alloys. This is attributed to similar matrix compositions since it is

expected that the reinforcement itself is not expected to affect the OCP values. Immersion in the 3.5 % NaCl solution which is chemically reactive with aluminum alloy, results in the intermetallic initially becoming more active than the matrix, giving rise to loss of metal in a process of selective corrosion (Equation 10). This in turn, causes the intermetallic to become enriched in Cu, thus making it more cathodic with a more noble potential as immersion time increases [14,22,64,68]. This is possibly reflected in the low initial OCP which rises to nobler values as immersion time increases.

Several optical microscope images are presented in Figure 4-11, after immersion for 10 h which show severe damage on the surface of the composites in Cl^- medium. Large pits were clearly visible on the surface exposed to Cl^- solution indicating susceptibility of the material towards pitting corrosion in Cl^- medium. Figure 4-11 b, c, e and f shown "halos" that form around pits, which indicate that Cu ions in the electrolyte are produced by alloy dissolution as soon as contact is initiated. As a result, Cu is enriched and deposited back on the unattacked matrix phase outside the bounds of the pit [64]. In homogeneous dissolution, both Al and Cu are dissolved during initial contact with the NaCl solution and it is assumed that copper atoms in the dilute alloy isolated by oxidation of the surrounding can temporarily enter the solution as ions [22]. Cu surface enrichment by the homogeneous dissolution mechanism shown by the chemical processes given below has been proposed in earlier studies [64,69,70]:

$$\boldsymbol{Al_2Cu \rightarrow 2Al^{3+} + Cu^{2+} + 8e^-}$$

Equation 10

$$Al \rightarrow Al^{3+} + 3e^{-}$$

Equation 11

$$Cu^{2+} + 2e^{-} \rightarrow Cu$$

Equation 12

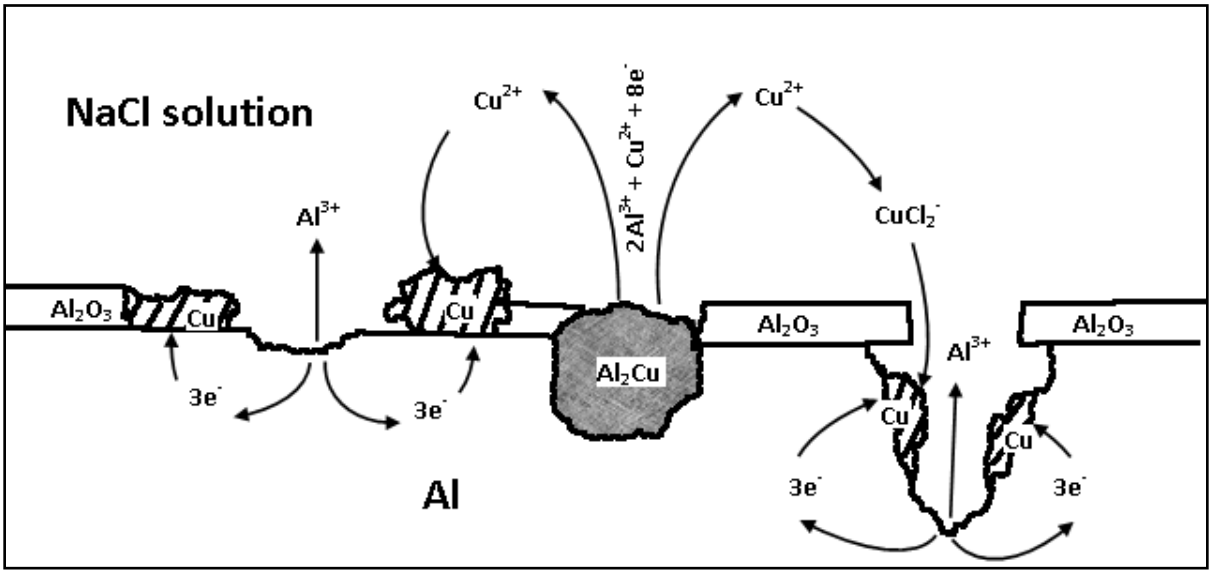

Figure 4-7. Schematic diagram illustrating copper deposition mechanism and role of chloride in forming copper cathode patches within a pit. Combined model from models proposed by Buchheit [64], Cervantes [69] and Obispo [70].

To produce effects as those observed in the current study, it is reasoned that some of the dissolved copper must be reduced in metallic contact with the aluminum on the film-free regions of the aluminum matrix surface in a transient pit which will be acting as anode. This transient pit will be produced by particles which were pulled off from the matrix. Figure 4-7 schematically illustrates the copper deposition mechanism. At anodic areas, Al^{3+} and Cu^{2+} ions are released from the alloy into the solution as the alloy corrodes (Equation 10). The production of Cu^{2+} in the diffusion boundary layer region probably reaches sufficient

concentrations to promote copper electrodeposition (Equation 12) at favorable (cathodic) sites on the surface. Electrons are conducted from dissolution sites to the deposition sites (Equation 11), allowing the Cu deposit to grow. A positive ion (i.e., Cu^{+} or Cu^{2+}) will tend to move away from the anode and out of the pit. In the presence of Cl^{-} the $CuCl_2^{-}$ anion can be formed, and the copper in this ion will move toward an anode position where it can be reduced in metallic contact with the aluminum [22]. In the present study, halos were formed around pits with a copper tone indicative of “deposition” of copper from the electrolyte after initial dissolution of the Al_2Cu intermetallic precipitates as seen in Figure 4-11.

Figure 4-8 shows the points where the analysis was performed, inside of pit (zone A) and around of pit (zone B) of the XT1129 MMCs after immersion in NaCl solution for 10h.

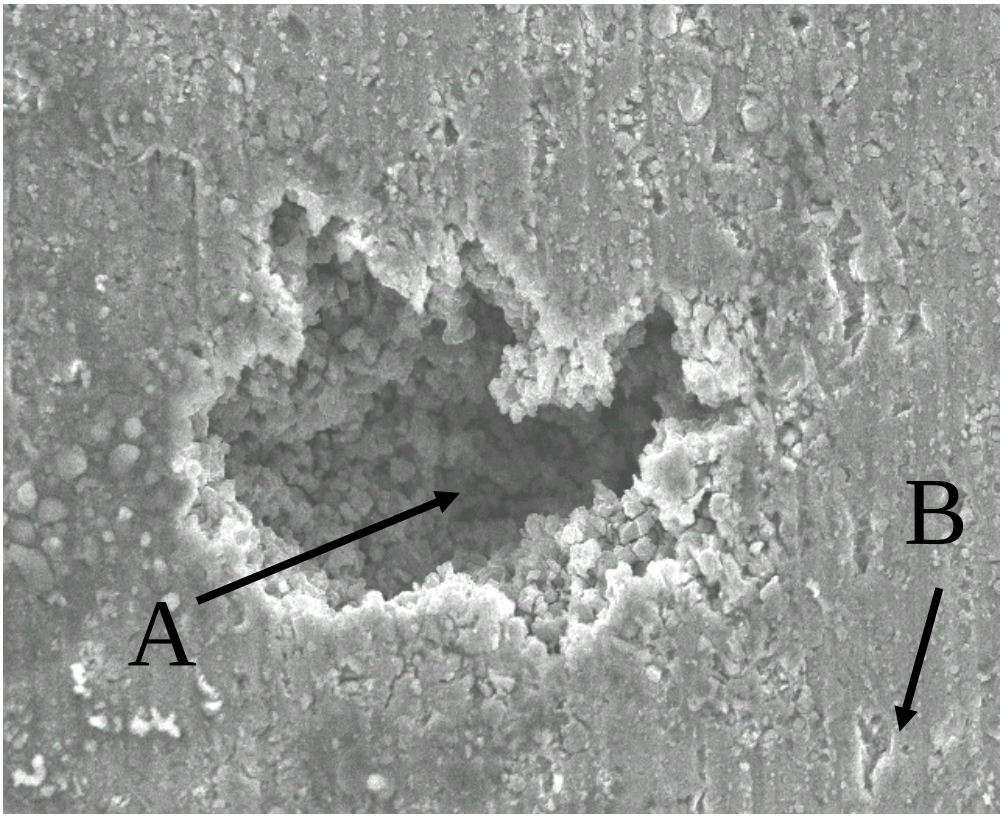

Figure 4-8. EDS analysis point of MMC XT1129 after immersion in NaCl solution for 10 h, 1000x.

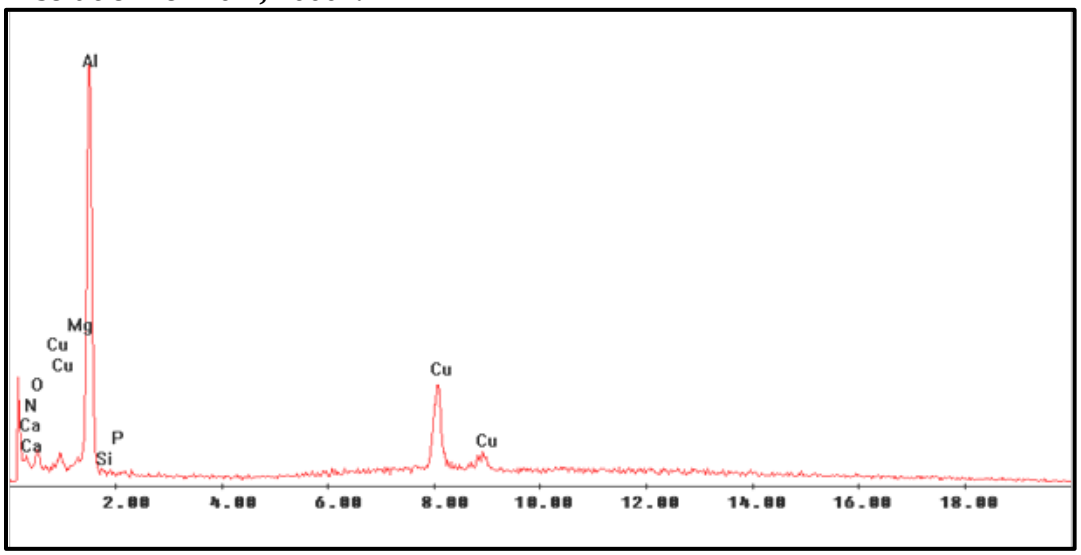

Figure 4-9. EDS intensities inside the pit, after immersion in NaCl solution for 10h.

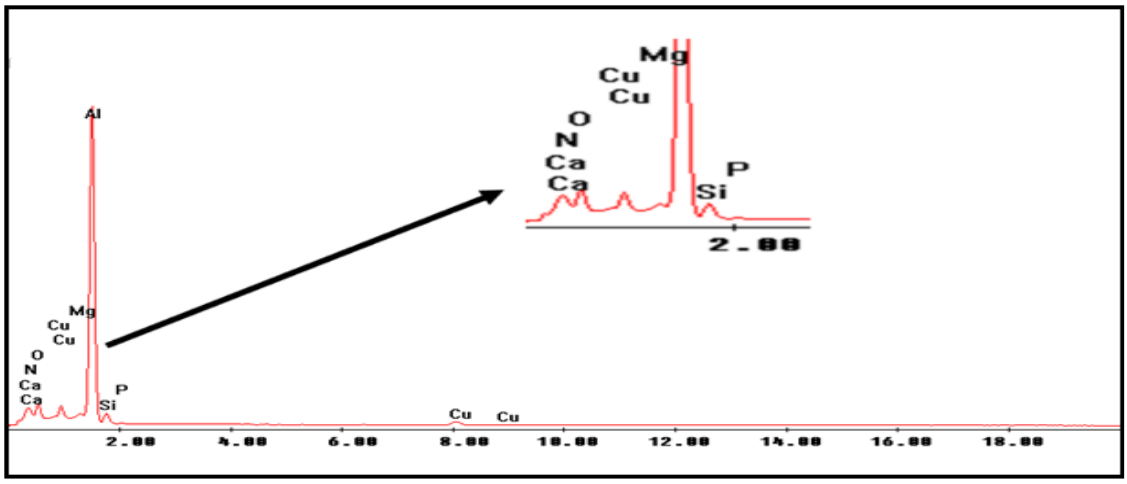

Figure 4-10. EDS intensities around the pit, after immersion in NaCl solution for 10h.

The EDS spectra shown in Figure 4-9 and Figure 4-10 reveal the presence of small amounts of copper inside the pit as well as in its surroundings. This provides evidence that there is copper dissolution and deposition, and that halos observed in Figure 4-11 are caused by the presence of copper deposited on the surface.

The results of EDS analysis of the MMCs XT1129, XT2009, XT2048, XT20031 and monolithic AA1100 and AA2024 are shown in the appendix A.

The topography of AA1100 alloy specimen immersed in NaCl solution for 10 h is revealed in Figure 4-11 a, which depicts cellular corrosion type, typical of Mg-Al alloys [35] and 1xxx series aluminum immersed in seawater [27,71]. However, OCP of Mg-Al alloys is between 1400 and 1550 mV in NaCl solution while the potential this case is closer to -750 mV which is roughly close to that of AA1100 alloy.

In Figure 4-11 d, which shows the AA 2024 sample immersed in NaCl solution for 10 h, both pitting and inter-granular corrosion (IGC) can be seen. This suggests that IGC of

AA2024 is a time dependent phenomenon and that there is an incubation time associated with the onset of IGC. The pits that are formed on the surface do not appear to grow very deep and may be associated with intermetallic particles in the matrix [22,72].

Aluminum alloys in which the intergranular precipitates are markedly more noble than the matrix phases (e.g., Al-Cu base alloys with Al_2Cu intergranular precipitates), or alloys in which the precipitates are markedly more electronegative (e.g., Al-Mg alloys and Al-Zn-Mg base alloys with Al_3Mg and Zn_2Mg intergranular precipitates, respectively) may be susceptible to severe intergranular corrosion [73]. The mechanism of the intergranular corrosion in these alloys is primarily electrochemical, involving local cell reaction between grain boundary, precipitates and the adjacent matrix. The precipitates corrode preferentially, and the degree of susceptibility to intergranular attack depends on the nature, amount, size and distribution of the intergranular precipitates.

Aluminum significantly modifies its OCP when adding Al_2O_3 particles as reinforcement ratios from 10 to 25% in volume. In case of Al-Cu alloy the value of OCP moves to less noble potentials. The Al_2O_3 particles allow the anchoring of dislocations formed during the process of forming or deformation of the composites, which along with grain boundaries are preferential sites for precipitation of intermetallic. This allows the formation of a finer precipitate which is homogeneously distributed in the composite. Thus, the nucleation centers of the pits are greater in number in the MMC than in Al-Cu alloy. Hence pit nucleation can occur across the surface of the composite and give the appearance of a generalized corrosion process, as can be seen in Figure 4-11 b, c, e and f.

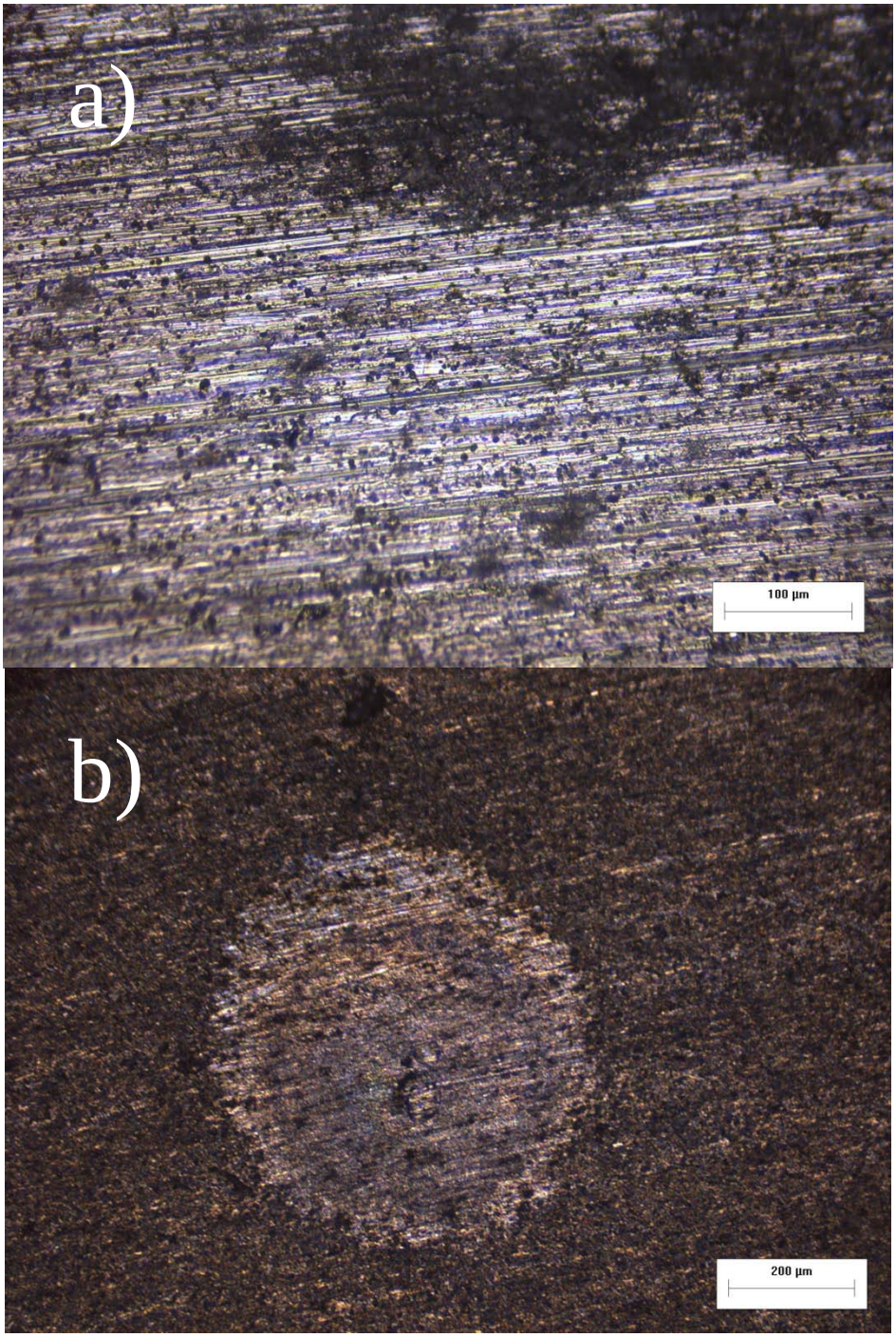

Figure 4-11. Micrographs of the MMCs and monolithic alloy after immersion for 10 hours in aerated 3.5% NaCl solution showing the overall corrosion morphology at low magnification.

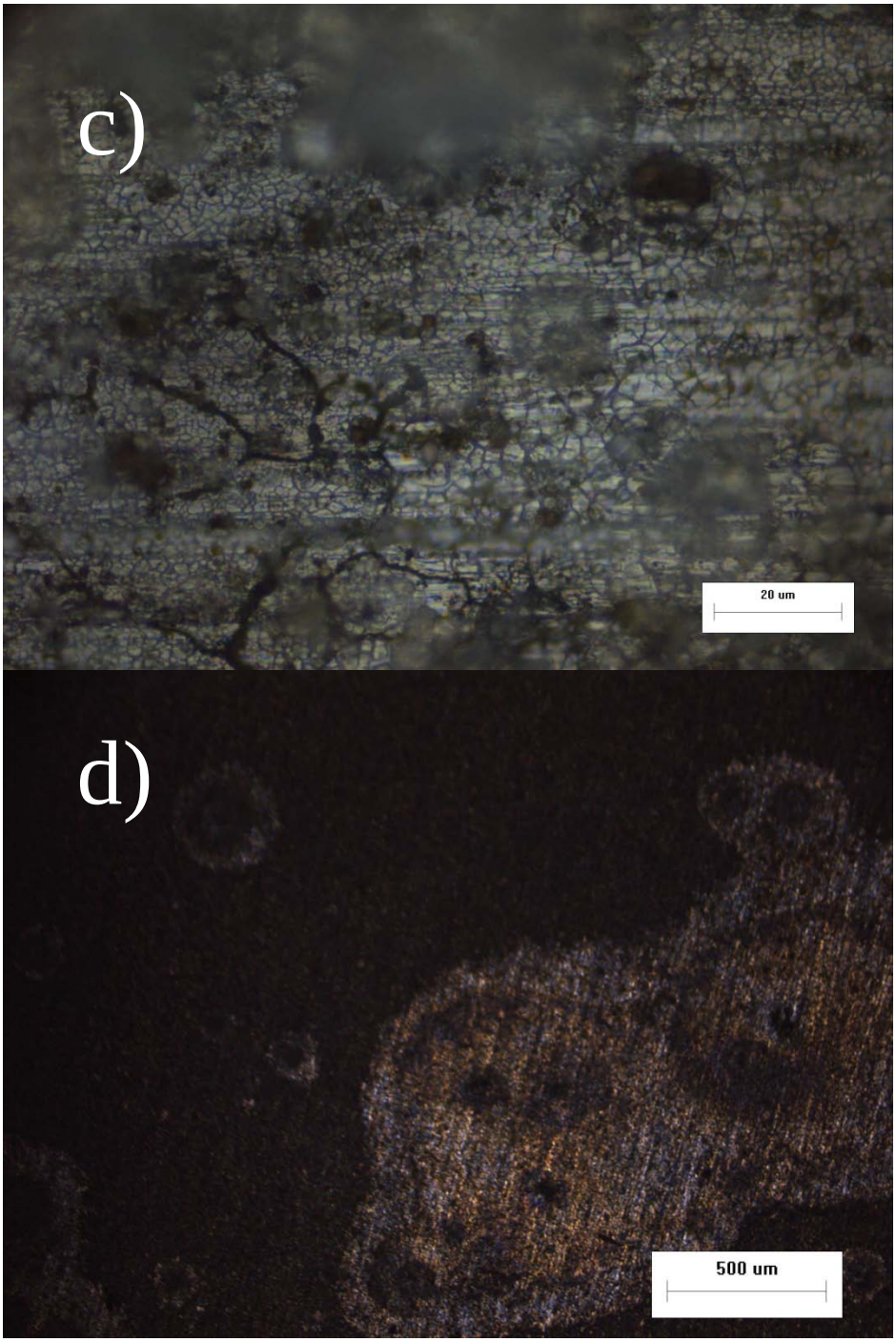

Figure 4-12. (Continued). Micrographs of the MMCs and monolithic alloy after immersion for 10 hours in aerated 3.5% NaCl solution showing the overall corrosion morphology at low magnification.

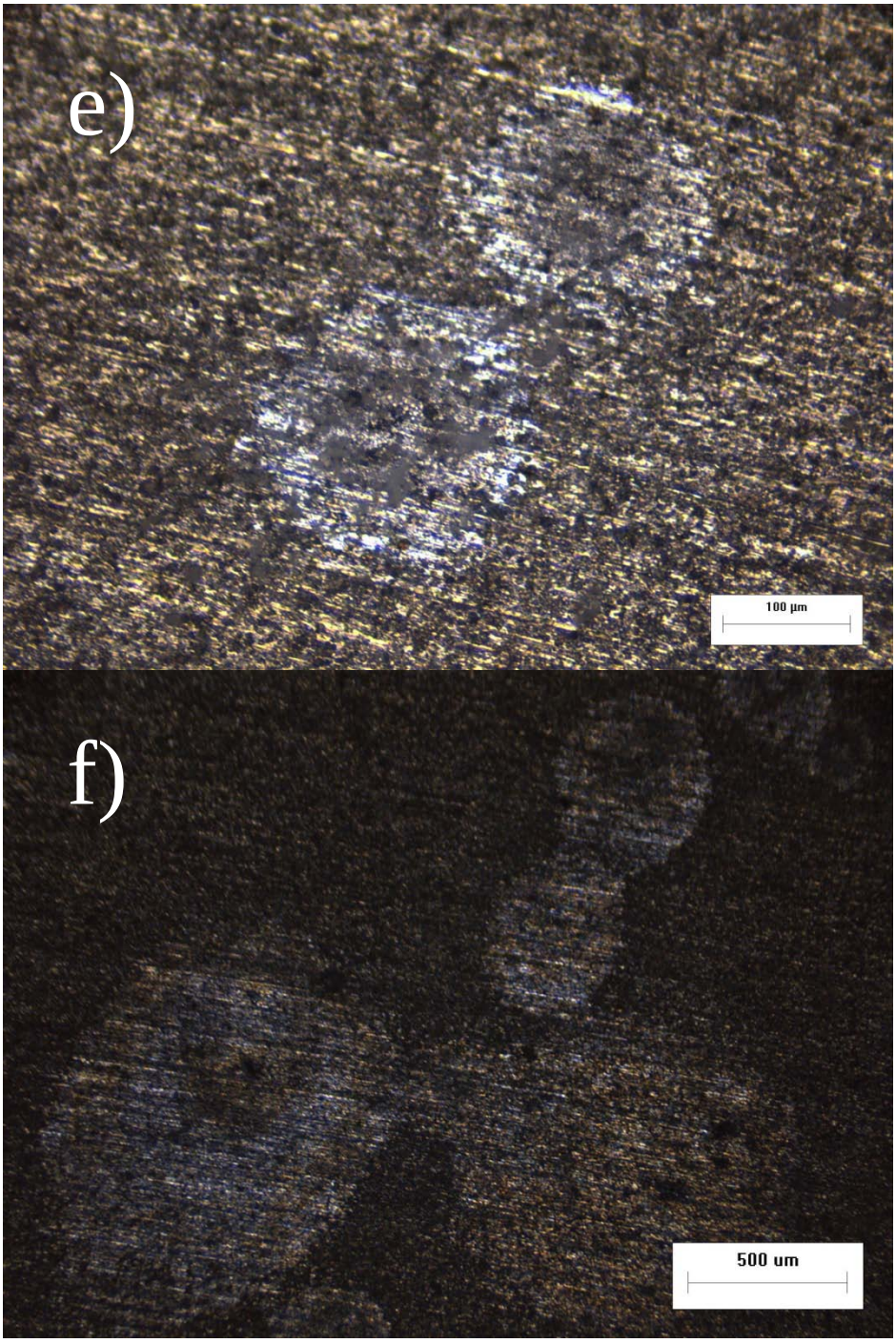

Figure 4-13. (Continued). Micrographs of the MMCs and monolithic alloy after immersion for 10 hours in aerated 3.5% NaCl solution showing the overall corrosion morphology at low magnification.

4.3. Cyclic polarization

Figure 4-14 and Figure 4-15 show the cyclic polarization curves of XT1129 and AA1100, and XT2009, XT2031, XT2048 and AA2024, respectively, in 3.5% NaCl solution. The values of pitting potential, E_p, return potential, E_{rp}, corrosion potential, E_{corr}, corrosion current density, i_{corr}, corrosion rate and Tafel slopes, β_a and β_c are obtained from these figures. R_p was calculated from the Stern-Geary equation (Equation 13):

$$R_p = \frac{\beta_a \beta_c}{i_{corr}[2.303(\beta_a + \beta_c)]}$$

Equation 13

During scanning toward positive potentials in the cyclic polarization experiments, it is usually expected that a stable pit starts growing at E_p where the current increases sharply from the passive current level [74]. However, metal matrix composites and aluminum alloys tested in this study do not show a passive zone. Since a large increase in current corresponding to the transpassive region did not occur, a threshold current density was fixed for reversal of the scan direction. The threshold current density is typically 1 mA/cm^2 [75], based on experiments of anodic polarization of electrodeposited 99.99% aluminum which revealed an increasing current density that reaches a limiting value of approximately 3 mA/cm^2 [16]. After several preliminary tests, the value of threshold current density for cyclic polarization was set at a value of 2 mA/cm^2; when the scan reaches this user-programmed current density value, it reverses and begins scanning in a negative (cathodic) direction.

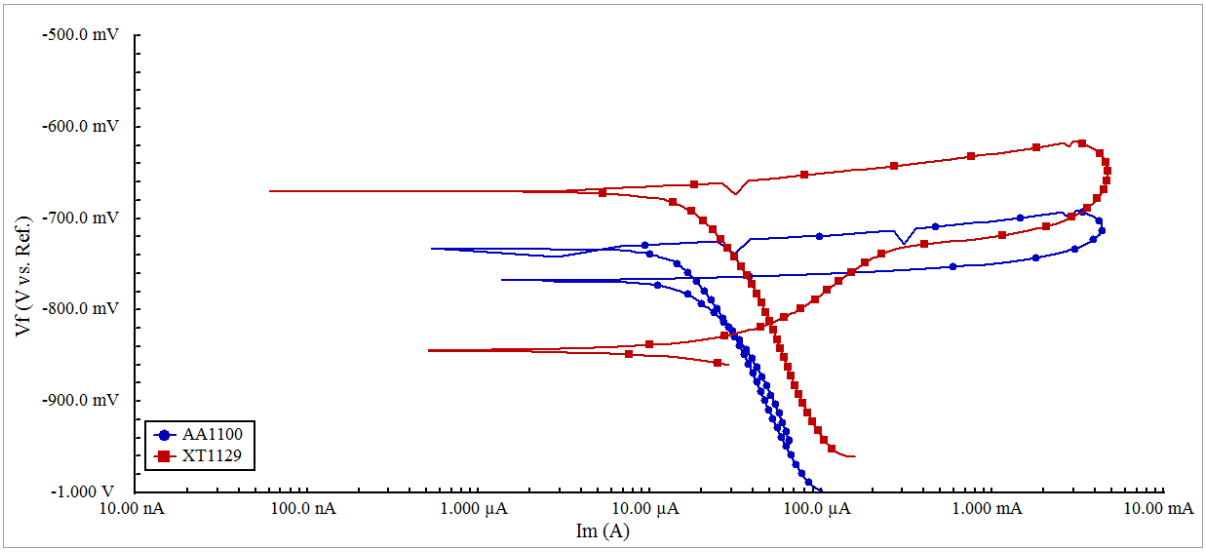

Figure 4-14. Cyclic polarization curves of the aluminum metal matrix composites reinforced with 10 vol.% Al_2O_3 and AA1100.

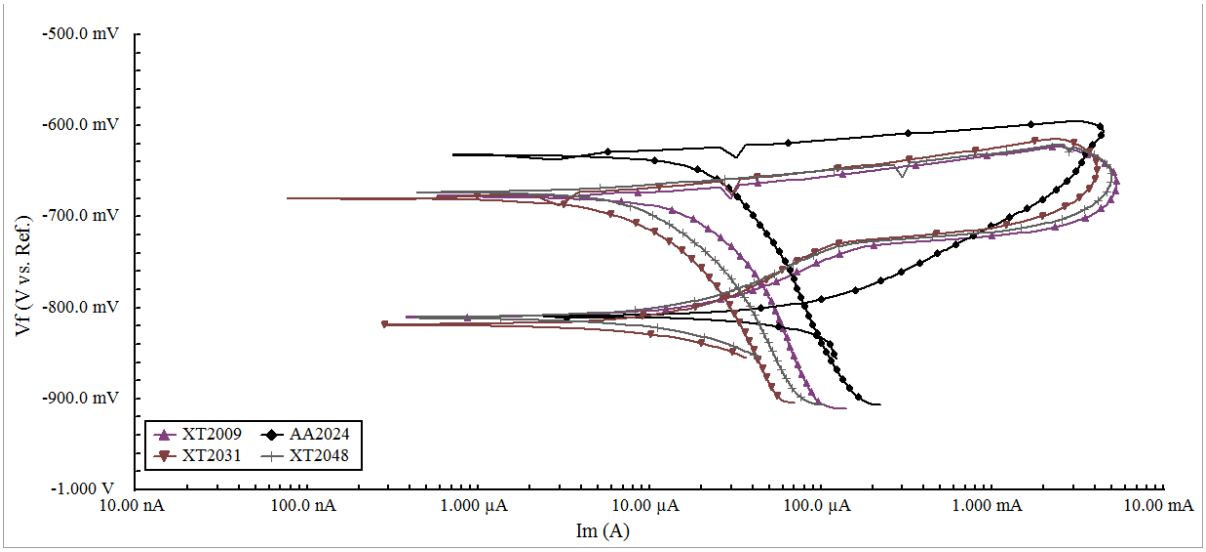

Figure 4-15. Cyclic polarization curves of the aluminum metal matrix composites reinforced with 15, 20 and 25 vol.% Al_2O_3 respectively and AA2024.

The difference between E_p and E_{rp} indicates the susceptibility to localized corrosion of all the materials used in this study. MMCs in particularly did not exhibit any resistance to pitting

corrosion in 3.5 % NaCl solution. From Figure 4-14 and Figure 4-15 it is observed that the corrosion potential is between the pitting potential and the repassivation of the pits for all MMCs, and one can deduce that the tendency toward nucleation and growth of the pit on these MMC surfaces is large or occurs spontaneously [33].

From the potential/current density curves (Figure 4-14 and Figure 4-15), it can be deduced that the MMCs and aluminum alloy studied exhibit similar behavior in 3.5% NaCl solution, although the corrosion mechanism could be different.

The corrosion parameters derived from cyclic polarization analysis are given in Table 4-6.

Table 4-6. Average values of characteristic corrosion parameters of composites and monolithic alloys in aerated 3.5% NaCl solution.

Material	AA1100	XT1129	AA2024	XT2009	XT2048	XT2031
Pitting potential (E_p) (mV)	-719.2	-648.7	-612.6	-651.5	-652.5	-649.0
Return Potential (E_{rt}) (mV)	-763.3	-822.0	-785.8	-775.5	-768.9	-787.0
Open Circuit Potential (E_{OCP}) (mV)	-748.0	-711.1	-655.2	-711.3	-707.7	-706.7
Corrosion potential (E_{corr}) (mV)	-733.7	-670.0	-630.0	-675.3	-676.0	-678.7
Corrosion density (i_{corr}) ($\mu A/cm^2$)	14.1	6.05	10.1	14.7	6.02	3.54
β_a (V/decade)	0.0154	0.0171	0.0169	0.0264	0.0194	0.0215
β_c (V/decade)	0.506	0.0584	0.0978	0.243	0.114	0.0837
Corrosion Rate (mm/year)	0.153	0.066	0.114	0.162	0.064	0.036
R_p (Ω)	461.69	952.83	657.71	729.11	1218.46	2138.62

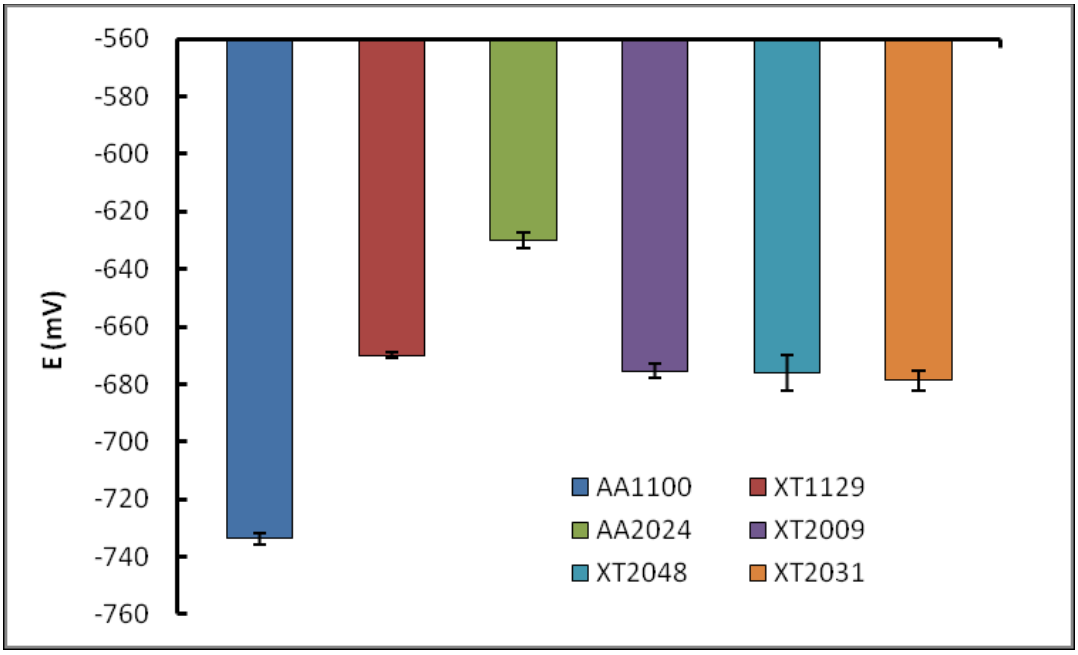

Figure 4-16. E_{corr} values for MMCs XT1129, XT2009, XT2031 and XT2048; and AA1100 and AA2024.

The bar graph in Figure 4-16, shows the experimental values, of corrosion potential, which indicates that in agreement with the open circuit potentials, the corrosion potentials are also similar for all the MMCs in 3.5 % NaCl solutions (approx. E_{corr}=-675mV), with a variation of a few millivolts. The potential is noblest for AA2024 (E_{corr}=-630 mV), and the most active is AA1100 (E_{corr}=-733mV).

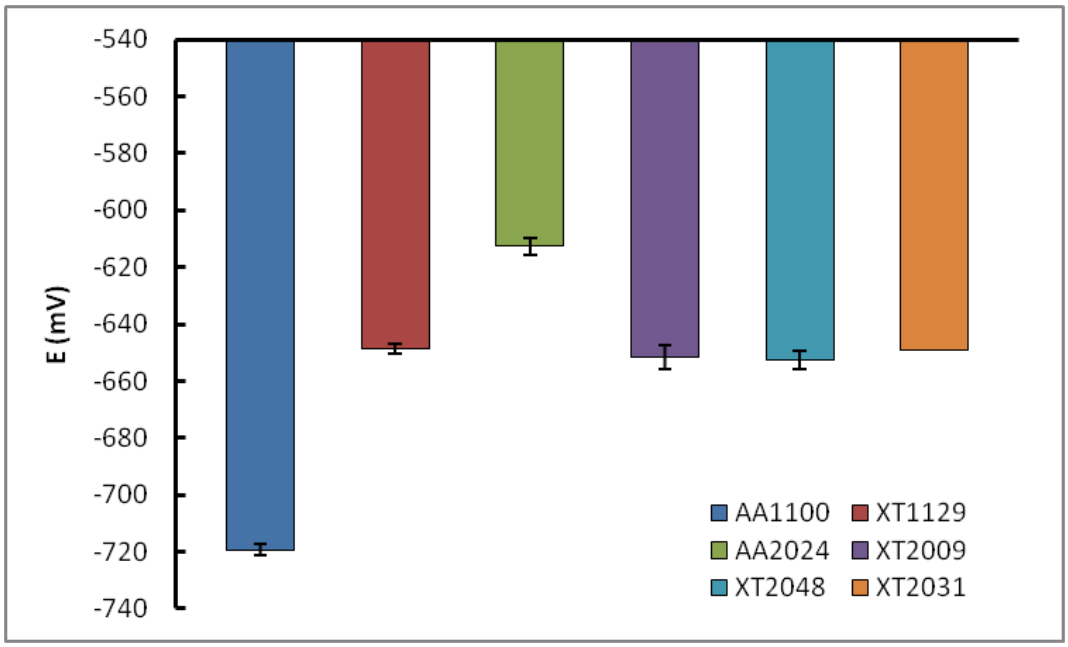

Figure 4-17. Pitting potentials E_p for MMCs XT1129, XT2009, XT2031 and XT2048; and AA1100 and AA2024.

The pitting potentials, shown in Figure 4-17 are also similar in all the MMCs (approx. E_p= -650mV), with variation of about one millivolt. The AA2024 exhibited the most positive E_p (E_p=-612mV), indicating relatively higher pitting corrosion resistance of this alloy in chloride solution compared to alloy AA1100 (E_p= -719mV).

The E_{corr} for the AA1100 has been observed to have a more active potential due to its pure composition with respect to both MMCs and AA2024 and because the AA2024 alloy has more active alloying elements in the matrix (i.e. Cu). When the alloy AA2024 is exposed to NaCl solution the intermetallic precipitate (i.e. Al_2Cu) is initially more active than the matrix, which is the cause of the subsequent cathodic behavior [15,76]. The corrosion potentials of

MMCs are found to lie between the corrosion potentials of AA1100 and AA2024, because reinforcement particles lead to the formation of precipitates of finer intermetallic Al_2Cu which are homogeneously distributed in the composite [77].

The morphology of corroded surfaces after polarization was examined by optical microscopy. The results showed that the surfaces were severely pitted after polarization testing in 3.5% NaCl solution.

Figure 4-18 shows that in both monolithic alloys AA1100, AA2024 as well as the MMCs, the pits were distributed evenly across the surface.

Figure 4-18-a shows the distribution of pits on alloy AA1100 exhibiting uniform initiation all over the surface. This is due to the intermetallic particles that precipitated in the process of production, whose typical constituents were analyzed to be (Al, Fe) and (Al, Fe, Si) [27]. The Al_3Fe particles are known to be cathodic to aluminum matrix [42].

Figure 4-19-c shows the even distribution of pits on the surface of AA2024, although the number of pits is more than on AA1100. This is due to the fact that the number of alloying elements, Cu (greater than 4%), Mn, Mg, Si, is greater in this case than for AA1100 (see Table 3-1). These elements produce precipitates such as Al2Cu (θ) and Al2CuMg (S) [78]. Thus, after immersion in NaCl, localized corrosion takes place, due to a cathodic reaction that takes place at these intermetallic compounds, as a result of which the aluminum surrounding these intermetallic precipitates dissolves [14].

Figure 4-18-b, Figure 4-19-d, Figure 4-20-e and f show surfaces of the MMCs after cyclic polarization testing. The distribution of pits is again even overall, although these are larger and deeper, than those in AA1100 and AA2024. As in the samples subjected to open circuit

potential measurements, halos were also observed. XT1129 presents the greatest number of pits followed by XT2009, XT2031 and XT2048.

In all composites studied here, it was observed that the nucleation of pits occurred uniformly. However, only a few of these grow (Figure 4-18), while the surrounding pits stop growing. If the Cu in the intermetallic compound Al(Cu,Mg) is the principal component responsible for the low resistance of the alloy to localized corrosion [69,78,79], then the rate of nucleation of pits should be greater in the MMCs XT1129, XT2009, XT2031 and XT2048 because the intermetallic Al_2Cu is homogeneously distributed in the matrix, as shown in Figure 4-1.

Protection potential (the first intersection point of the forward scan with the reverse scan during cyclic polarization) in every case is more electronegative than the respective corrosion potential, meaning that pitting corrosion does occur in the all materials tested and begins spontaneously as soon as immersion in the solution takes place [77].

It is clear that the onset of pitting is not visible in the forward scan, which means that E_p is very close to E_{corr}. E_p is not easily observed in aerated solutions, which is the case in most of the aluminum alloys [77]. It can be observed that pitting potential is not affected significantly by the addition of the Al_2O_3 reinforcement in MMCs [28,33], but rather by the alloying elements in aluminum matrix.

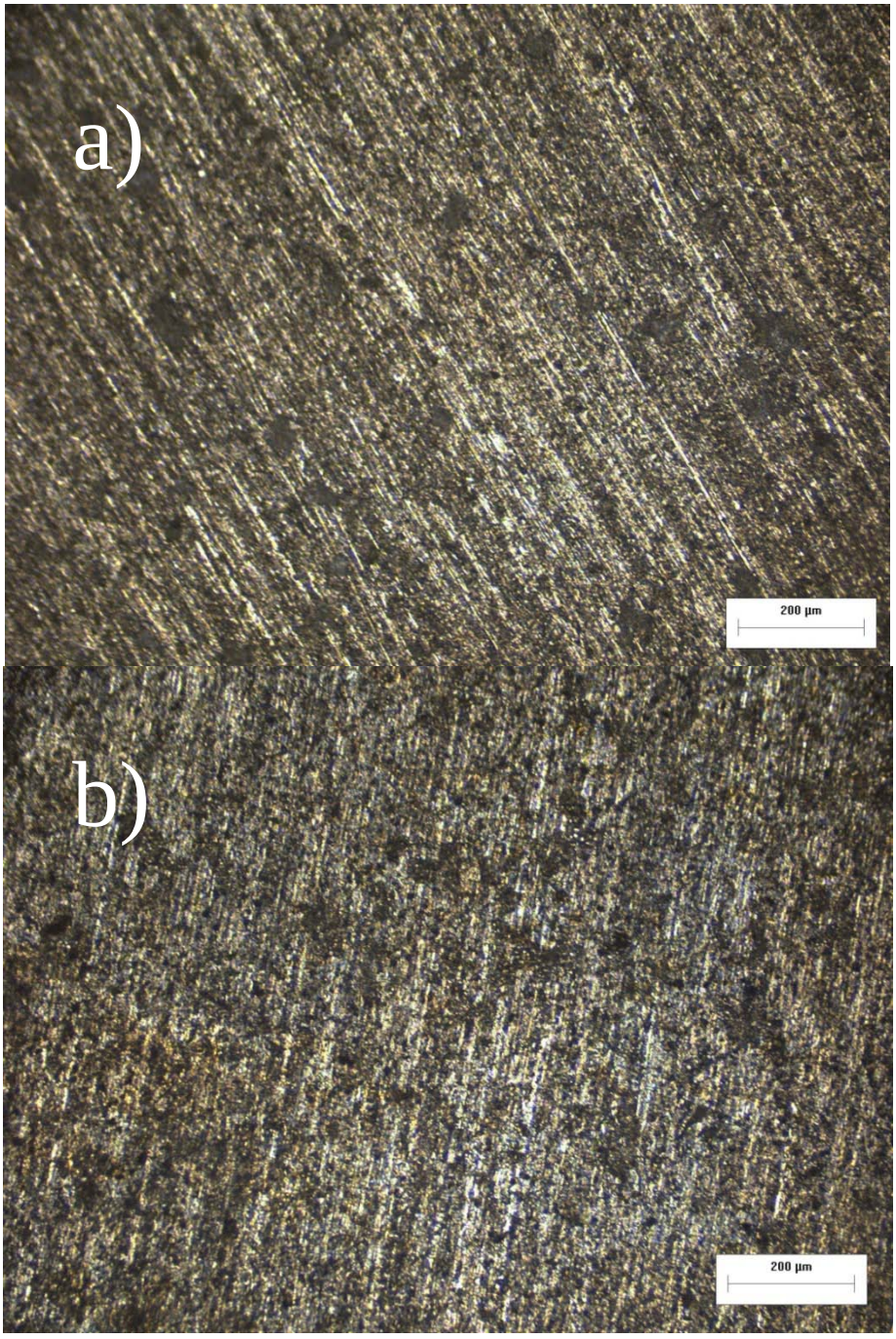

Figure 4-18. Corrosion surfaces following potentiodynamic cyclic polarization in aerated 3.5% NaCl solution for composites and aluminum alloy showing the overall pitting morphology at low magnification.

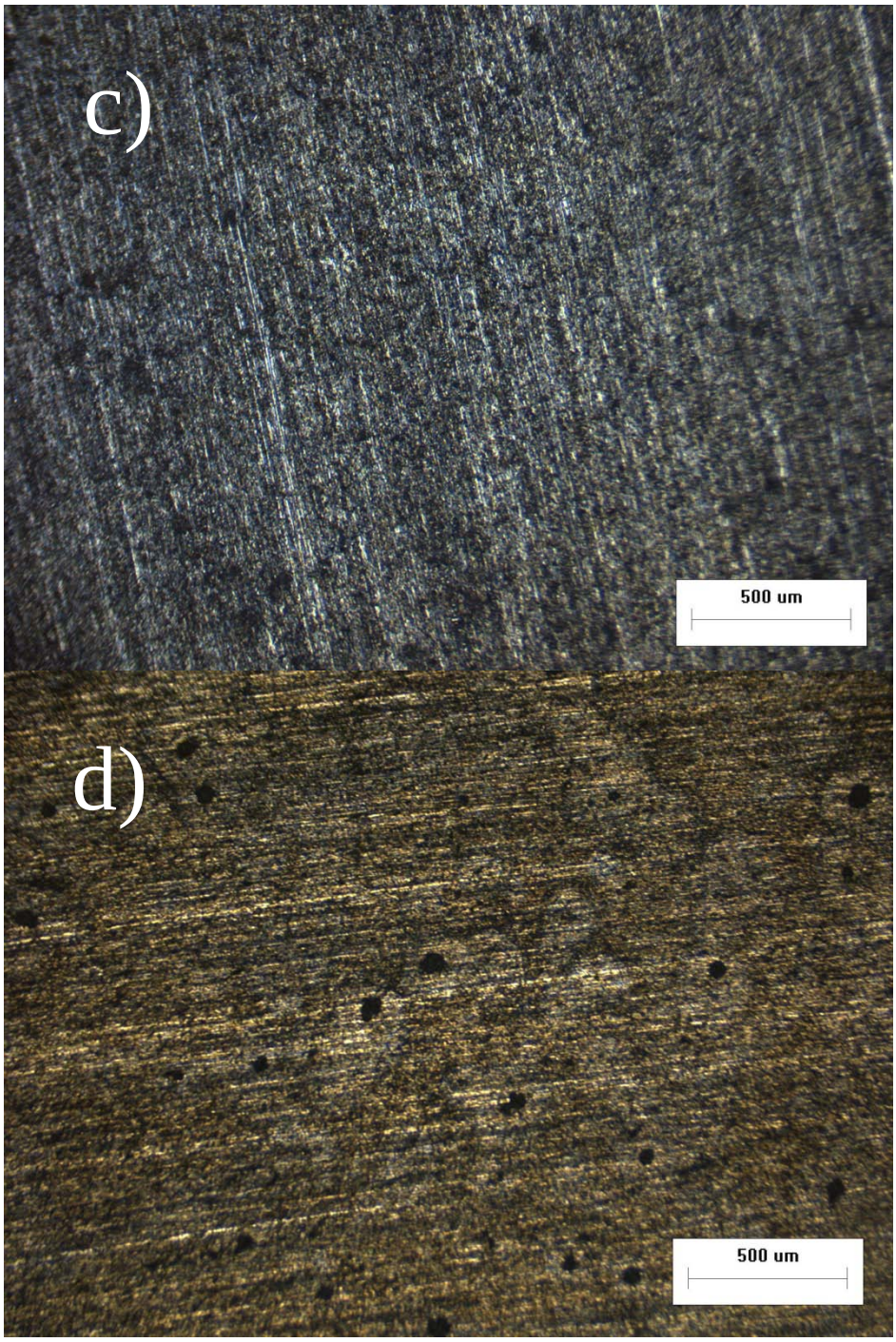

Figure 4-19. (Continued). Corrosion surfaces following potentiodynamic cyclic polarization in aerated 3.5% NaCl solution for composites and aluminum alloy showing the overall pitting morphology at low magnification..

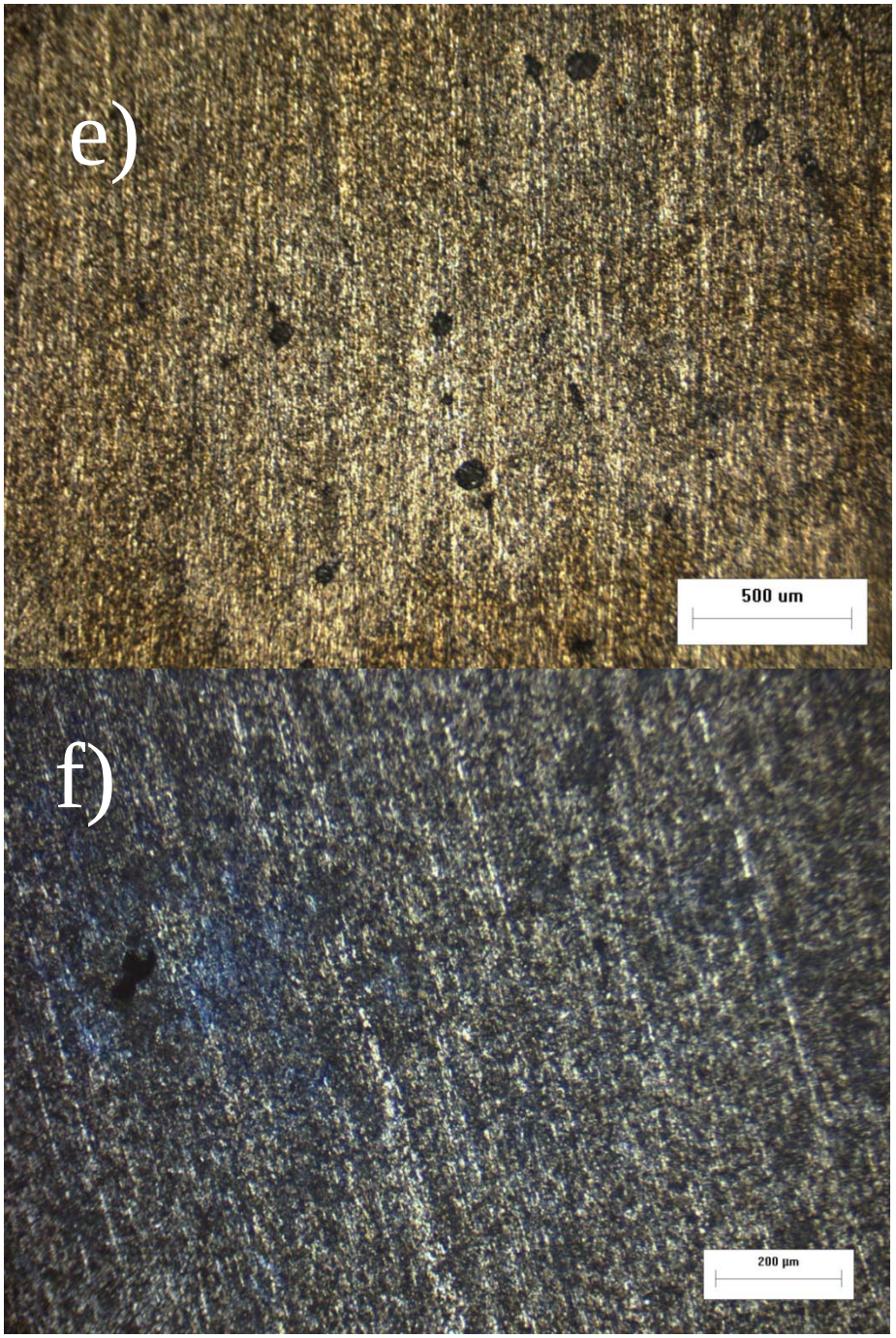

Figure 4-20. (Continued). Corrosion surfaces following potentiodynamic cyclic polarization in aerated 3.5% NaCl solution for composites and aluminum alloy showing the overall pitting morphology at low magnification.

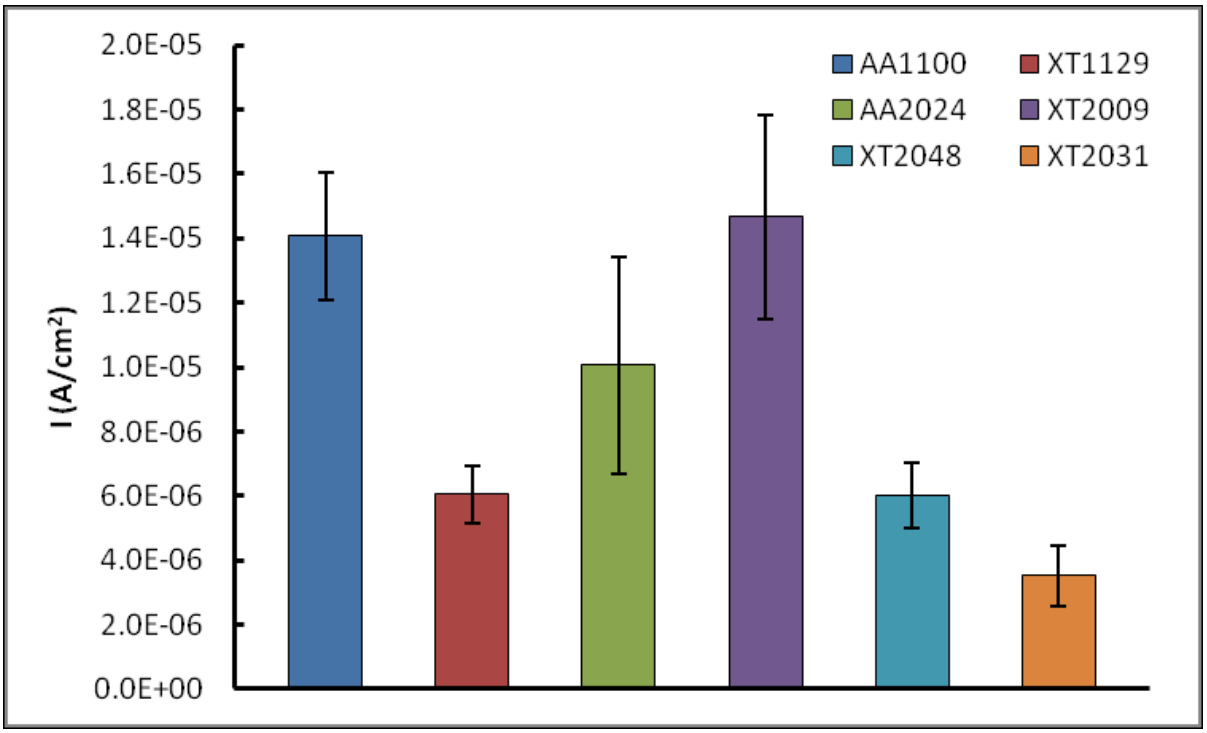

Figure 4-21. Corrosion current densities (i_{corr}) for MMCs XT1129, XT2009, XT2031 and XT2048 as well as AA1100 and AA2024.

The corrosion rate, i_{corr}, obtained from the polarization curves are presented in Table 4-6 and Figure 4-21. Corrosion attack was observed to be relatively uniform for the AA1100, AA2024 and XT1129. The surface oxide film in the composites is not continuous due to presence of porosities and it appears that the particulate-matrix interfaces influence the corrosion rate [23,35]. Therefore corrosion initiates easily at these discontinuities and the composites are susceptible to severe localized corrosion [68]. Although the extent of localized corrosion may not be reflected in the i_{corr} values determined using Tafel extrapolation studies [22,74], this technique, nevertheless, provides information that the

corrosion rate of composites increases or decreases with increasing volume fraction of reinforcement.

Table 4-7. Average values of pit parameters produced during cyclic polarization tests. XT2048 and XT 2031 show bimodal pit characteristics.

Materials	Average density of pits (pits/mm^2)	Average area fraction of pits	Average size of pits (μm)
AA1100	1293.86	7.1E-05	30.00
XT1129	1096.49	8.16E-05	12.33
AA2024	818.71	9.48E-05	22.33
XT2009	1578.95	9.08E-05	15.00
XT2048	1242.69	8.17E-05	12.00
XT2031	1250.00	8.95E-05	11.67
XT2048 *	966.18	2.25E-05	73.33
XT2031 *	805.15	1.89E-05	70.00

Table 4-7 shows the values obtained from measurements of the pits produced during the cyclic polarization test. Measurements were made according to ASTM G46. The composites XT2048 and XT2031 had a bimodal distribution of the average pit size, which were 12 μm and 70 μm. Data from of the large size pits are highlighted with an asterisk in Table 4-7. It can also be seen that the size of the pits in the MMCs are approximately the same (12μm), whereas in the monolithic alloys the pits are twice as large as those in the MMCs.

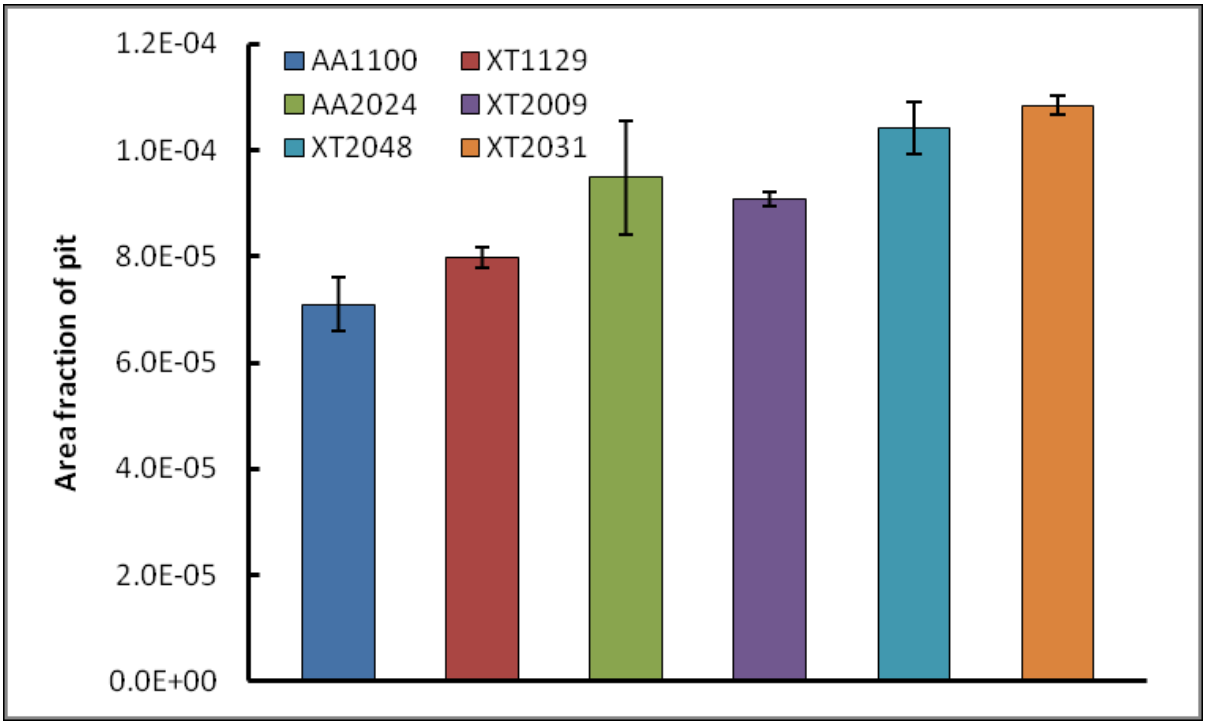

Figure 4-22. Average values of area fraction of pits after cyclic polarization testing of MMCs and monolithic alloys.

The total area fraction of pits of the composites XT2048 and XT2031 are the sum of the area fraction of pits of varying sizes found in these composites. Area fraction of pits is shown in Figure 4-22. As expected, it can be seen that the area fraction of pits increases as the volume fraction of reinforcement in the metal matrix increases.

From Figure 4-21 it can be inferred that for the XT2xxx series MMCs, the corrosion rates increase with decreasing volume fraction of reinforcement. Also, XT2031 (25% Al_2O_3) exhibits the lowest value of corrosion rate (i_{corr}= 3.54 µA/cm^2), which is approximately four times smaller than that for XT2009 (15% Al_2O_3), as well as for AA1100 alloy, and 2.5 times that of the AA2024 alloy. MMCs XT1129 and XT2048 have the same corrosion rate i_{corr}= 6 µA/cm^2.

Based on the data in Table 4-6 and Table 4-7 it can be inferred that the pitting corrosion mechanisms for the MMCs reinforced with alumina particles are affected by increasing the percentage of Al_2O_3 particles added to the matrix, and pit density is so high that the corrosion appears to be generalized.

The corrosion potential did not vary greatly or show a definite trend in relation to the presence of Al_2O_3 particles. However, an increase in the degree of corrosion is attributed to the presence of Al_2O_3 particles.

4.4. Electrochemical impedance spectroscopy (EIS)

Figure 4-23 and Figure 4-24 show the Nyquist and Bode plots respectively of electrochemical impedance spectroscopy data recorded at open circuit conditions after a steady state potential was attained in aerated 3.5 % NaCl solution for AA1100 and MMC XT1129. At high frequencies in the Nyquist plot, there is an obvious capacitive arc, which could be considered as double layer capacitance, while at low frequencies inductive processes clearly occur. Clearly, a larger value of polarization resistance can be extrapolated from these plots for the MMC which also shows a greater value of the double layer capacitance. The phase angles in the Bode plots indicate a slightly more capacitive behavior of the MMC which can be explained due to the presence of the Al_2O_3 reinforcement.

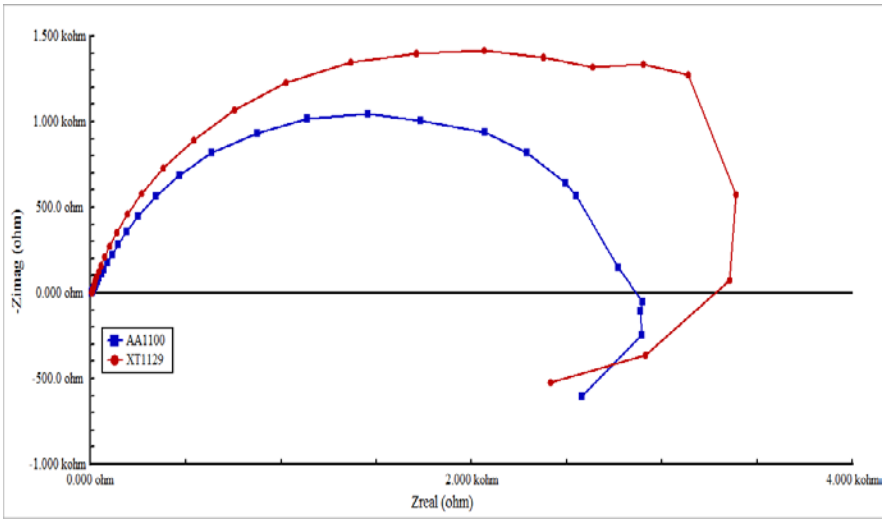

Figure 4-23. Nyquist plot for the aluminum MMCs reinforced with 10 vol.% Al_2O_3 (XT1129) and alloy AA1100 immersed in 3.5% NaCl solution.

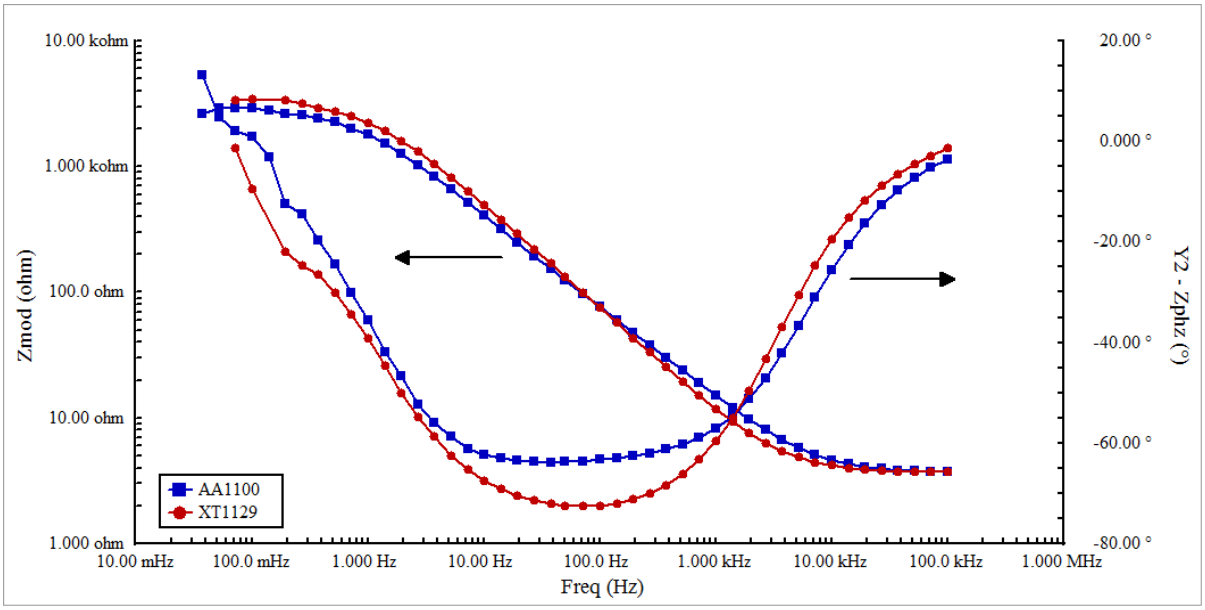

Figure 4-24. Bode impedance magnitude and phase angle plots for the MMCs reinforced with 10% Al_2O_3 (XT1129) and alloy AA1100 immersed in 3.5% NaCl solution.

The measured capacitive impedance data were analyzed based upon the Randles equivalent circuit presented in the Figure 4-27. The circuit includes a solution resistance (R_{soln}), charge transference (R_{ct}) or polarization resistance (R_p) of the surface oxide film, and constant phase element (CPE). In the 3.5% NaCl electrolytic media, specific adsorption of different ions on the oxide film and possible formation of different products, lead to the dissolution of the outer porous film as well as an increase in the heterogeneity of the surface. All of these factors lead to the presence of a single layer and results in the introduction of a CPE term in place of the normally used capacitance in the EC models shown in Figure 4-27 and Figure 4-28.

Figure 4-24 and Figure 4-25 show the EIS results for AA2024 and MMC XT2009, XT2048 and XT2031, where, at high frequencies there is an obvious capacitive arc, which could be considered again also as double layer capacitance, and at low frequencies the impedance processes of inductive character occurs clearly for MMCs XT2009 and XT2048. For XT2031 however, two consecutive capacitive semicircles are produced in the Nyquist plot. On the other hand, AA2024 shows a single semicircle with dispersion of data in the mid frequency range. As in the earlier cases, the resistance polarization values appear to increase with increasing volume percentage of the reinforcement. Nevertheless, AA 2024 which lacks reinforcement has the highest resistance polarization. A similar trend is seen in terms of capacitive behavior and can be explained as a result of the presence of the reinforcement as well as the susceptibility to pitting attack of these materials.

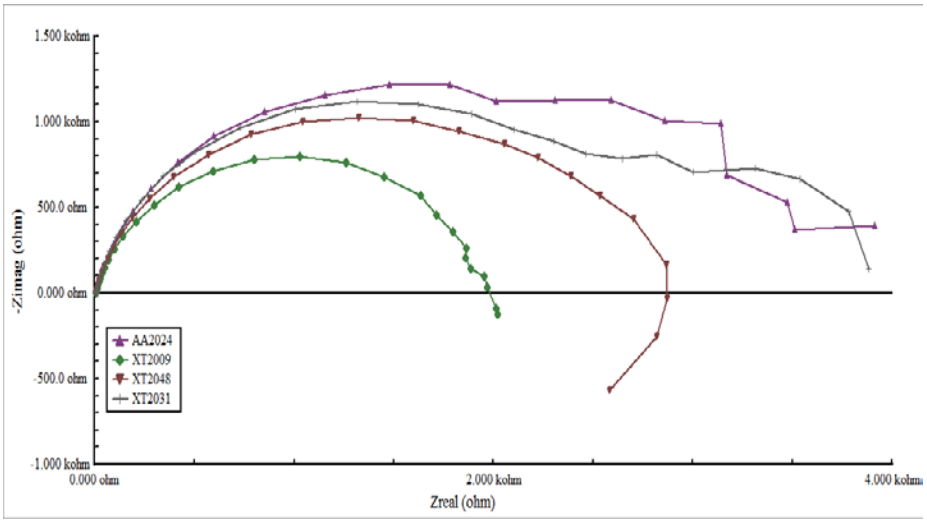

Figure 4-25. Nyquist plots for the aluminum MMCs reinforced with 15% Al_2O_3 (XT2009), 20% Al_2O_3 (XT2048), 25% Al_2O_3 (XT2031) and alloy AA2024 immersed in 3.5% NaCl solution.

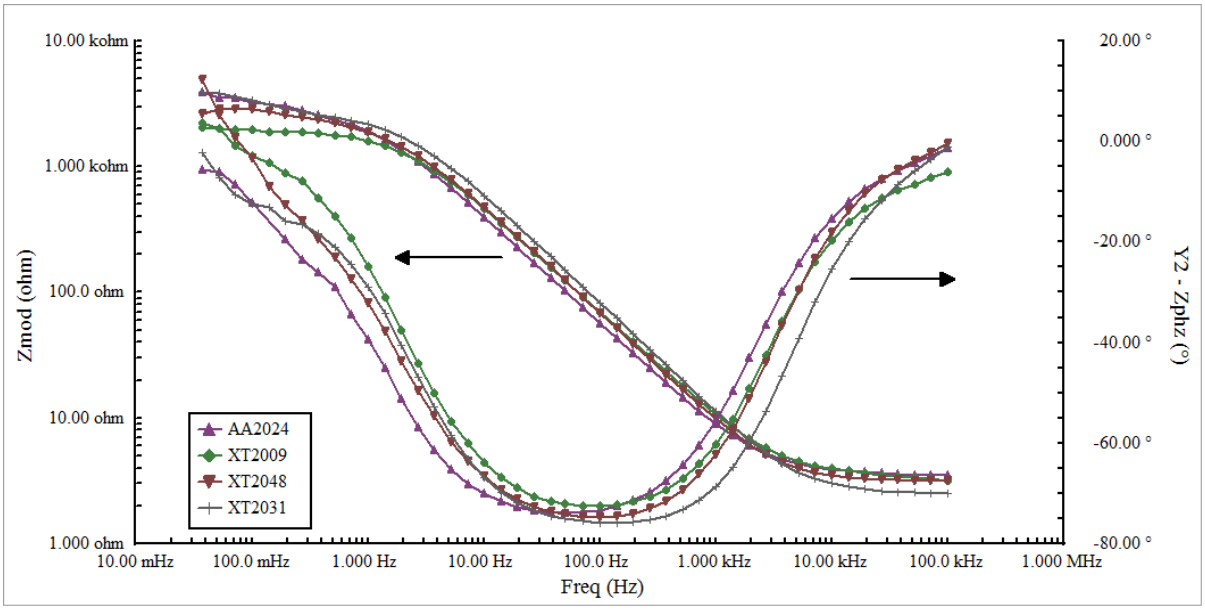

Figure 4-26. Bode impedance magnitude and phase angle plots for the MMCs reinforced with 15% Al_2O_3 (XT2009), 20% Al_2O_3 (XT2048), 25% Al_2O_3 (XT2031) and alloy AA2024 immersed in 3.5% NaCl solution.

The Randles equivalent circuit presented in the Figure 4-27 simulates the experimental data obtained for AA1100, XT1129, AA2024, XT2009 and XT2048 immersed in aerated 3.5%NaCl solution, while the Randles equivalent circuit presented in the Figure 4-28 is for XT2031. Here R_{soln} is uncompensated resistance between working and reference electrode, C_{dl} is constant phase element through passive layer, R_p is passive layer resistance, C_{cor} is constant phase element at substrate/passive layer interface and R_{cor} is charge transfer resistance at substrate/passive layer interface.

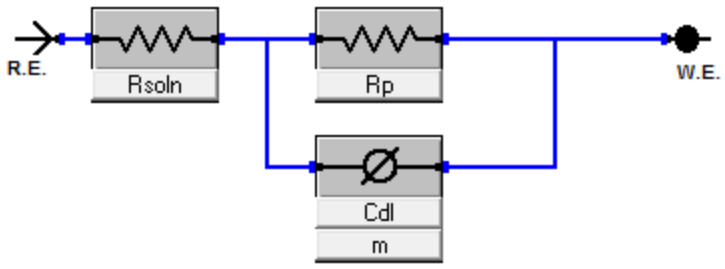

Figure 4-27. Equivalent circuit processed to produce the response for the systems: AA1100, AA2024, XT1129, XT2009 and XT2048 in aerated 3.5 wt.% NaCl solution.

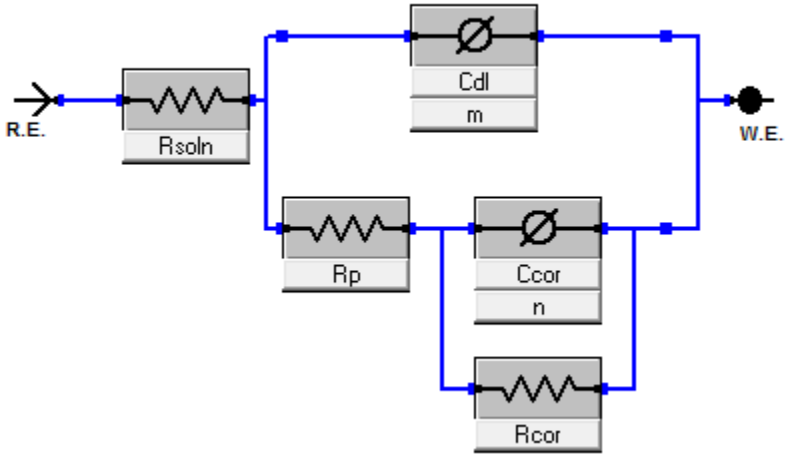

Figure 4-28. Equivalent circuit processed to produce the response for the XT2031 system in aerated 3.5 wt.% NaCl solution.

The results of the analyses using the Randles circuit for all Bode and Nyquist plots are displayed in Table 4-9. The polarization resistance (R_p) obtained by impedance spectroscopy analysis show that the resistance of the AA2024 is larger than that for the composite, indicating that the composite tends to corrode at a higher rate than the matrix.

The morphology of corroded surfaces after EIS test was examined by optical microscopy. The results showed that the surfaces were severely pitted after polarization in 3.5% NaCl

solution. Figure 4-29 shows that both in alloys AA1100, AA2024 and the MMCs, the pits were distributed evenly across the surface. Table 4-8 shows the values obtained from measurements of the pits produced during the EIS test. Here again, measurements were made according to ASTM G46.

Table 4-8. Average values of pit parameters produced during EIS tests.

Materials	Average density of pits (pits/mm^2)	Average area fraction of pit	Average size pits (μm)
AA1100	1929.82	1.76E-05	3.00
XT1129	1016.08	6E-05	13.33
AA2024	1008.77	8.31E-05	11.00
XT2009	1147.66	7.59E-05	10.00
XT2048	1637.43	8.12E-05	10.00
XT2031	1864.04	9.08E-05	12.00

Figure 4-32 shows the relationship of Rp a a function of the area fraction of pits on MMCs and monolithic alloys. In materials with corrosion pitting the value of R_p is dependent on the area fraction of pits [80], i.e., increase or decrease in the area fraction of pits results in increased or decreased R_p, respectively. The proportionality factor for R_p-area fraction of pits is not calculated in this investigation.

As shown in Figure 4-29, all samples suffer pitting corrosion after EIS testing. AA1100 has the smallest fraction of pit area while the XT2031 exhibits the maximum fraction of pit area. If monolithic materials mark the limits, AA1100 minimum and AA2024 maximum (Figure 4-32), the MMCs XT1129, XT2048 and XT2048 are located between these limits. In Table 4-8 it can be noted that pit size for the MMCs is less than the average pit size on AA2024 and

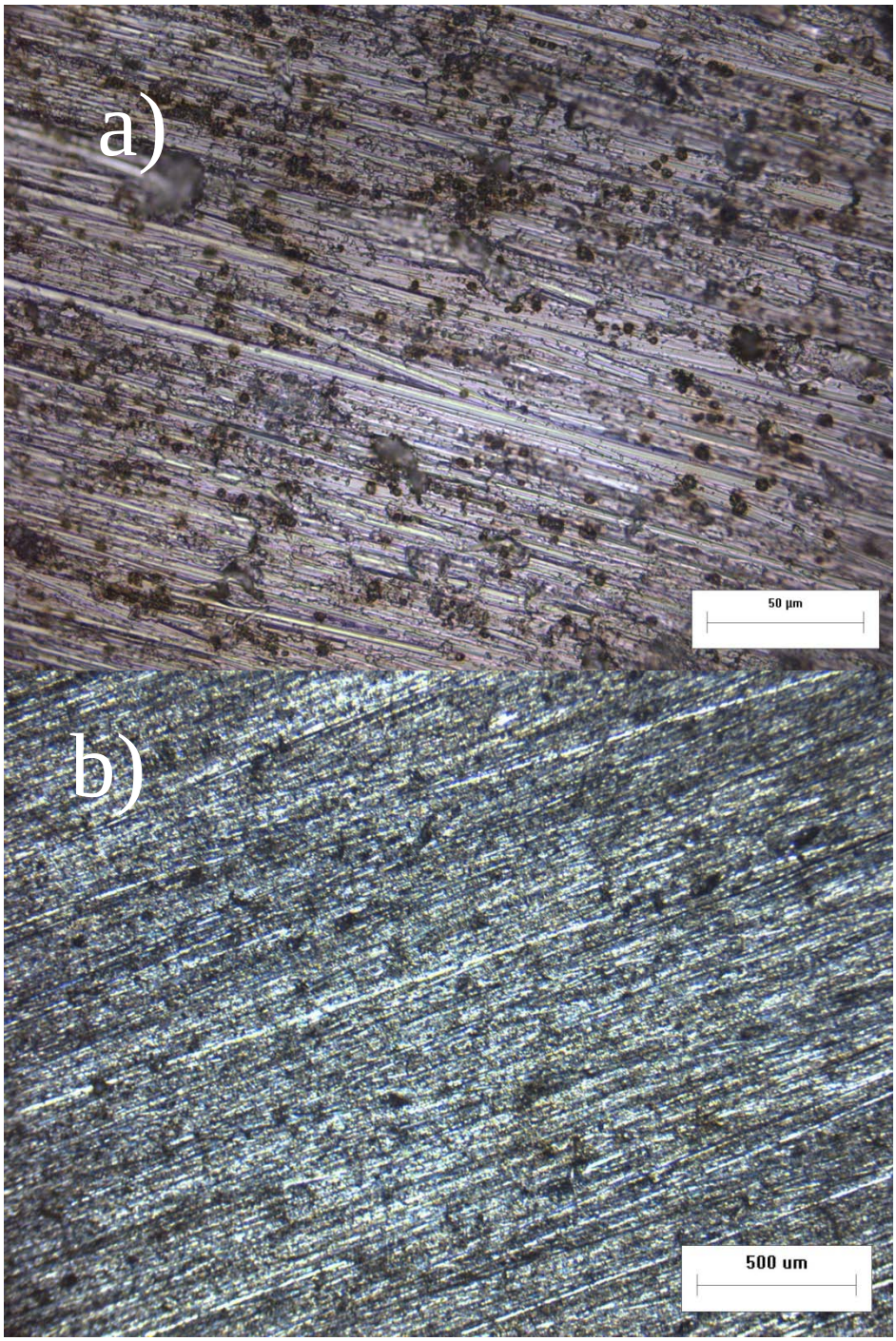

Figure 4-29. Corrosion surfaces following EIS testing in aerated 3.5% NaCl solution for composites and aluminum alloys showing the overall corrosion morphology at low magnification.

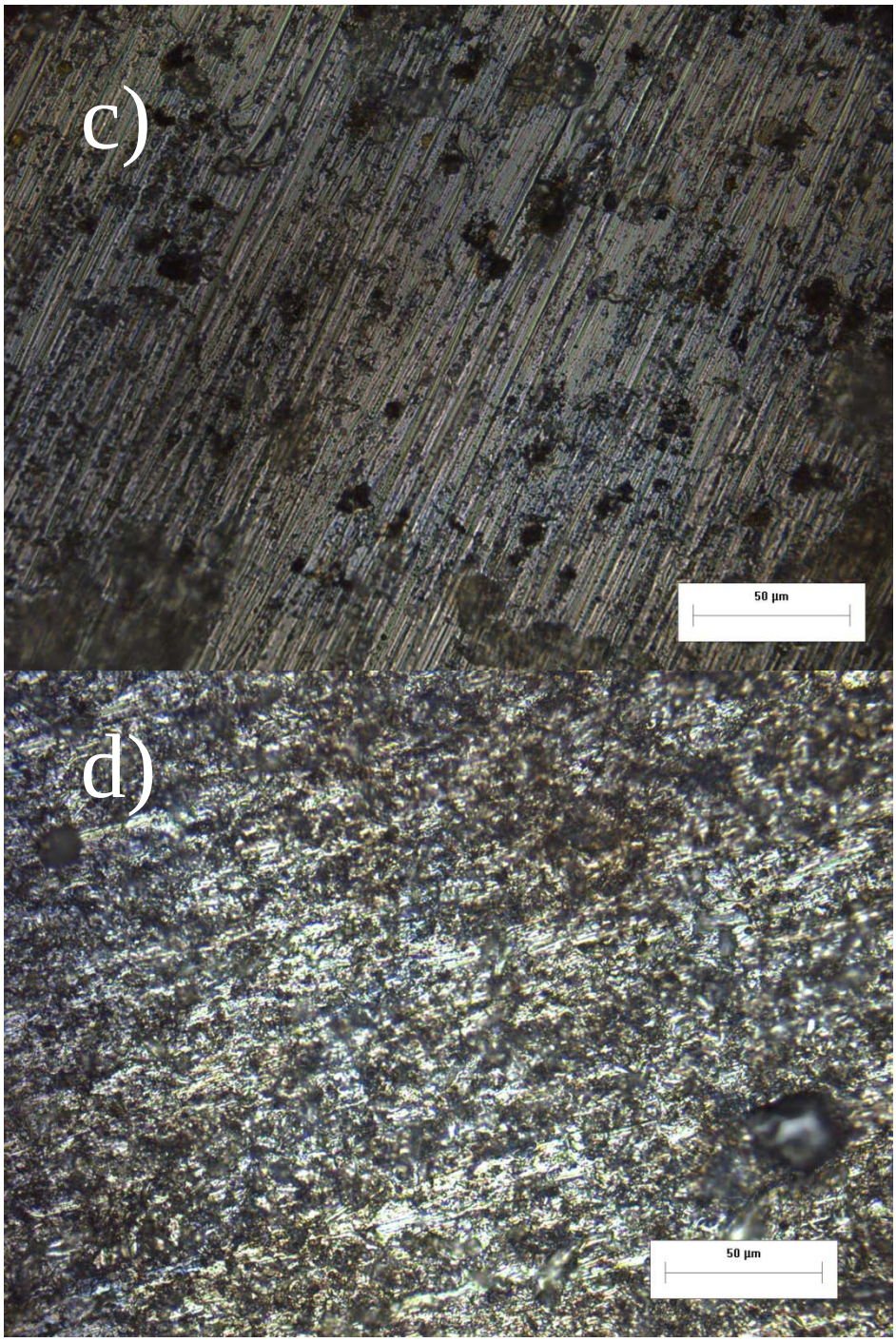

Figure 4-30. (Continued). Corrosion surfaces following EIS testing in aerated 3.5% NaCl solution for composites and aluminum alloys showing the overall corrosion morphology at low magnification.

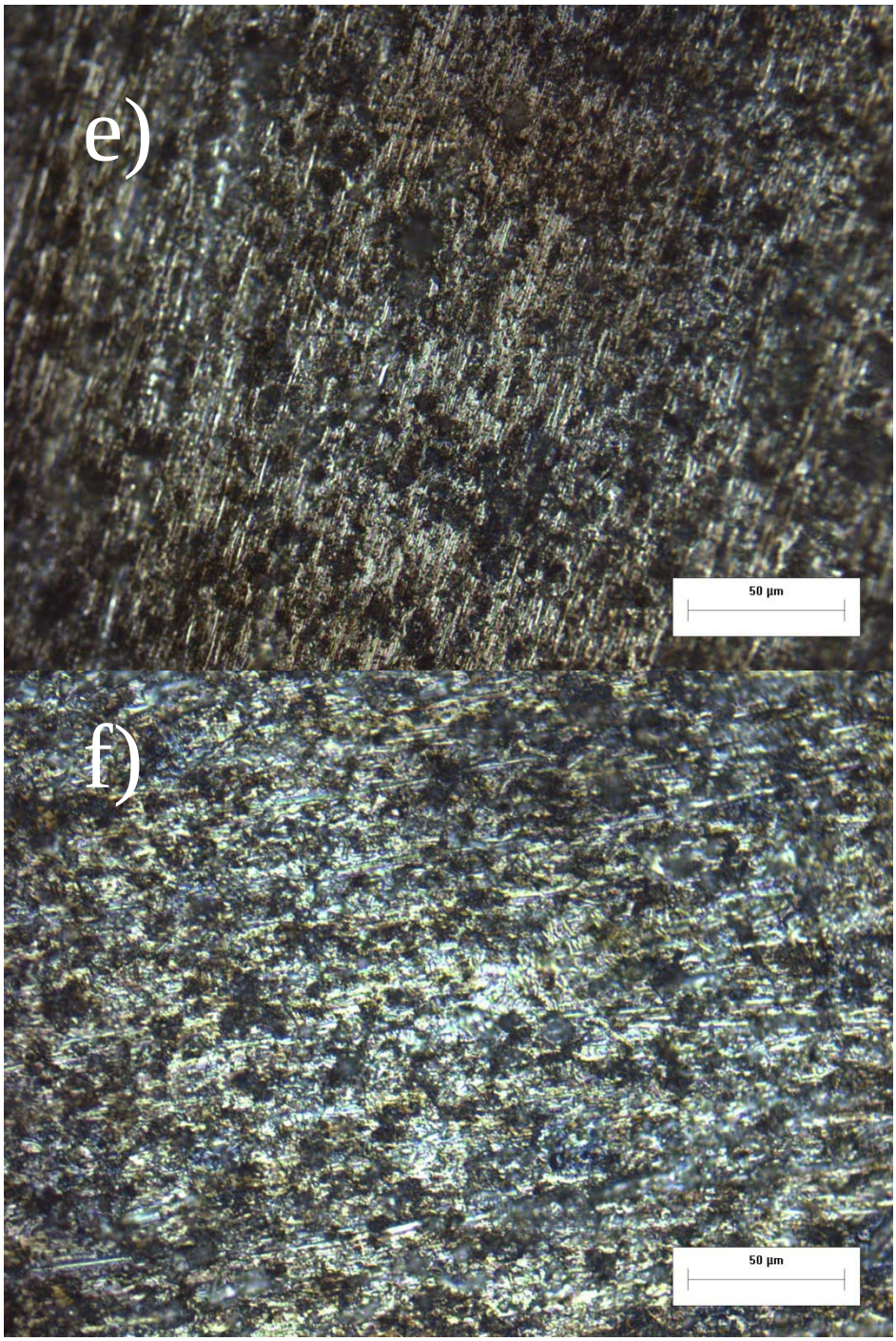

Figure 4-31. (continued). Corrosion surfaces following EIS testing in aerated 3.5% NaCl solution for composites and aluminum alloys showing the overall corrosion morphology at low magnification.

greater than that in AA1100. The density of pits increases with increasing percentage of reinforcement, and it can be stated that the MMCs have many pit nucleation centers although these do not grow to a large extent [81].

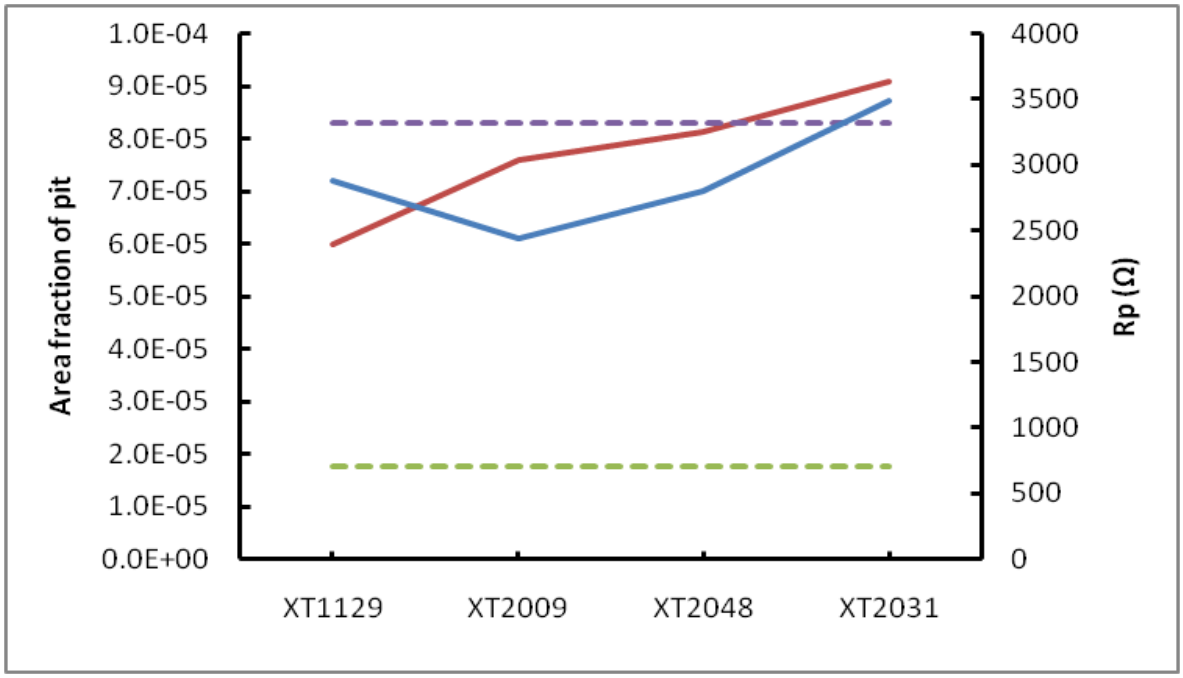

Figure 4-32. Behavior of R_p as a function of area fraction of pits of MMCs and monolithic alloys after EIS testing.

Values of the component parameters for the equivalent circuits in Figure 4-27 and Figure 4-28 were calculated using the DC105 software provided by Gamry Instruments, and the principal values are tabulated in Table 4-9. R_p value for composite XT2031 was calculated from the Nyquist plot at the lowest point which cuts the axis Z' [47]. The impedance parameters from EIS testing indicate similar values of resistance polarization for all the materials which were utilized in this study. The experiment is clearly validated by the fairly

constant values of the solution resistance which indicates that the nature of the solution is not unduly changed during testing. R_p values of the composites are lower than AA2024 and higher than AA1100. In the composites belonging to the XT2XXX series, the R_p increases as the percentage of reinforcement increases. This behavior may be due to the behavior of the intermetallic formed at the interface of matrix and reinforcement [13]. In the presence of Cl^- ions, the semicircle in the Nyquist plot forms an inductive loop which extends into the negative region of the Z" axis indicating specific adsorption of large anions on the surface. There is also the possibility that this may be associated with the anodic process presented by the dissolution of the intermetallics during the initial stages of exposure to the aggressive medium [14]. The presence of an inductive loop may also be related to pitting process [82].

The true capacitance of the data from the plots obtained from EIS testing were calculated from the website of Research Solutions and Resources [83], based on the equation:

$$Z = R_p/[1 + R_p C_{dl}(jw)^m]$$

Equation 14

The values of the time constant (C_{dl}) decreases with increasing percentage of reinforcement, which is attributed to the formation of pits that change the roughness of the surface or produce non-uniformly distributed properties of the irregular electrode surface [47].

Table 4-9. Impedance parameters for aluminum alloys and MMCs in aerated 3.5% NaCl solution.

Material	R_{soln} (ohms)	R_p (ohms)	C_{dl} (S*s^n)	m	C (µF)
AA1100	4.44	2145	8.16E-05	0.821	56.08
XT1129	4.64	2876	6.14E-05	0.846	44.79
AA2024	5.00	3937	6.46E-05	0.846	53.30
XT2009	4.56	2438	5.09E-05	0.858	35.98
XT2048	4.53	2804	4.72E-05	0.860	34.63
XT2031	4.62	3490	4.07E-05	0.869	28.99

5 CONCLUSIONS

All the MMCs (XT1129, XT2009, XT2031 and XT2048) and the monolithic alloys AA1100, AA2024 are subjected to pitting and uniform corrosion, when exposed to 3.5% NaCl solution under open circuit conditions. It may be concluded that the MMCs, although known to be suitable candidates for different structural applications, are highly susceptible to pitting corrosion in saline media. Resistance polarization does increase with increasing volume fraction of the Al_2O_3 reinforcement. The results obtained demonstrate that the intermetallic present in both the aluminum alloys and MMCs are responsible for the observed pitting behavior. While the Al_2O_3 reinforcement as such may have no direct influence on the corrosion behavior of these composite materials, formation of intermetallics at the reinforcement/matrix interface appears to play a significant role. The Al(Cu,Mg) intermetallic initially exhibits an anodic behavior with respect to matrix while the dissolved Cu shows cathodic behavior. The process of reduction of oxygen to OH^- takes place as the cathodic response and the resulting local pH causes the dissolution of the layer of oxide and of neighboring aluminum.

The results show that the reactions occurring in the passive layer and the diffusion phenomenon through this layer are determining factors in EIS studies for aluminum alloys and MMCs. Although the pitting corrosion initiates on cathodic intermetallic particles, reaction slows down when the electrical connection is restricted between intermetallic particles and solution. This can be accomplished by accumulation of corrosion products inside the pits or detachment of intermetallic particles from the alloy surface.

Tafel extrapolation analysis indicates that addition of Al_2O_3 in various amounts (10, 15, 20 and 25 vol. %) has no influence on the corrosion potential, but rather on the rate of corrosion. Corrosion rate decreases with increasing percentage ofAl_2O_3 particles.

Cyclic polarization testing indicates that both the composite materials and the monolithic alloys are not passivated in 3.5 % NaCl solution.

Overall, the results presented here point to significant complexity in the dissolution characteristic of microstructurally heterogeneous Al-Cu-based alloys with Al_2O_3 reinforcement. These complexities must be understood and accounted for to properly control and predict the corrosion behavior of these metal matrix composite materials.

REFERENCES

1. United States of America. Department of Defense; Composite Materials Handbook: Vol. 4. Metal Matrix Composite. United States of America 1999.
2. S. Tjong, Carbon Nanotube Reinforced Composite, WILEY-VCH, Weinheim, 2009, ISBN: 978-3-527-40892-4.
3. K. Kainer (ed.), Metal Matrix Composites: custom-made materials for automotive and aerospace engineering, WILEY-VCH, Weinheim, 2006, ISBN: 3-527-31360-5, ISBN-10: 3-527-31360-0.
4. R. Baboian (ed.), Corrosion Test and Standards: Applications and Interpretation, 2nd Edition, West Conshohocken PA: ASTM International, 2005, ISBN: 0-8031-2098-2.
5. T. Durai, K. Das, S. Das. Corrosion characterization of alumina-magnesium metal matrix composites. *Corrosion Science* 49 (2008) 1110-1130.
6. S. Mileiko, Metal And Ceramic Based Composites: Composites materials series, Vol. 12, Elsevier, Amsterdam, 2007.
7. H. Grene, Evaluation of corrosion protection methods for aluminum metal matrix composites, Ph.D. Dissertation, University of Southern California, USA, 1992.
8. D. Talbot, J. Talbot, Corrosion science and technology, CRC Press, Boca Raton, 1998, ISBN: 0-8493-8224-6.
9. Y. Kim, Characterization of alloying Cu effect on electrochemical reactions of Al-Cu solid solution alloys, Ph.D. Dissertation, The Ohio State University, 2006.
10. T. Suter, Y. Müller, P. Schmutz, O. Trzebiatowski, Microelectrochemical studies of pit initiation on high purity and ultra high purity aluminum. Advanced Engineering Materials 7 (2005) 5 (339-348).
11. S. Minhua, F. Yan, H. Ronggang, L. Changjian, A study of pitting corrosion of aluminum alloy 2024-T3 by scanning microreference electrode technique, Materials Science and Engineering A344 (2003) 323-327.
12. D. Feron (ed.), Corrosion behavior and protection of copper and aluminium alloy in seawater, European Federation of Corrosion Publications, No. 50; Woodhead Publishing Limited, Cambridge England; 2007, ISN:1354-5116.
13. K. Jafarzadeh, T. Shahrabi, M. Hosseini, EIS study on pitting corrosion of AA5083-H321 Aluminum-Magnesium alloy in stagnant 3.5% NaCl solution. Journal of Materials Science and Technology 24 (2008) 215-219.

14. M. Bethencourt, F. Botana, M. Cano, M. Marcos, J. Sánchez-Amaya, L. Gonzáles-Rovira, Behaviour of alloy AA2017 in aqueous of NaCl. Part I: Corrosion mechanisms, Corrosion Science 51 (2009) 518-524.
15. Z. Weilong, G. Frankel, Anisotropy of localized corrosion in AA 2024-T3, Electrochemical and solid-state letters, 3 (2000) 268-270.
16. Y. Liu, M. Arenas, P. Skeldon, G. Thompson, P. Bailey, T. Noakes, H. Habazaki, K. Shimizu, Anodic behaviour of a model second phase: Al-20at.%Mg-20at.%Cu. Corrosion Science 48 (2006) 1225-1248.
17. K. Mazdiyasni (ed.), Fiber reinforced ceramic composites; materials, processing and technology, NOYES PUBLICATIONS, USA, 1990. ISBN: 0-8155-1233-3.
18. S. Peters (ed.), Handbook of composites, 2nd edition, CHAPMAN & HALL, London, 1998.
19. B. Cantor, M. Goringe (eds.), Metal and ceramic matrix composites, Institute of Physics Publishing, Bristol and Philadelphia, 2004.
20. L. Durand (ed.), composite materials research progress, Nova Science Publishers, Inc., New York. 2008.
21. L. Suk-Joog, Sintering: densification, grain growth and microstructure, Elsevier, Amsterdam, 2005.
22. M. Metzger, Intergranular corrosion of single phase aluminium as a pitting phenomenon, Colloque C4, 10 (1975) C4-387.
23. J. Hu, W. Chu, W. Fei, L. Zhao, Effect of interfacial reaction on corrosion behavior of alumina borate whisker reinforced 6061 Al composite, Materials Science and Engineering A374 (2004) 153-159.
24. A. Daoud, W. Reif, Influence of Al_2O_3 particulate on the aging response of A356 Al-based composites, Journal of Materials Processing Technology 123 (2002) 313-318.
25. H. Nakae, S. Wu, Engulfment of Al_2O_3 particles during solidification of aluminum matrix composites, Materials Science and Engineering A252 (1998) 232-238.
26. G. Kiourtsidis, S. Skolianos, E. Pavlidou, A study on pitting behaviour of AA2024/SiC_p composites using the double cycle polarization technique, Corrosion Science 41 (1999) 1185-1203.
27. H. Ezuber, A. El-Houd, F. El-Shawesh, A study on the corrosion behavior of aluminum alloys in seawater, Materials and Design 29 (2008) 801-805.
28. K. Gopinath, R. Balasubramaniam, V.Murthy, Corrosion behavior of cast Al-Al_2O_3 particulate composites, Journal of Materials Science Letters 20 (2001) 793-794.
29. I. Singh, D. Mandal, M. Singh, S. Das, Influence of SiC particles addition on the corrosion behavior of 2014 Al-Cu alloy in 3.5% NaCl solution, Corrosion Science 51 (2009) 234-241.

30. S. Payan, Y. Le-Petitocorps, J. Olive, H. Saadaoui, Experimental procedure to analyze the corrosion mechanisms at the carbon/aluminium interface in composite materials, Composites Part A 32 (2001) 585-589.
31. T. Etter, P. Schulz, M. Weber, J. Metz, M. Wimmler, J. Löffler, P. Uggowitzer, Aluminium carbide formation in interpenetrating graphite/aluminium composites, Materials Science and Engineering A448 (2007) 1-6.
32. A. Pedro, M. Merino, S. Merino, F. Viejo, M. Carboneras, R. Arrabal, Influence of reinforcement proportion and matrix composition on pitting corrosion behavior of cast aluminium matrix composites (A3XX.X/SiC_p). Corrosion Science 47 (2005) 1750-1764.
33. J. De Salazar, A. Ureña, S. Manzanedo, M. Barrena, Corrosion behaviour of AA6061 and AA7005 reinforced with Al_2O_3 particles in aerated 3.5% chloride solutions: potentiodynamic measurements and microstructure evaluation, Corrosion Science 41 (1999) 529-545.
34. A. Griffiths, A. Turnbull, An investigation of the electrochemical polarization behaviour of 6061 aluminium metal matrix composites, Corrosion Science 36 (1994) 23-25.
35. A. Bakkar, V. Neubert, Corrosion characterization of alumina-magnesium metal matrix composite, Corrosion Science 49 (2007) 1110-1130.
36. Making potentiostatic and potentiodynamic anodic polarization measurements, ASTM G5, Eds ASTM International, West Conshohocken, PA 19428-2959 (2004).
37. Conventions applicable to electrochemical measurements in corrosion testing, ASTM G3, Eds ASTM International, West Conshohocken, PA 19428-2959 (2004).
38. Conducting cyclic potentiodynamic polarization measurements for localized corrosion susceptibility of Iron-, Nickel-, or Cobalt-Based alloys, Eds. ASTM International, West Conshohocken, PA 19428-2959 (2004).
39. F. Rodríguez-Gómez, Tecnicas electroquimicas de corriente directa para la medición de la velocidad de corrosión: Resistencia a la polarización, Depto. Ing. Metalúrgica, Facultad Química, UNAM-Mexico D.F. Mexico.
40. R. Kelly, D. Shoesmith, R. Buchheit. Electrochemical techniques in corrosion science and engineering. Marcel Dekker, New York, 2003, ISBN: 0-8247-9917-8.
41. A. Bard, Encyclopedia of Electrochemistry, Vol. 3: Instrumentation and Electroanalytical Chemistry, Wiley VCH, 2007, ISBN: 978-3-527-30395-3.
42. C. Vargel, Corrosion of aluminum, Elsevier Ltd. Amsterdam, 2004, ISBN: 0-08-044495-4.
43. C. Zoski, Handbook of Electrochemistry, Amsterdam, Elsevier B.V., 2007, ISBN-13: 978-0-444-51958-0, ISBN-10: 0-444-51958-0.

44. W. Plieth, Electrochemistry for materials science, Amsterdam, Elsevier B.V.,2008, ISBN: 978-0-444-52792-9.
45. Z. Zhao, G. Frankel, The effect of temper on the first breakdown, Corrosion Science 49 (2007) 3089-3111.
46. V. Bagotshy, Fundamentals of electrochemistry, second edition, Wiley Interscience, New Jersey, 2006, ISBN-13: 978-0-471-70058-6, ISBN-10: 0-471-70058-4.
47. R. Cottis and S. Turgoose, Electrochemical Impedance and Noise, NACE International, Houston, ISBN: 1-57590-093-9.
48. P. Marcus, F. Mansfeld (eds.), Analytical methods in corrosion science and engineering, CRC Taylor & Francis, Boca Raton, 2006, ISBN-13: 978-0-8247-5952-0, ISBN-10: 0-8247-5952-4.
49. A. Brad, L. Faulkner, Electrochemical methods, fundamentals and applications, second edition, John Wiley & Sons, INC. New York, 2001, ISBN: 0-471-04372-9.
50. J. Wang, Analytical electrochemistry, second edition, Wiley-VCH, New York, 2001, ISBN: 0-471-22823-0.
51. E. Barsoukkov, J. Macdonald, Impedance spectroscopy theory, experiment, and applications, Second edition, Wiley-Interscience, New Jersey, 2005, ISBN: 0-471-64749-7.
52. M. Orazem, B. Tribollet, Electrochemical impedance spectroscopy, Wiley, New York, 2008, ISBN: 978-0-470-04140-6.
53. D. Vladikova, The technique of the differential impedance analysis, Part I: Basics of the impedance spectroscopy, Proceedings of the International Workshop “Advanced Techniques for Energy Sources investigation and Testing”, 4-9 Sept. 2004, Sofia Bulgaria.
54. D. Loveday, P. Peterson, B. Rodgers, Evaluation of organic coatings with electrochemical impedance spectroscopy, Part 1: Application of EIS coatings, JCT Coatings Tech, 2004, page 46.
55. V. Jovic, Determination of the correct value of C_{dl} from the impedance results fitted by the commercially available software, Center for Multidisiplinary Studies, University of Belgrade, P.O. Box 33, Serbia and Montenegro.
56. Basis of electrochemical impedance spectroscopy, Gamry Instruments, 734 Louis Drive, Warminster, PA 18974 USA, Website: www.gamry.com.
57. Equivalent circuit modeling using the Gamry EIS300 electrochemical impedance spectroscopy software, Gamry Instruments, 734 Louis Drive Warminster, PA 18974 USA, Website: www.gamry.com.

58. ASM International, Properties and selection: nonferrous alloys and special-purpose materials, Vol. 2, 10th edition, ASM International, Materials Park OH, 1990, ISBN: 0-87170-378-5 (v.2).
59. P. Rodrigo, P. Poza, M. Utrilla, A. Ureña, Identification and [illegible] of Ω phases in AA2009/SiC composites, Journal of Alloys and Compounds 482 (2009) 187-195.
60. T. Ramgopal, P. Gouma, G. Frankel, Role of grain-boundary precipitates and solute-depleted zone on the intergranular corrosion of aluminum alloy 7150, NACE International, Corrosion 58 (2002) 687-697.
61. M. Rodriguez-Reyes, M. Pech-Canul, J. Rendon-Angeles, J. Lopez-Cuevas, Limiting the development of Al_4C_3 to prevent degradation of Al/Si_p, Composites Science and Technology 66 (2005) 1056-1062.
62. C. Hsu-Shen, L. Kuo-Shung, Y. Jien-Wei, Aging behavior and tensile properties of 6061 Al-0.3 μm Al_2O_{3p} particle composite produced by reciprocating extrusion, Scripta Materíalia 45 (2001) 541-546.
63. S. Candan, An investigation on corrosion behavior of pressure infiltrated Al-Mg alloy/SiC_p composites, Corrosion Science 51 (2009) 1392-1398.
64. R. Buchheit, R. Boger, M. Carroll, R. Lear, C. Paglia, J. Searles, The electrochemistry of intermetallic particles and localized corrosion in Al alloys, JOM Journal of the Minerals, Metals and Materials Society 53 (2001) 29-33.
65. L. Guan-Jun, L. Wen-Fang, P. Ji-Hua, D. Jun, Micro-yield behaviors of Al_2O_3-$SiO_{2(sf)}$/Al-Si metal matrix composites, Transactions of Nonferrous Metals Society of China, 17 (2007) 307-312.
66. R. Escalera-Lozano, C. Gutiérrez, M. Pech-Canul, M. Pech-Canul, Corrosion characteristic of hybrid $Al/SiC_p/MgAl_2O_4$ composites fabricated with fly ash and recycled aluminum, Materials Characterization 58 (2007) 953-960.
67. C. Vargel, Corrosion of aluminum, Elsevier, Amsterdam, 2004. ISBN: 0-008-044495-4
68. J. Datta, B. Samanta, A. Jana, S. Sinha, C. Bhattacharya, S. Bandyopadhyay, Role of Cl^- and NO_3^- ions on the corrosion behavior of 20% SiC_p reinforced 6061-Al metal matrix composite: A correlation between electrochemical studies and atomic force microscopy, Corrosion Science 50 (2008) 2658-2668.
69. R. Cervantes, L. Murr, R. Arrowood, Copper nucleation and growth during the corrosion of aluminum alloy 2524 in sodium chloride solutions, Journal of Materials Science 36 (2001) 4079-4088.
70. H. Obispo, L. Murrr, R. Arrowood, E. Trillo, Copper deposition during the corrosion of aluminum alloy 2024 in sodium chloride solutions, Journal of Materials Science 35 (2000) 3479-3495.

71. A. Sehgal, G. Frankel, B. Zoofan, S. Rokhlin, Pit growth study in Al by the foil penetration technique, Journal of the Electrochemical Society 147 (1) (2000)140-148.
72. W. Zhang, G. Frankel, Anisotropy of localized corrosion in AA2024-T3, Electrochemical and Solid-State Letters 3 (2000) 268-270.
73. L. Shreir (ed.), Corrosion Metal/environment reactions, third edition, Butterworth-Heinemann, Oxford, 1994, ISBN: 0-7506-1077-8.
74. G. Frankel, Pitting corrosion of metals, Journal Electrochemical Society 145 (1998) 2186-2196.
75. Princeton Applied Research, Application Note Corr-4, Electrochemistry and corrosion overview and techniques. Website: http://www.princetonappliedresearch.com/products/appnotes.cfm.
76. Y. Kim, R. Buchheit, A characterization of the inhibiting effect of Cu on metastable pitting Al-Cu solid solution alloys, Electrochemical Acta 52 (2007) 2437-2446.
77. G. Kiourtsidis, S. Skolianos, Pitting corrosion of artificially aged T6 AA2024/SiC_p composites in 3.5wt.% NaCl aqueous solutions, Corrosion Science 49 (2007) 2711-2725.
78. R. Buchheit, R. Boger, Cu redistribution and surface enrichment due to dissolution of Al-Cu alloys. The Ohio State University. Fontana Corrosion Center, Department of Materials Science and Engineering, 2002. Final report: Air Force Office of Scientific Research.
79. H. Böhni, Metastable pitting – Occurrence and significance for passive metals, Swiss Federal Institute of Technology Zürich ETH-Hönggerberg, CH 8093 Zürich, Switzerland.
80. W. Neil, C. Garrad, The corrosion behaviour of aluminium-silicon carbide composites in aerated 3.5% sodium chloride, Corrosion Science, 36 (1994) 5 (837-851).
81. S. Candan, Effect of SiC particle size on corrosion behavior of pressure infiltrated Al matrix composites in NaCl solution, Materials Letters 58 (2004) 3601-3605.
82. A. Aballe, M. Bethencourt, F. Botana, M. Marcos, M. Rodríguez, Corrosion monitoring of the AA2024 alloy in NaCl solutions by electrochemical noise measurements, Rev. Metal. Madrid 34 (1998) 42-46.
83. Research Solutions & Resources LLC, Capacitance value from CPE, R parallel, Princeton, NJ 08543-7561 PO Box 7561, Website: http://www.consultrsr.com/ .

APPENDIX A: EDS ANALYSIS

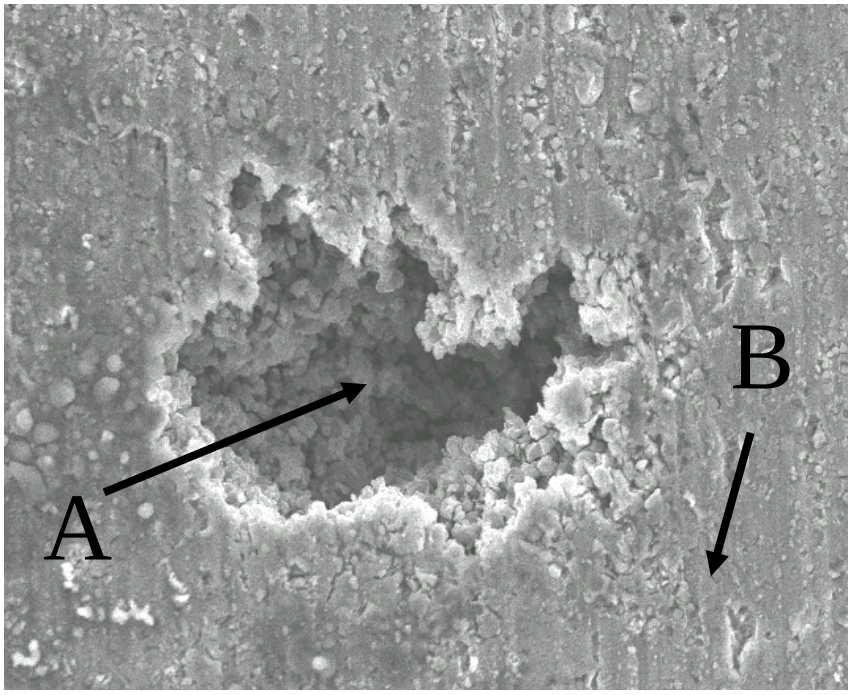

Figure A 1. EDS analysis point of MMC XT 1129 after immersion in 3.5% NaCl solution for 10 h, 1000x.

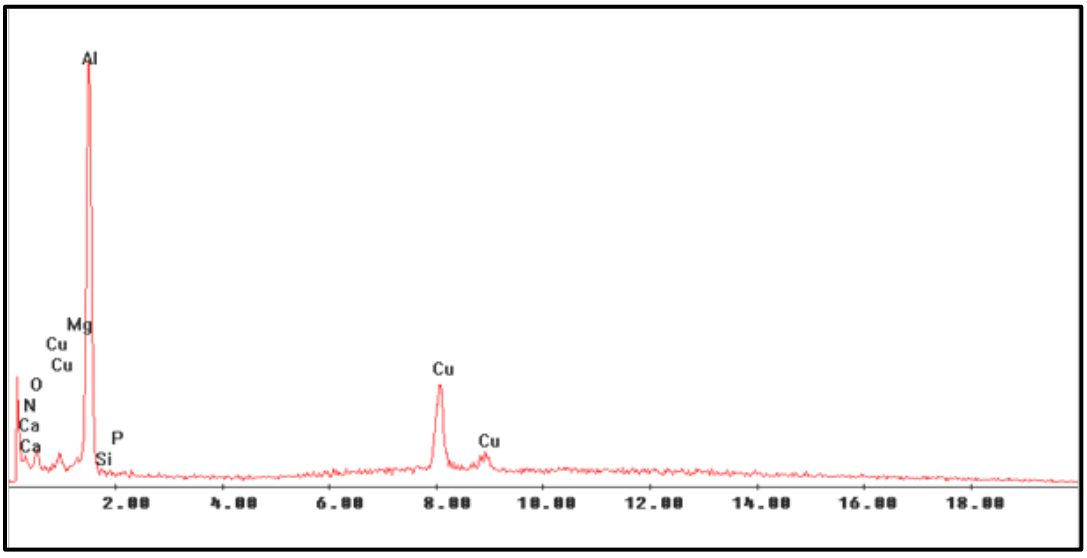

Figure A 2. EDS intensities inside the pit (zone A) of XT1129 after immersion in 3.5% NaCl solution for 10h.

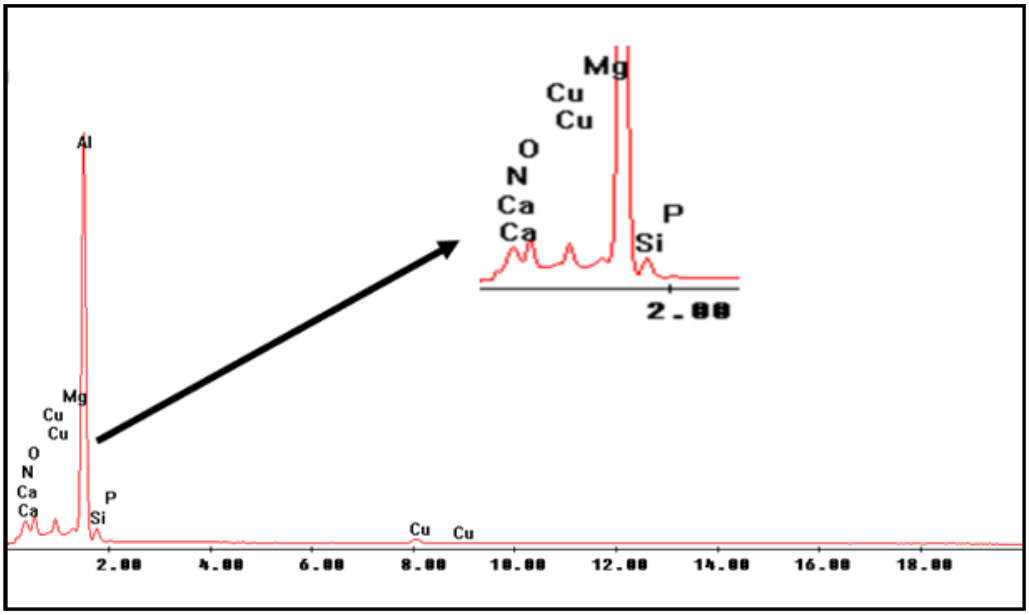

Figure A 3. EDS intensities around the pit (zone B) of MMC XT1129 after immersion in 3.5% NaCl solution for 10h.

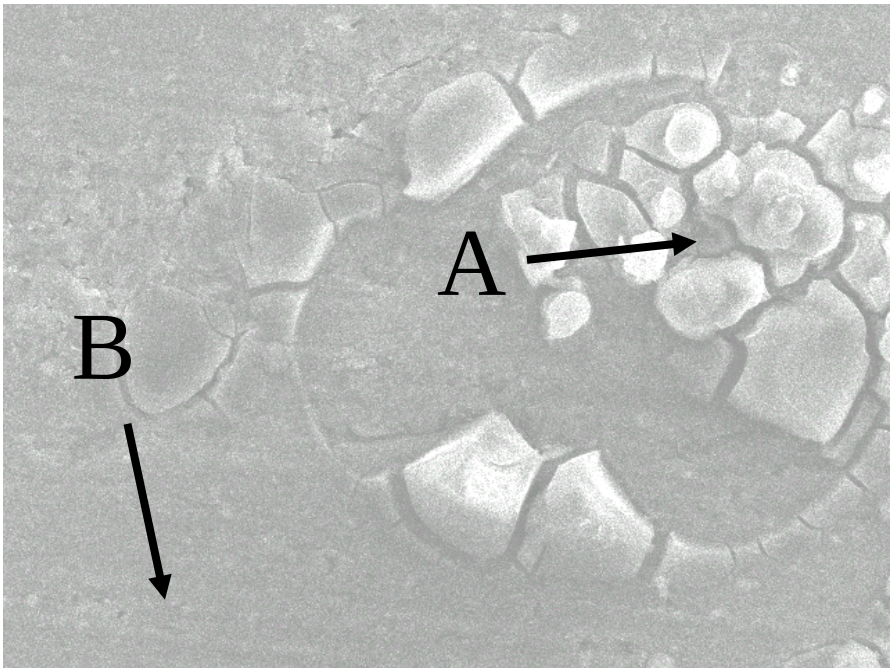

Figure A 4. EDS analysis point of MMCs XT 2009 after immersion in 3.5% NaCl solution for 10 h, 1000x.

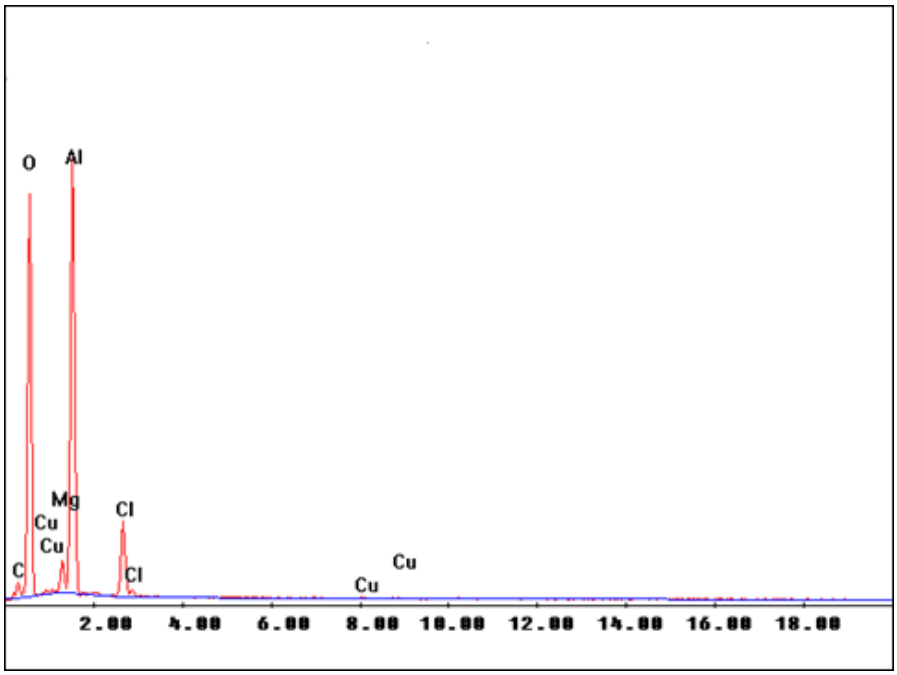

Figure A 5. EDS intensities inside the pit (zone A) of MMC XT2009 after immersion in 3.5% NaCl solution for 10h.

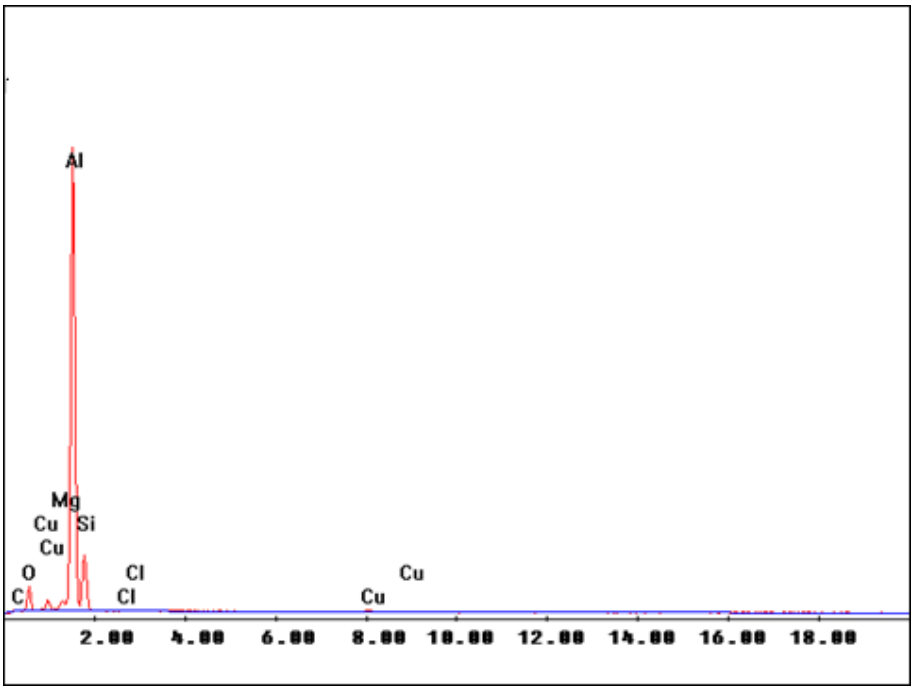

Figure A 6. EDS intensities around the pit (zone B) of MMC XT2009 after immersion in 3.5% NaCl solution for 10h.

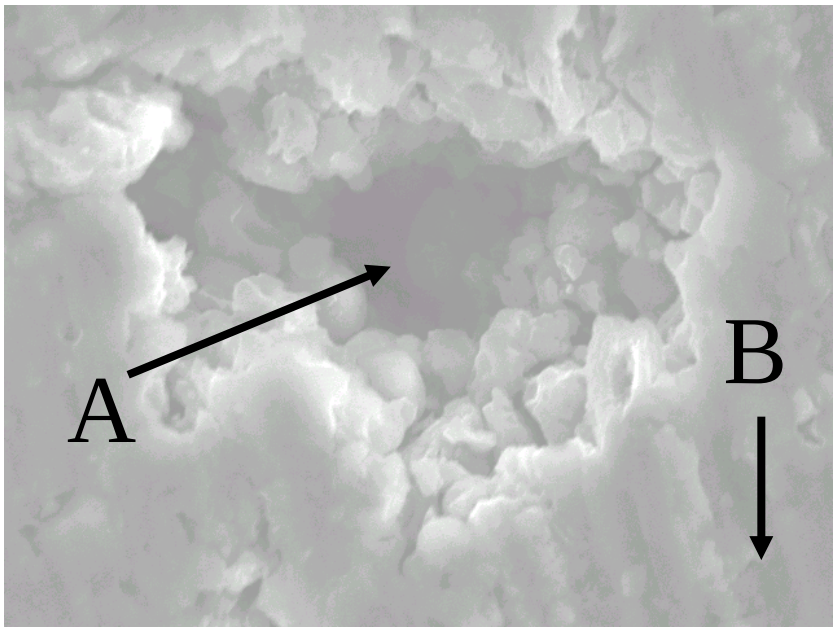

Figure A 7. EDS analysis point of MMC XT 2048 after immersion in 3.5% NaCl solution for 10 h, 3000x.

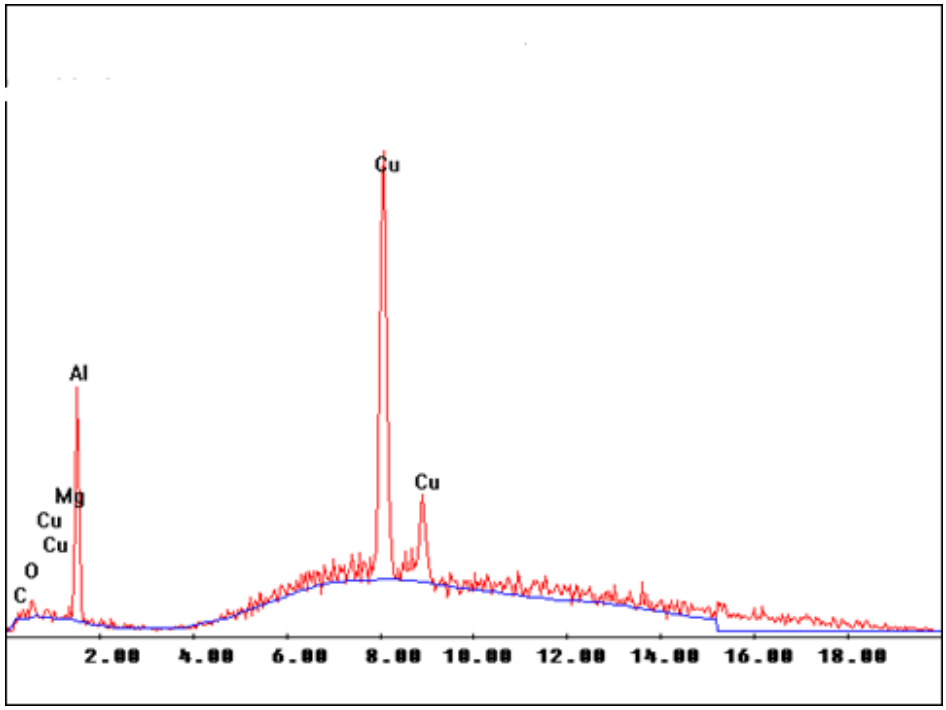

Figure A 8. EDS intensities inside the pit (zone A) of MMC XT2048 after immersion in 3.5% NaCl solution for 10h.

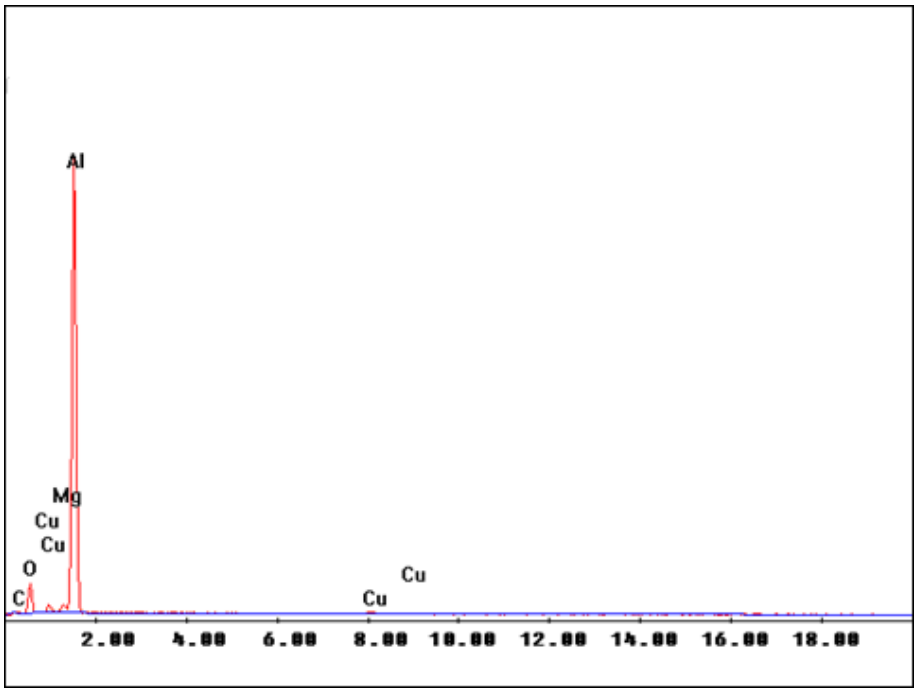

Figure A 9. EDS intensities around the pit (zone B) of MMC XT2048 after immersion in 3.5% NaCl solution for 10h.

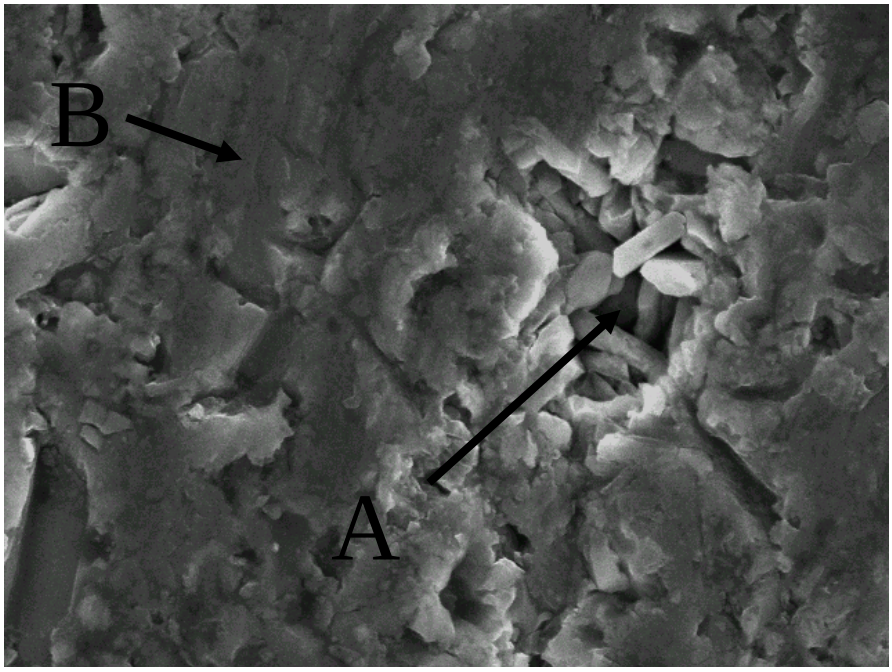

Figure A 10. EDS analysis point of MMC XT 2031 after immersion in 3.5% NaCl solution for 10 h, 2700x.

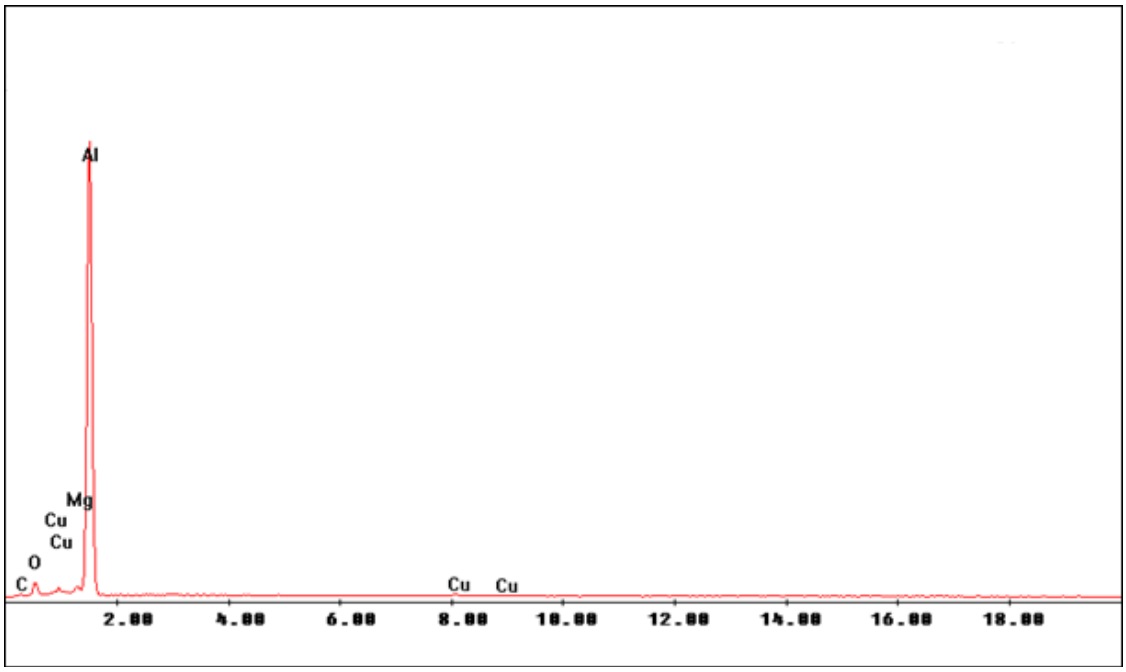

Figure A 11. EDS intensities inside the pit (zone A) of MMC XT2031 after immersion in 3.5% NaCl solution for 10h.

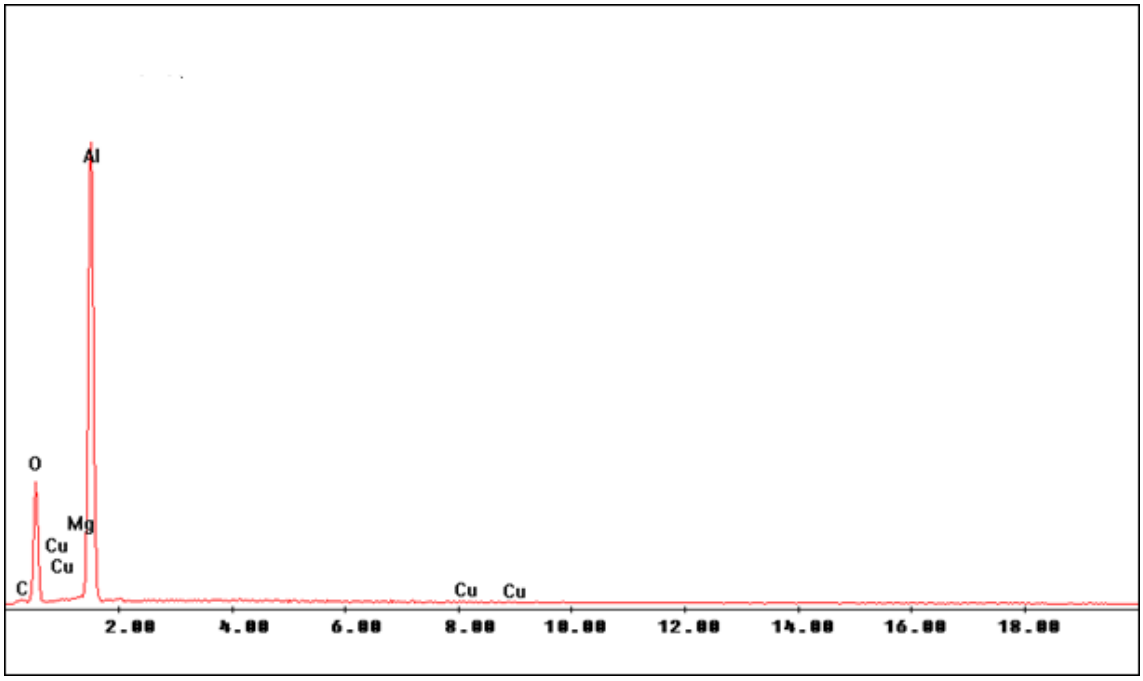

Figure A 12. EDS intensities around the pit (zone B) of MMC XT2031 after immersion in 3.5% NaCl solution for 10h.

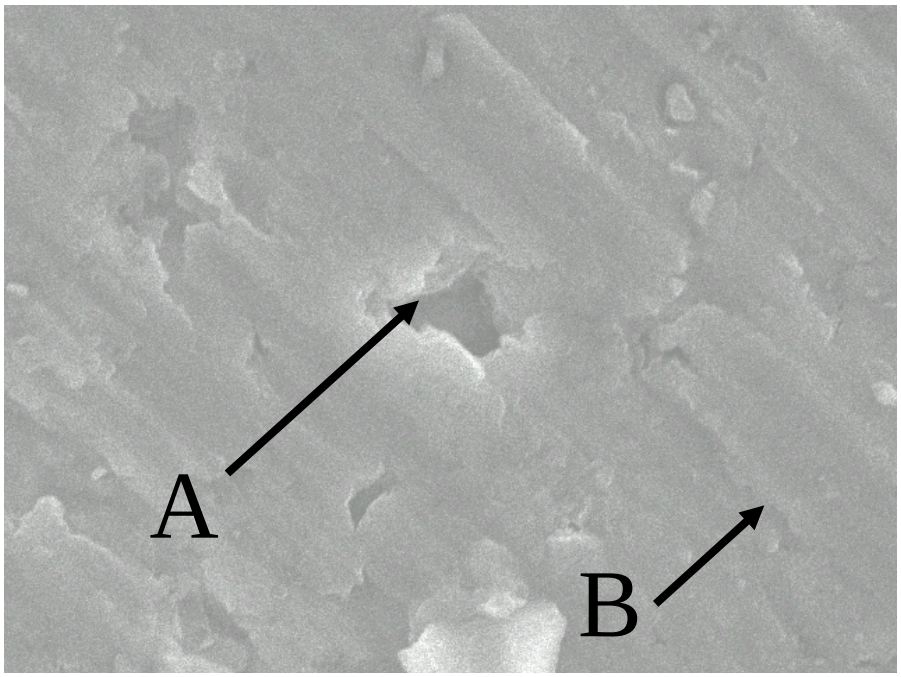

Figure A 13. EDS analysis point of MMC XT 1100 after immersion in 3.5% NaCl solution for 10 h, 3000x.

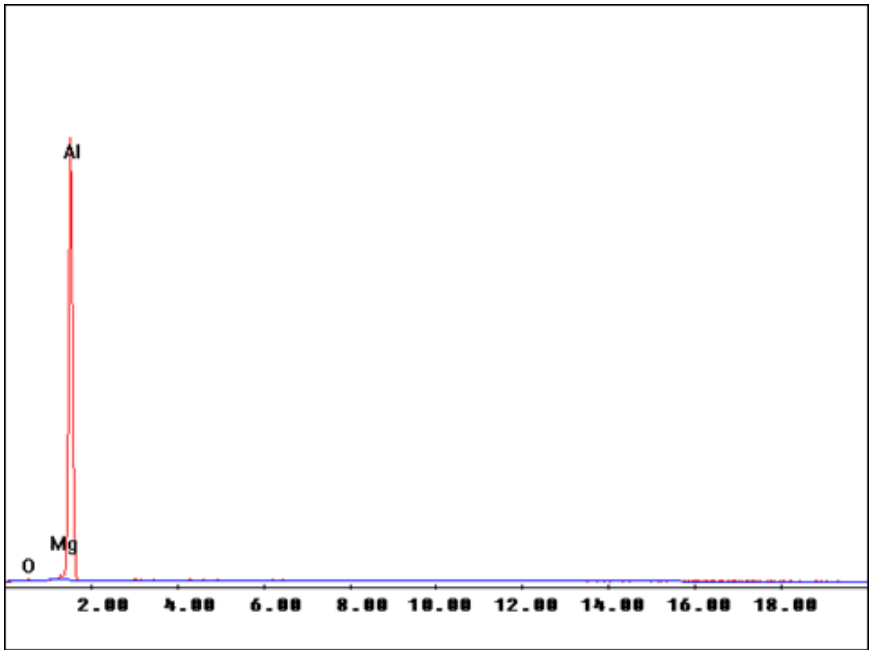

Figure A 14. EDS intensities inside the pit (zone A) of MMC XT1100, after immersion in 3.5% NaCl solution for 10h.

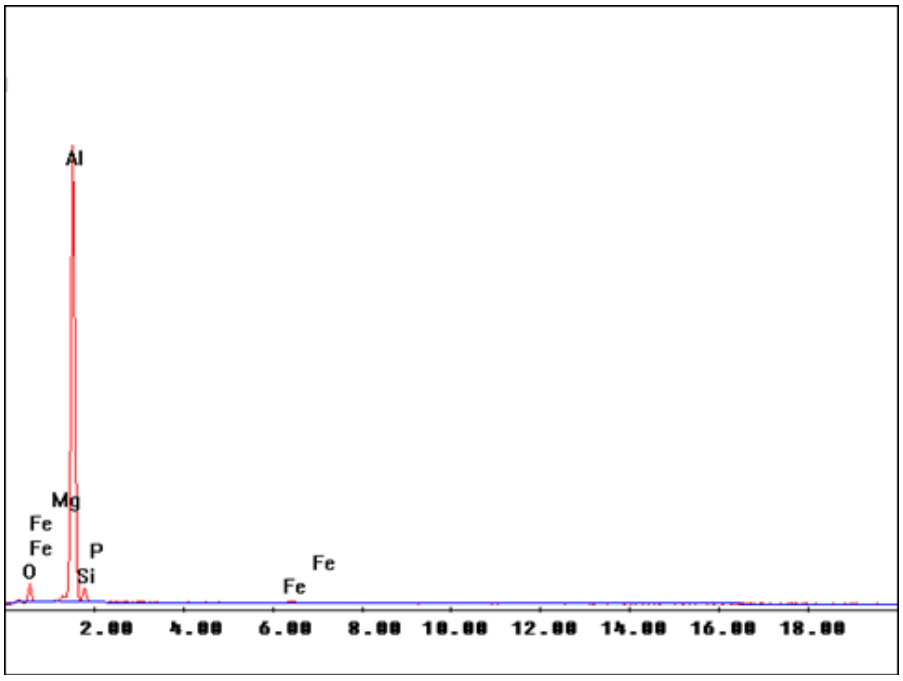

Figure A 15. EDS intensities around the pit (zone B) of MMC XT1100 after immersion in 3.5% NaCl solution for 10h.

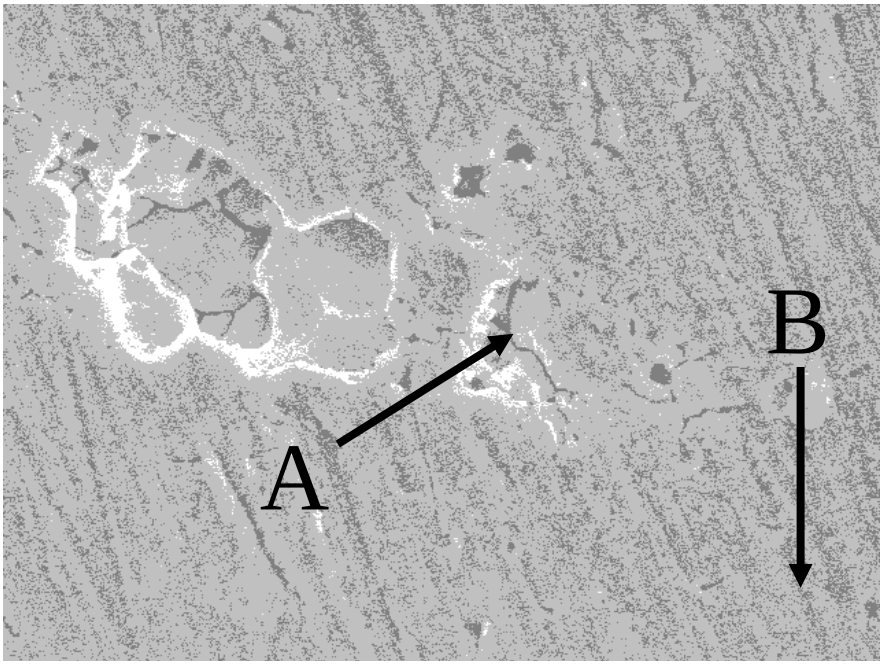

Figure A 16. EDS analysis point of MMC XT 2024 after immersion in 3.5% NaCl solution for 10 h, 3000x.

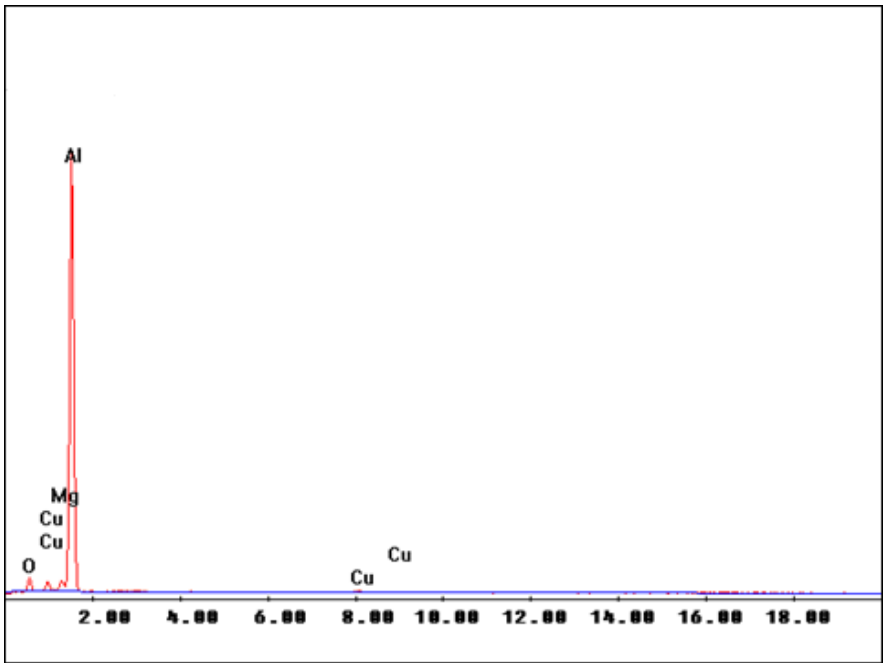

Figure A 17. EDS intensities inside the pit (zone A) of MMC XT2024 after immersion in 3.5% NaCl solution for 10h.

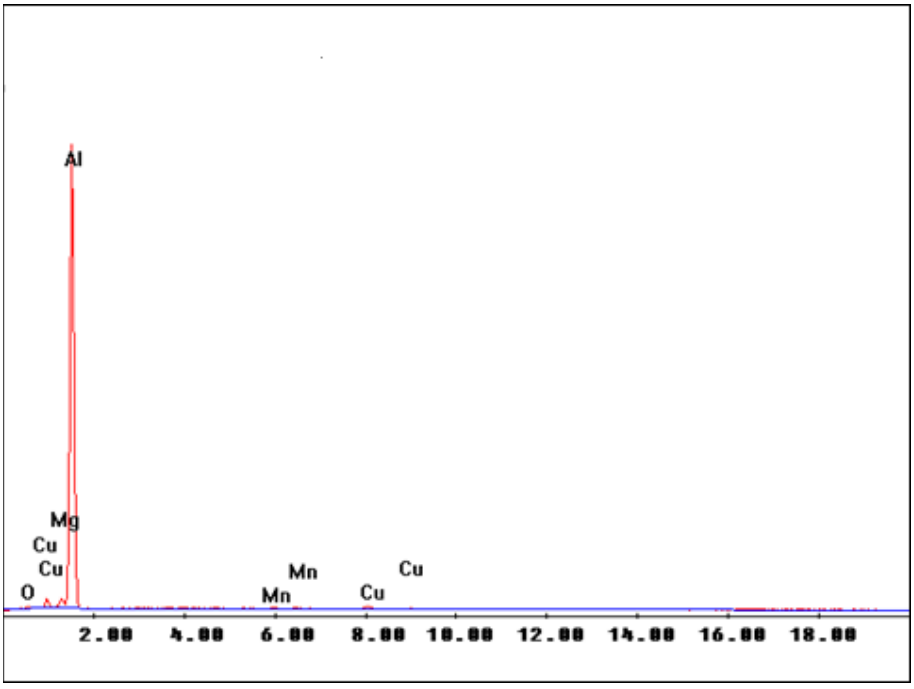

Figure A 18. EDS intensities around the pit (zone B) of MMC XT1100 after immersion in 3.5% NaCl solution for 10h.

APPENDIX B: EIS PLOTS

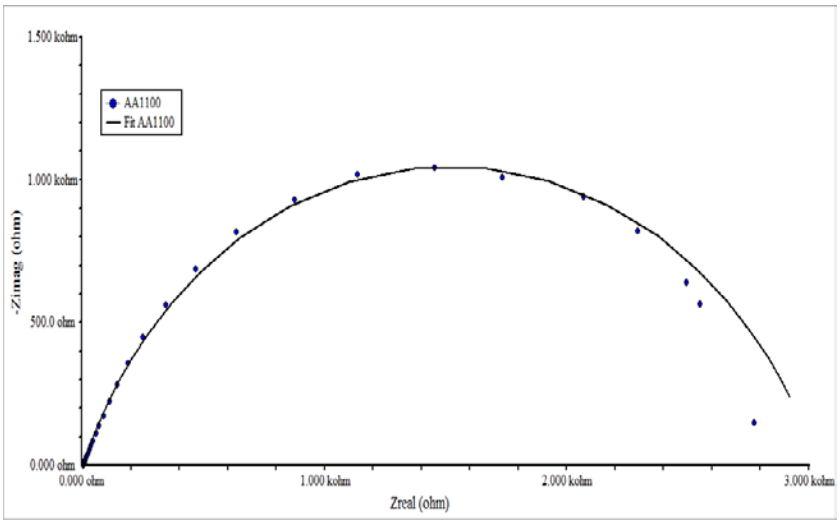

Figure B 19. Nyquist plot for the aluminum alloy AA1100 immersed in 3.5% NaCl solution.

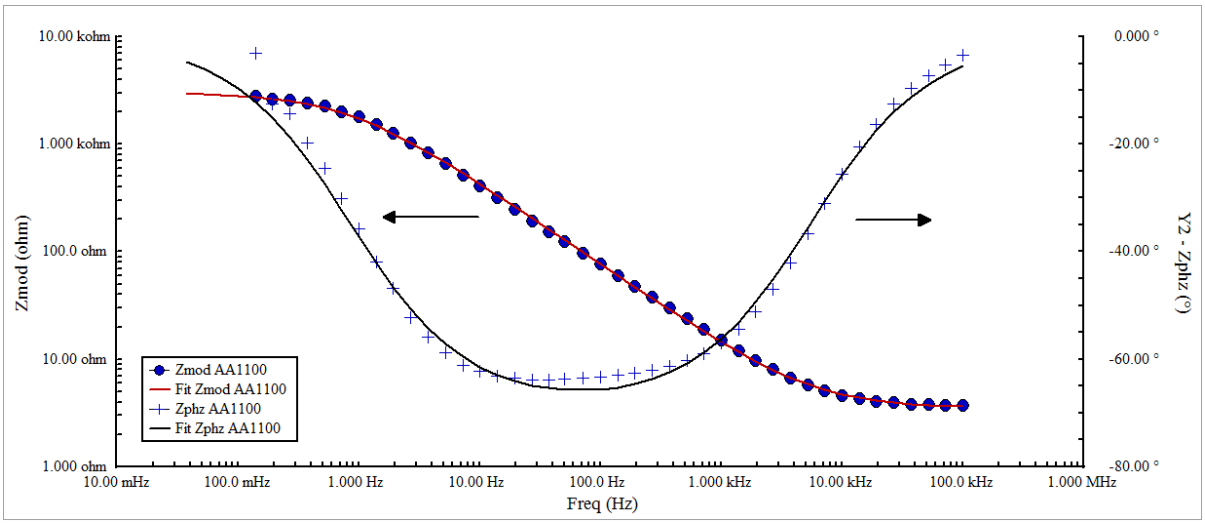

Figure B 20. Bode impedance magnitude and phase angle plots for the alloy AA1100 immersed in 3.5% NaCl solution.

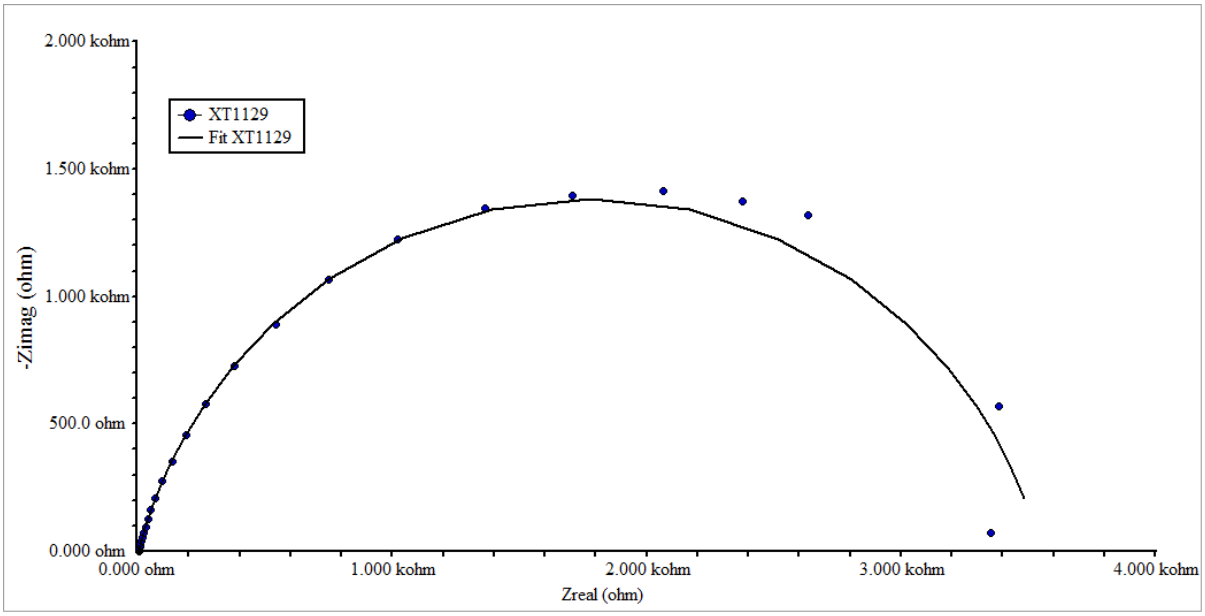

Figure B 21. Nyquist plot for the aluminum MMCs XT1129 immersed in 3.5% NaCl solution.

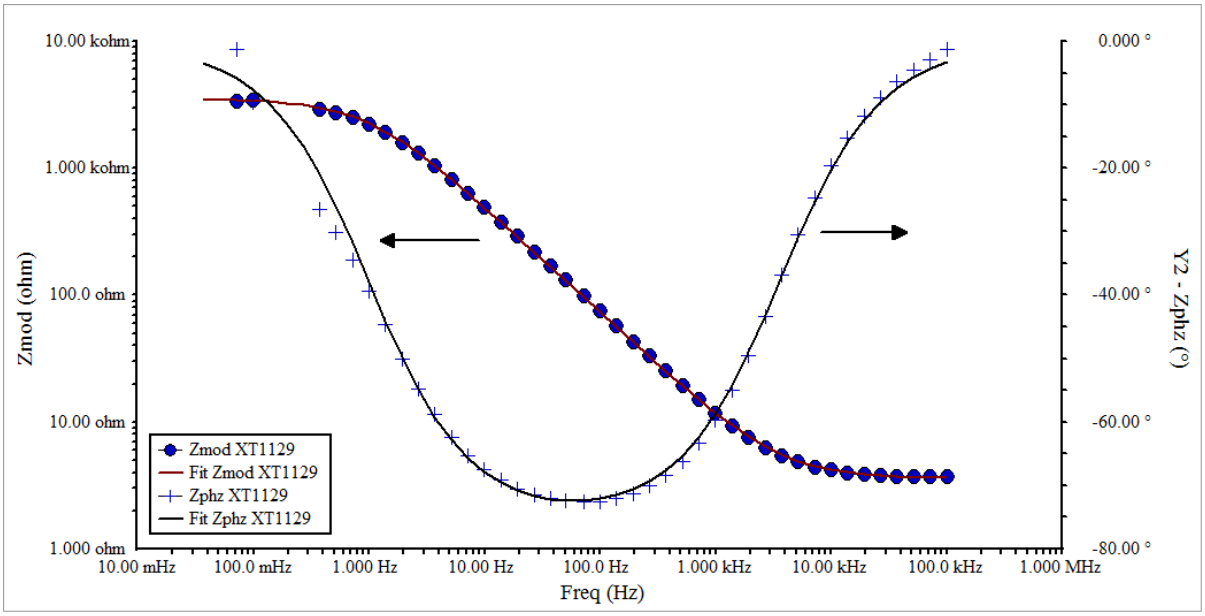

Figure B 22. Bode impedance magnitude and phase angle plots for the XT1129 immersed in 3.5% NaCl solution.

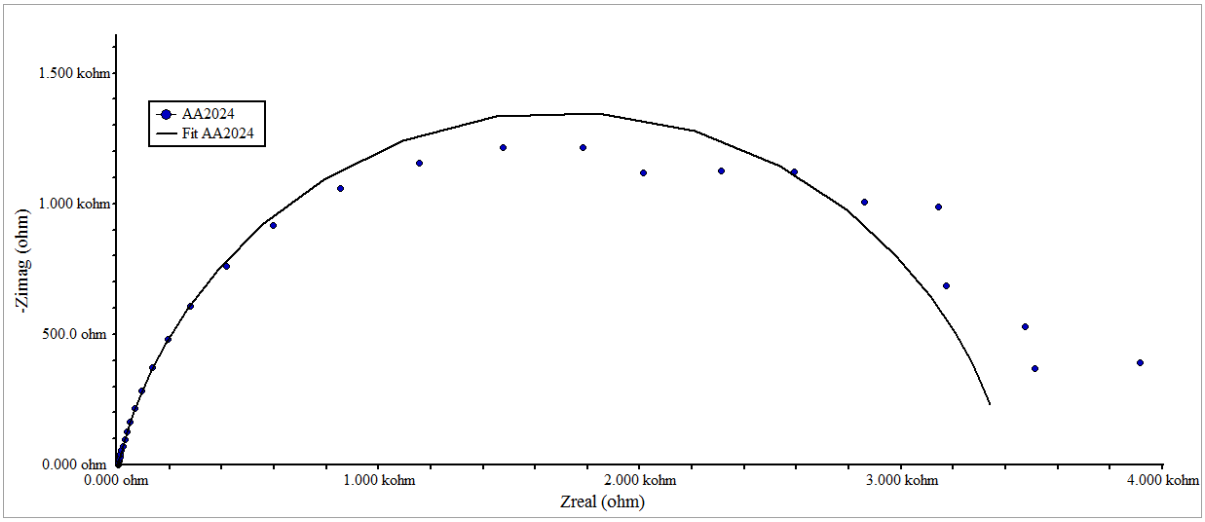

Figure B 23. Nyquist plot for the aluminum alloy AA2024 immersed in 3.5% NaCl solution.

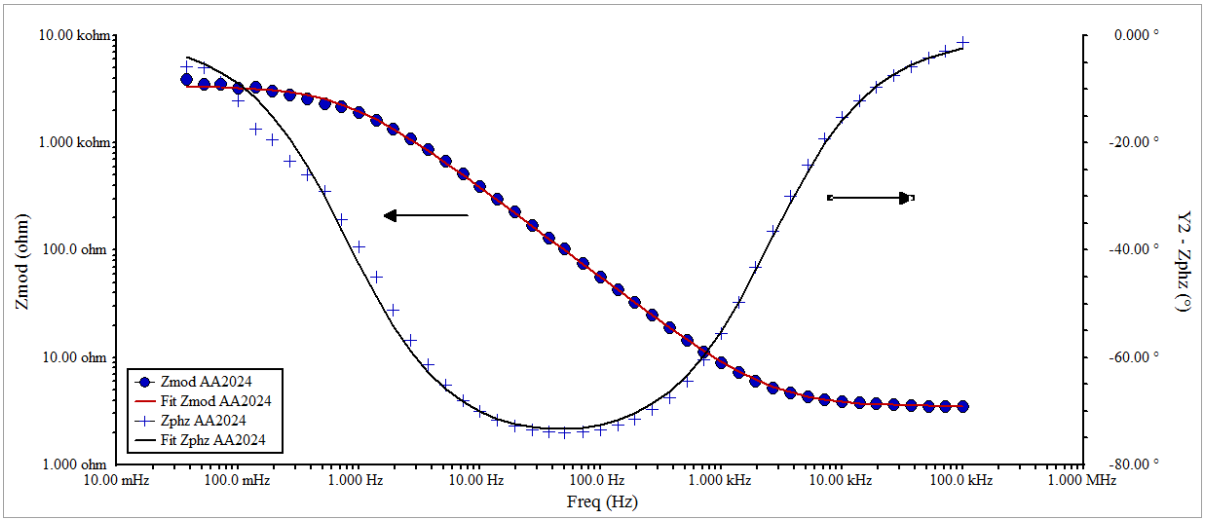

Figure B 24. Bode impedance magnitude and phase angle plots for the AA2024 immersed in 3.5% NaCl solution.

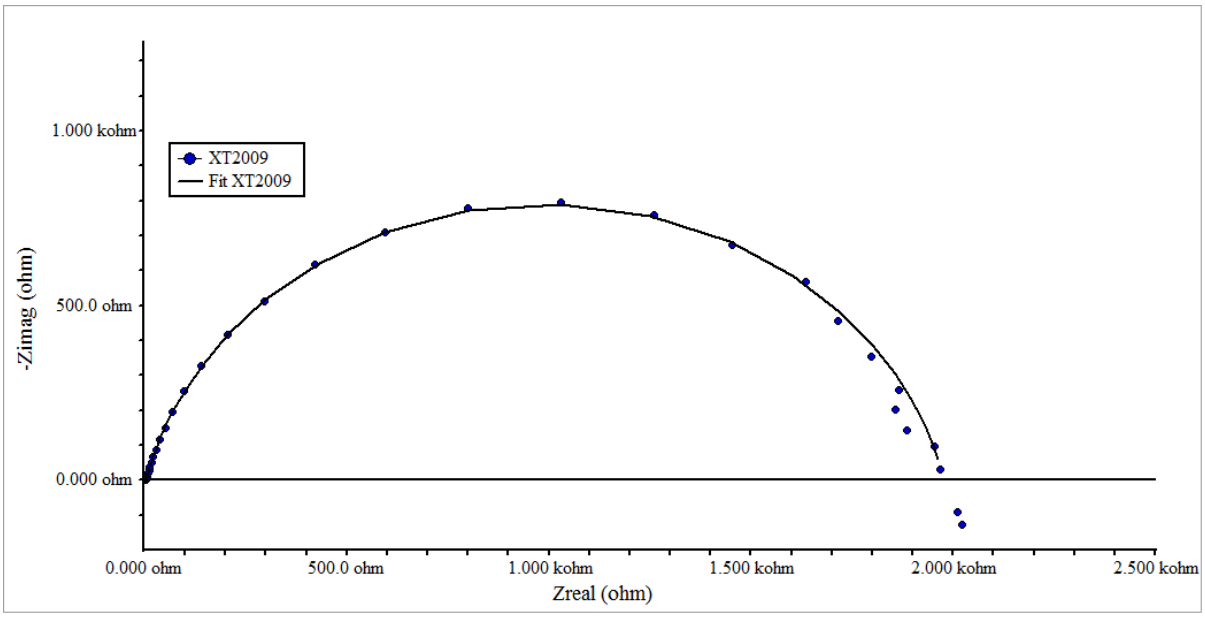

Figure B 25. Nyquist plot for the aluminum MMCs XT2009 immersed in 3.5% NaCl solution.

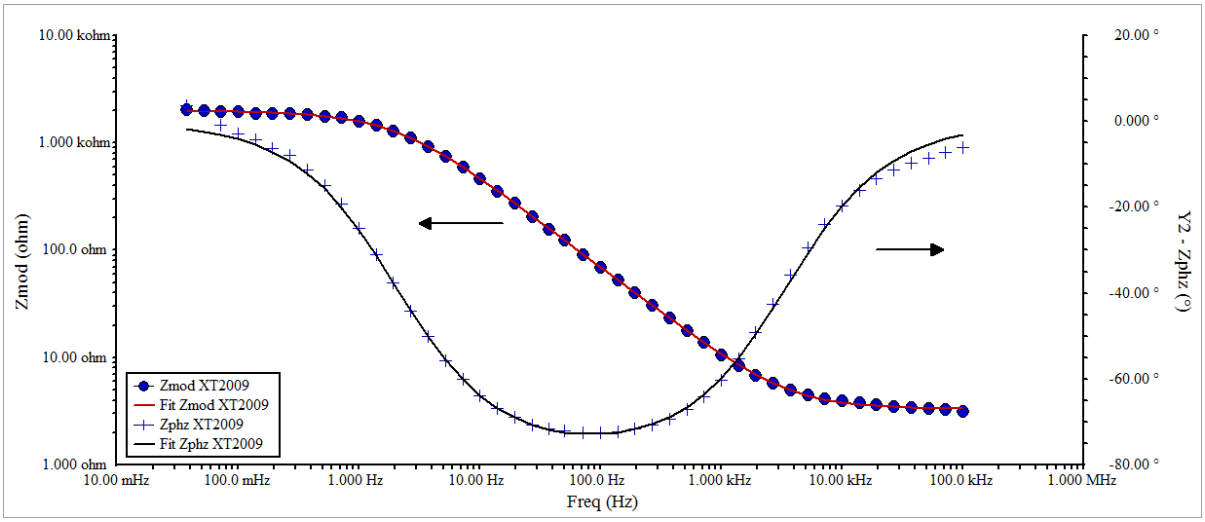

Figure B 26. Bode impedance magnitude and phase angle plots for the XT2009 immersed in 3.5% NaCl solution.

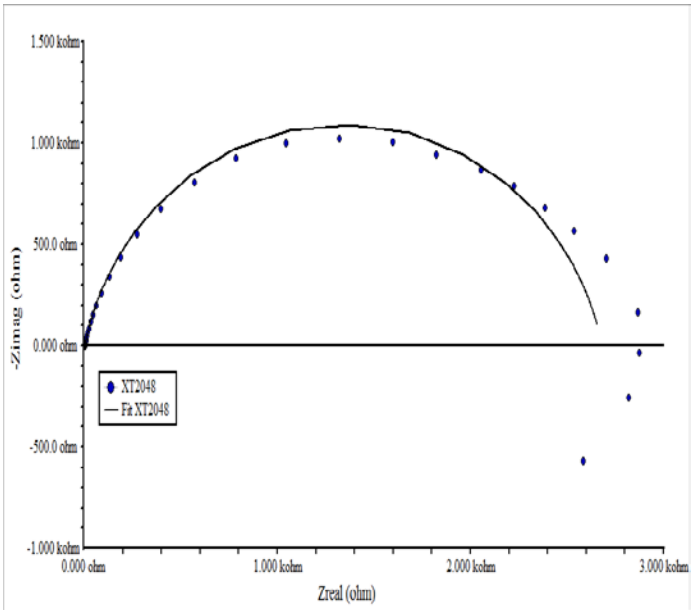

Figure B 27. Nyquist plot for the aluminum MMCs XT2048 immersed in 3.5% NaCl solution.

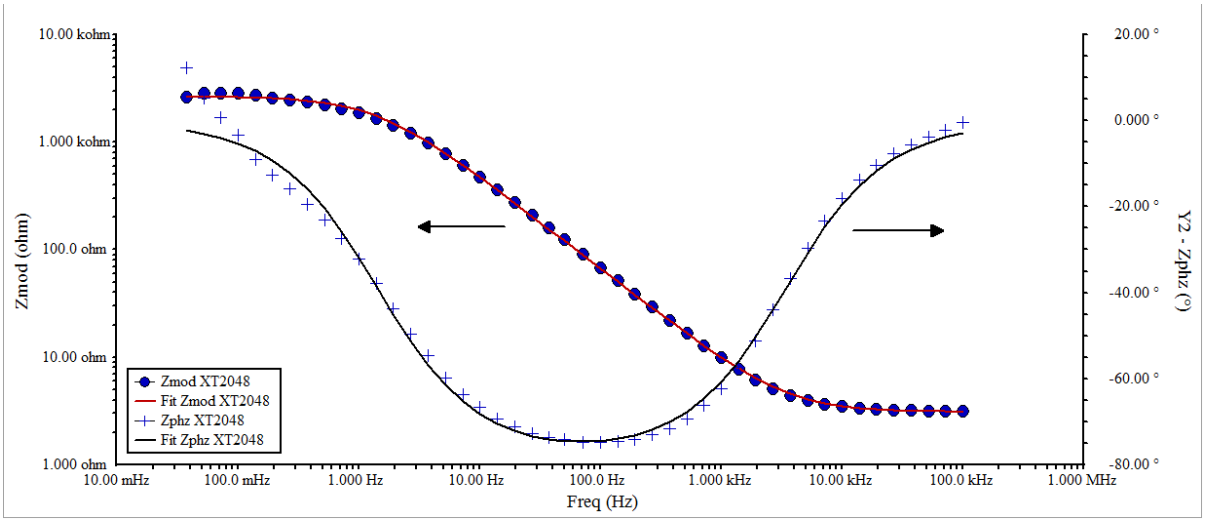

Figure B 28. Bode impedance magnitude and phase angle plots for the XT2048 immersed in 3.5% NaCl solution.

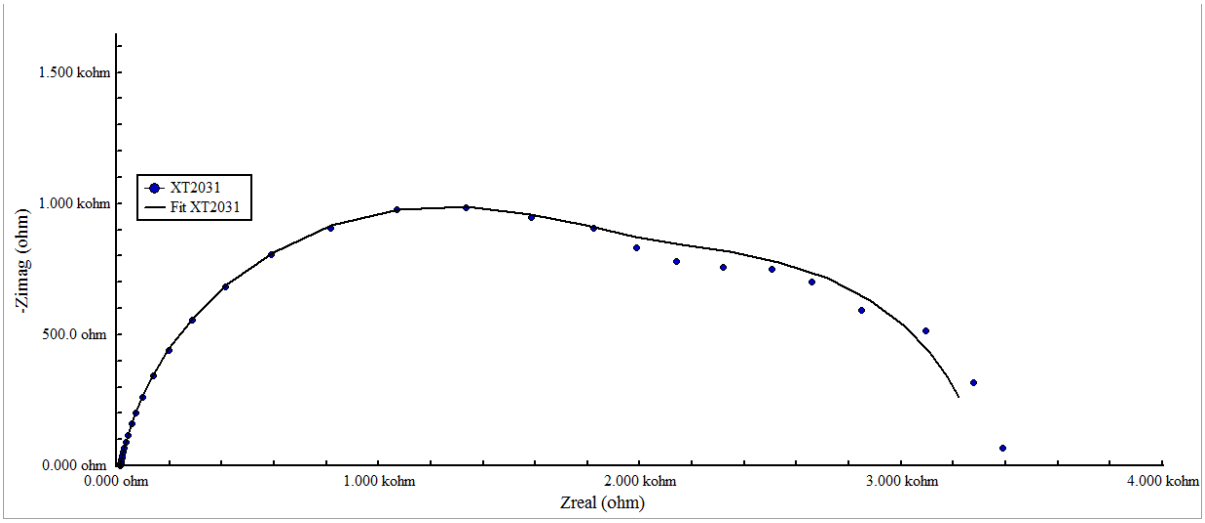

Figure B 29. Nyquist plot for the aluminum MMCs XT2031 immersed in 3.5% NaCl solution.

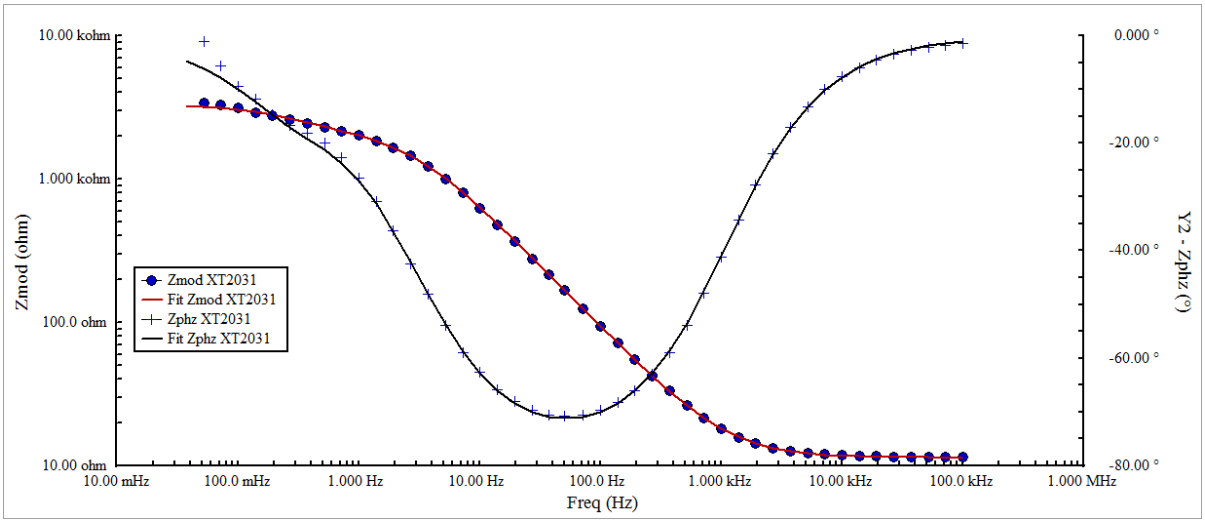

Figure B 30. Bode impedance magnitude and phase angle plots for the XT2031 immersed in 3.5% NaCl solution.

APPENDIX C : ANALYSIS OF EIS AND CP PLOTS

Table C-1. Average values of characteristic corrosion parameters of composites and monolithic alloys after cyclic polarization testing in aerated 3.5% NaCl solution.

Material	AA1100	σ^2	XT1129	σ^2	AA2024	σ^2	XT2009	σ^2	XT2048	σ^2	XT2031	σ2
Ep	-719.2	2.14	-648.7	1.83	-612.6	2.99	-651.5	4.19	-652.5	3.15	-649.0	0.00
Erp	-763.3	0.81	-822.0	6.58	-785.8	9.86	-775.5	9.20	-768.9	13.23	-787.0	2.65
Eoc	-748.0	0.90	-711.1	0.90	-655.2	4.60	-711.3	0.64	-707.7	0.65	-706.7	0.85
Ecorr	-733.7	2.08	-670.0	1.00	-630.0	2.65	-675.3	2.52	-676.0	6.08	-678.7	3.51
Icorr (μA)	14.07	2.00	6.05	0.91	10.05	3.35	14.67	3.15	6.02	1.02	3.54	0.94
Beta A (V/decade)	0.015	0.001	0.017	0.00049	0.017	0.003	0.026	0.002	0.019	0.003	0.022	0.004
Beta C (V/decade)	0.506	0.33	0.058	0.012	0.098	0.022	0.243	0.052	0.114	0.021	0.084	0.009
Corrosion Rate (mm/year)	0.153	0.022	0.066	0.010	0.114	0.038	0.162	0.035	0.064	0.011	0.036	0.010
Rp (Ω)	461.69	48.71	952.83	83.43	657.71	174.66	729.11	189.86	1218.46	311.43	2138.62	288.11

Table C-2. Average values of characteristic corrosion parameters of composites and monolithic alloys after EIS tests in aerated 3.5% NaCl solution.

Material	Rsoln (Ω)	σ^2	Rp (Ω)	σ^2	Cdl (S*s^n)	σ^2	m	σ^2	C (µF)	σ^2
AA1100	4.44	0.928	2145	768	8.16E-05	1.63E-05	0.821	0.045	56.08	11.74
XT1129	4.64	0.933	2876	588	6.14E-05	1.86E-06	0.846	0.007	44.79	0.41
AA2024	5.00	1.367	3937	466	6.46E-05	9.96E-06	0.846	0.012	53.30	10.03
XT2009	4.56	1.179	2438	425	5.09E-05	4.88E-06	0.858	0.007	35.97	3.10
XT2048	4.53	1.468	2804	258	4.72E-05	6.61E-06	0.860	0.010	34.62	5.83
XT2031	4.62	1.904	2486	134	4.07E-05	3.32E-06	0.869	0.022	28.98	1.62

Table C-3. Average values of characteristic corrosion parameters of composites and monolithic alloys after EIS tests in aerated 3.5% NaCl solution (continued).

Material	R_{cor}	σ^2	C_{cor}	σ^2	n	σ^2	Goodness fit	σ^2
AA1100							5.49E-03	3.48E-03
XT1129							1.13E-03	6.38E-04
AA2024							2.56E-03	3.32E-04
XT2009							5.60E-04	4.40E-04
XT2048							2.98E-03	7.79E-04
XT2031	1001	366.96	8.35E-04	1.42E-04	0.897	0.11	1.28E-03	1.16E-03

Table C-4. Average values of pit parameters produced during cyclic polarization tests.

Materials	Average pit density (pits/mm^2)	σ^2	Average area fraction of pits	σ^2	Average size of pits (μm)	σ^2
AA1100	1293.86	21.93	7.10E-05	4.94E-06	30.00	5.00
XT1129	1118.42	21.93	7.99E-05	1.92E-06	12.33	2.52
AA2024	818.71	55.19	9.48E-05	1.06E-05	22.33	2.52
XT2009	1578.95	43.86	9.08E-05	1.31E-06	15.00	3.00
XT2048	1242.69	33.50	8.17E-05	4.99E-06	12.00	2.00
XT2031	1250.00	43.86	8.95E-05	1.76E-06	11.67	5.69
XT2048 *	966.18	167.35	2.25E-05	2.05E-06	73.33	15.28
XT2031 *	805.15	147.59	1.89E-05	1.08E-06	70.00	10.00

Table C-5. Average values of pit parameters produced during EIS tests.

Materials	Average pit density (pits/mm^2)	σ^2	Average area fraction of pits	σ^2	Average size of pits (μm)	σ^2
AA1100	1929.82	350.88	1.76E-05	1.4E-06	3.00	0.50
XT1129	1016.08	55.19	6E-05	5.25E-06	13.33	2.89
AA2024	1008.77	21.93	8.31E-05	4.97E-06	11.00	3.61
XT2009	1147.66	55.19	7.59E-05	4.95E-06	10.00	2.00
XT2048	1637.43	55.19	8.12E-05	2.17E-06	10.00	1.00
XT2031	1864.04	65.79	9.08E-05	3.97E-06	12.00	2.00